THE CHARACTERIZATION OF SINGLE DNA MOLECULES IN NANOFLUIDIC DEVICES

R. Michael Schotzinger

A dissertation submitted to the faculty at the University of North Carolina at Chapel Hill in partial fulfillment of the requirements for the degree of Doctor of Philosophy in the Department of Biomedical Engineering.

Chapel Hill
2019

Approved by:

J. Michael Ramsey

Frances S. Ligler

Corbin D. Jones

Michael A. Daniele

Paul A. Dayton

ABSTRACT

R. Michael Schotzinger: The Characterization of Single DNA Molecules in Nanofluidic Devices
(Under the direction of J. Michael Ramsey)

This dissertation investigates DNA extension and transport characteristics in nanochannel confinement. Experiments were performed with the goal of advancing DNA polymer physics theory in nanochannel confinement by determining the influence of nanochannel aspect ratio (width/depth) on extension. DNA extension lengths were measured in the extended de Gennes regime in devices with unique aspect ratio nanochannels. Contrary to past findings, the DNA extension length was found to scale in agreement with the theoretically predicted relationship ($R \sim D_{eff}^{-2/3}$) and simulation results, with exponent values ranging from -0.67 to -0.70. In addition, the data suggests that modest aspect ratios do not appreciably affect scaling, while the smallest critical dimension of a nanochannel can strongly impact extension.

Further research investigated DNA transport characteristics in nanofluidic optical mapping scenarios with the goal of quantifying and ultimately improving DNA transport efficiency or the number of fragments that transport without detrimental DNA-wall interactions. A method for quantitative analysis of DNA transport was developed to compare fluorescently-labeled DNA traces interrogated at three successive areas of a serpentine nanochannel. DNA fragments were identified with the use of cross-correlation, DNA sizing, size calibration, and lastly fragment assignment based on DNA transport time and size. The addition of Mg cofactors into experimental buffers inhibited DNA transport by increasing stick-slip motion and DNA-wall affinity, with Mg-DNA bridging hypothesized as the leading mechanism of decreased performance. Adding an oligonucleotide dynamic coating addition into the buffer decreased the number of DNA fragments with impacted transport and strongly improved transport efficiency. In addition, both transport efficiency and diffusivity of DNA fragments were observed to be size-dependent.

Lastly, the design, fabrication, and testing of a single cell capture device is described. The purpose of the device was to enable cell capture, lysis, and DNA compartmentalization from single cells

downstream for genetic analysis. The device demonstrated repeatable capture and lysis of individual cells, but was not able to successfully compartmentalize DNA for downstream analysis due to a number of failure modes during DNA extraction. The single cell capture work is included here to educate and inform future experiment in the area.

“A man that chops his own firewood is warmed twice” – Henry David Thoreau

ACKNOWLEDGEMENTS

I would like to thank numerous people for helping me throughout the years in this program. First, I would like to thank Mike Ramsey for allowing me to join his lab after my first advisor left for another position. I would like to thank Laurent Menard for teaching me how to think critically as a scientist and his robust mentorship over the years. I would like to thank Larry Zaino for his comradery and sage advice, those years I worked with him were truly my favorite years in lab. I would like to thank Olivia Sanchez-Felix and John Perry for their friendship and keeping me sane and grounded throughout this process. I would like to thank J.P. Alarie for sharing his time and experimental thoughts with me in lab. In addition, I would like to thank the Soper diaspora – Kristina Herrera, James Taylor, Nicole Smiddy, and Colleen O'Neil – for their friendship and continued support over the years. I would like to thank my father for always lending an ear to help me strategize the best way forward in my career and my mother for her unwavering confidence in me. I would like to thank my brother Tom(my) for being exactly who I needed him to be throughout this process, my best friend. Most importantly, I would like to thank my fiancé Sheila Sodagar for all of the support she has given me. I dedicate my dissertation to her as a small token of my gratitude; upwards and onwards!

TABLE OF CONTENTS

LIST OF TABLES

LIST OF FIGURES

LIST OF ABBREVIATIONS AND SYMBOLS

AFM	Atomic force microscopy
N_A	Avogadro's number
D_t	Axial diffusion coefficient
BME	Beta mercaptoethanol
k_B	Boltzmann's constant
BSA	Bovine Serum Albumin
Cr	Chromium
c_i	Concentration of ionic species
L_c	Contour Length
CC	Correctly-called fragments
τ	Cross-correlation lag time
A	Cross-sectional area
I	Current
COP	Cyclo olefin polymer
λ_D	Debye length
K	Debye-Hückel parameter
ρ_0	Density of water
δ	Depletion length
DTT	Dithiothreitol
R	DNA extension
α	DNA hydrodynamic radius
η	Dynamic viscosity
D_{eff}	Effective Channel Diameter

v	Effective DNA line charge
w	Effective width
ρ_e	Electric charge density
EDL	Electric double layer
E	Electric field
φ	Electric potential
e	Electron elementary charge
EOF	Electroosmotic flow
μ_{ep}	Electrophoretic mobility
ψ	Electrostatic potential
σ^2	End-to-end length variance
u	Flow velocity
FIB	Focused ion beam
t_a	Fragment appearance time
K_bT	Free energy
g	Global persistence length
P	Hydrodynamic pressure
IC	Incorrectly-called fragments
J_i	Ion flux
v_i	Ion mobility
D_i	Ionic species diffusivity
I_s	Ionic strength
L	Length of flow
L	Length of nanochannel segment
Mg	Magnesium
Mg^{2+}	Magnesium ions

M	Missing fragments
Q	Net charge of a molecule
P	Persistence length
PBS	Phosphate buffered saline
PVP	Polyvinyl pyrrolidone
ROIs	Regions of interest
R	Resistance
Re	Reynolds number
D_R	Rouse Diffusivity
SEM	Scanning electron microscopy
μ	Solution dynamic viscosity
ε	Solution relative permittivity
σ	Standard deviation
T	Temperature
ε_0	Vacuum permittivity
z_i	Valence of ionic species
V	Voltage
ζ	Zeta potential

CHAPTER 1: INTRODUCTION

1.1 – Whole genome analysis promises future improvements in clinical outcomes

There is a growing understanding of the role that genomic structural variation has in a variety of diseases such as cancer, Parkinson's disease, autism spectrum disorders, and schizophrenia.[1-4] Methods and techniques capable of identifying and classifying structural variants (SVs) in DNA are therefore essential to researchers and clinicians, especially if they can provide wide coverage of the genome and are effective in regions of highly repetitive sequence.[5,6] Such techniques would supplement the more widely available genetic tests that identify high effect single nucleotide variants (SNVs) such as those in the BRCA1 and BRCA2 tumor suppressor genes that lead to elevated risk for breast and ovarian cancers.[7] Through a combination of whole genome analyses – including whole genome sequencing, structural variant calling, and epigenomic analysis – a better understanding of the combined effect of multigenic and regulatory region variation is anticipated.

Structural variants are genomic variations larger than SNVs and small indels. They include novel insertions, deletions, duplications, inversions, and translocations from 1 kbp to 3 Mbp in size, illustrated by Figure 1.2. The current methods primarily used for identifying SVs include the use of hybridization arrays and the analysis of high-throughput, short-read sequencing data, which can be supplemented by the use of mate pair, paired-end, or linked read library preparations.[8,9] These methods have the advantage of high throughput but also have significant limitations. For example, array based methods can only detect copy number variants (CNVs, duplications and deletions), typically above tens of kilobases. Sequencing based analyses generally have a similar size resolution limit. Furthermore, calling SVs in regions of segmental duplication, where they are known to be enriched, is often avoided because of the incidence of false positive calls by the analysis algorithms.[10] Optical mapping provides an alternative approach for assessing structural variation that relies on locating the position of restriction sites along extended DNA molecules to characterize long-range genomic information.[11,12] Optical mapping

techniques are able to analyze long DNA molecules, opening up the potential to identify SVs not currently accessible by other methods.

1.2 – The emergence of nanofluidic platforms as tools for genomic mapping

Early restriction mapping of genetic material was demonstrated by fixing stained DNA molecules on microscope slides or agarose gels where they were digested by endonucleases.[13-15] Fixing DNA to a surface prevents molecular fluctuations but can also result in inhomogeneous stretching or molecule breakage. In addition, multiple molecules are needed to determine statistically independent measurements of the restriction location.[16] In contrast with surface-fixed DNA mapping techniques, nanofluidic-based mapping applications rely on nanochannel confinement. Threading a biomolecule such as DNA through a nanochannel forces its extension and ensures the sequential passage of molecular segments through a nanoscale volume.[17-19] This has proven useful for the advancement of genomic mapping over the past two decades as a molecule stretched in a nanochannel is not subject to any other forces other than the lateral confinement responsible for its extension. Numerous approaches utilizing nanofluidic systems for optical DNA mapping have been developed.[12,20,21] Fluorescently stained DNA molecules can be labeled with a second fluorophore at restriction sites where single-strand cuts have been made by a nicking restriction enzyme (Fig. 1.3a). The DNA molecule is then extended in a nanochannel and imaged.[12] Partial denaturation mapping of long genomic molecules (Fig 1.3b.) is another demonstrated mapping technique made possible by utilizing formamide and local heating to elicit local sequence-specific denaturation.[20] In this method, intensity profiles of the DNA backbone are assembled to create sequence-specific barcodes of genetic information. DNA molecules can also be digested within a nanochannel by restriction enzymes that generate double-stranded cuts (Fig. 1.3c).[21] The ends of restriction fragments slightly withdraw due to molecular elasticity, causing observable gaps to appear between adjacent fragments. Confinement in the nanochannel prevents the intermixing of the restriction fragments.[21,22] The sizes of the restriction fragments are assessed from overlapped fluorescence images, and multiple single-molecule reads can be assembled into a genomic map by aligning to a reference. The alignment process utilizes NGS methods to create the reference genome by which optical mapping data is compared, illustrated by Figure 1.2. Optical mapping data can also be used *de novo* to create the reference map.[23,24]

1.3 – Optical DNA Mapping in the Ramsey Lab

Since the early 2010's, Professor Ramsey's lab has been working towards the development of a nanofluidic platform for optical mapping of DNA, resulting in numerous publications[25-29], patents[30-34], and the university spin-out Genturi Inc.[35] Restriction mapping of DNA enables genomic analysis of long strands of DNA (> 10 kbp) and is becoming an important tool for analyzing large-scale genetic mutations called structural variants. Optical restriction mapping of DNA in the Ramsey lab contains three main chronological components, schematically shown in Figure 1.1. To begin, a DNA molecule pre-bound with restriction enzymes is electrokinetically injected into a nanochannel where lateral confinement forces extension as it transports through the nanochannel. During transport the DNA molecule comes into contact with cationic cofactors which activate restriction enzymes to cut DNA into fragments at sequence-specific sites. Lastly, cut DNA fragments are transported through the nanochannel in an ordered fashion for back-end genomic analysis. The purpose of optical restriction mapping is to detect large scale mutations, which become apparent by comparing the length and order of DNA fragments to a reference genome. Early nanofluidic device fabrication work in the Ramsey lab in silicon, quartz, and plastics proved instrumental in creating finely-tuned required for DNA mapping.[26,27] Leveraging fabrication experience into the design and development of devices capable of DNA transport and enzymatic digestion within the confinement of nanochannels was instrumental to early successes. Novel nanofluidic device features were developed and provided real advantages over contemporary methods. Illustrated in Fig 1.1a. & b., networking nanoslit-nanochannels and 3D nanofunnels made reliable DNA nanochannel injection commonplace.[25,26] Fundamental research into DNA molecule dynamics and electrokinetic transport at the nanoscale set the stage for larger-scale DNA mapping experiments with HindIII restriction enzymes. Current Genturi mapping devices leverage nanochannel confinement to enable high-throughput DNA mapping in real-time.

1.4 – Current Challenges and Obstacles

A number of companies are attempting to commercialize mapping technologies including BioNano Genomics, Oxford Nanopore, and Nabsys. Advances in BNG's Irys platform have reduced the time and cost of mapping a human genome to a few days and $8,000, respectively.[36] Significant challenges exist for manipulating long genomic DNA molecules in nanofluidic platforms. Overcoming the

entropic barrier to DNA entry into a nanochannel is often nontrivial, particularly as nanochannel diameters decrease.[37] The nanochannels designed to extend double-stranded DNA are typically on the order of 50-200 nm in diameter and are difficult to fabricate.[17,38,39] Furthermore, confined DNA is subject to Brownian motion which may reduce the resolution of nanochannel based genomic mapping.[12,20,21] Some of these operational challenges can be mitigated by integrating additional nanofluidic elements into the existing basic geometries, thus providing greater control over DNA manipulation and characterization.[20] In addition and perhaps most importantly to this work, DNA transport in nanochannels can be Hindered by nonspecific DNA-wall interactions due to the complexity of buffer components and charged walls in an electrophoretic system.[40-45] Impacted DNA transport is highly detrimental to the throughput and accuracy of optical mapping platforms. Optimization of nanofluidic optical mapping platforms will be facilitated by a greater understanding of DNA behavior in nanochannels.

1.5 – Electrokinetic flow in nanochannels

The transport of fluids at the nanoscale diverges from micro or macroscale behavior. Differing physical processes cause unique fluidic phenomena at different length scales, hence dimensionless numbers are often used to model flow. To model flow at the nanoscale a few key assumptions are often made: the fluid is assumed to be a continuum, the viscosity of the fluid is assumed to be independent of shear rate, and the fluid is incompressible. With these assumptions the motion of a fluid due to electrokinetic flow at the nanoscale is thereby governed by the incompressible Navier-Stokes equation:

$$\rho_0 \left(\frac{\partial \boldsymbol{u}}{\partial t} + \boldsymbol{u} \cdot \nabla \boldsymbol{u} \right) = -\nabla p + \mu \nabla^2 \boldsymbol{u} - \rho_e \nabla \varphi \quad (1)$$

where μ is the dynamic viscosity, ρ_e is the electric charge density, φ is the electric potential driving flow, ρ_0 is the density of water, p is the pressure, and $\boldsymbol{u}$ is the resulting flow velocity. Terms corresponding to the fluid inertia are on the left side of the equation while terms corresponding to viscosity are on the right. The density does not change in incompressible fluids; therefore, the continuity equation can also be applied:

$$\nabla \cdot \boldsymbol{u} = 0 \quad (2)$$

In addition, the Reynolds number is a dimensionless quantity of inertial forces to viscous forces within a fluid, described by the following equation where L represents the length of the flow:

$$Re=\frac{\rho uL}{\mu} \tag{3}$$

The Reynolds number in nanofluidic flows is nearly always << 1. In other words, viscous components dominate the inertial components of flow. Due to this, flow in nanochannels is laminar and the left side of Eq. (1) is negligible. These typically encountered nanoscale flow conditions are referred to as Stokes flow.

Transport at the nanoscale through nanochannels is often driven electrokinetically with the use of a potential difference in an electrolytic solution. The electric potential of electrokinetic flows is directly related to the charge density through the electrostatic Poisson equation and the flux of ions for a species 'i' can be modeled by the Nernst-Planck equation:

$$J_i=-v_i z_i e c_i \nabla\varphi-D_i \nabla c_i+c_i \boldsymbol{u} \tag{4}$$

where v_i is the ion mobility, z_i is the valence of the ionic species, e is the elementary charge of an electron, c_i is the concentration of the ionic species, and D_i is the diffusivity of that species. Eq. (4) is the sum of three terms: Fick's first law specifying the diffusion of molecules in a chemical concentration gradient, flux due to φ, and convective transport due to external fields. The Nerst-Plank equation assumes ions to be ideal point sources with no radius and is valid in scenarios where ions do not influence each other.[46,47]

1.6 – Wall charge and Debye Length

Nanofluidic devices are often fabricated out of quartz, silicon, or polymers due to the relative ease of fabrication in those substrates. Nanofluidic channel walls of quartz, silicon, and polymer nanofluidic channels become deprotonated in the presence of basic solutions.[48,49] Deprotonation causes the walls to adopt an electrical charge, which can be described as a constant wall potential. This causes unique phenomena to emerge in nanofluidic systems due to the close proximity of wall charges to transporting ions in electrophoretic systems.

The Poisson-Boltzmann equation is used to describe the distribution of an electric potential from a charged surface to determine the effect of electrostatic interactions on surrounding ions and molecules:

$$-\nabla^2\psi = \frac{e}{\varepsilon}\sum_i c_i z_i \exp\left(\frac{-z_i e\psi}{kT}\right) \quad (5)$$

Here, ψ represents electrostatic potential, ε represents the relative permittivity of the solution, k is the Boltzmann's constant, and T is temperature. The electric potential experienced by a point charge from a charged surface increases with a decreasing distance according to Coulomb's law. The length of the electrostatic potential normal to the channel wall is referred to as the Debye length (λ_D), which, assuming low potentials ($ze\psi \ll kT$), is found by Taylor expanding the exponential in Equation 5 to arrive at the Debye-Hückel approximation:

$$\lambda_D = \sqrt{\frac{\varepsilon kT}{\sum_i N_A c_i z_i^2 e^2}} \quad (6)$$

where N_A is Avogadro's number. Within the Debye length charges are electrically screened, shielded by free ions in solution. For a symmetrically charged (z_i:z_i) electrolyte at 25 °C, the value of the Debye length (nm) can be simplified as a factor of ionic strength (I_s):[50]

$$\lambda_D = \frac{2.15 \times 10^{-1}}{\sqrt{I_s}} \quad (7)$$

$$I_s = \frac{1}{2}\sum c_i z_i^2 \quad (8)$$

Ion exclusion can occur in cases of low ionic strength where the concentration of ions of counter charge to channel walls are orders of magnitude higher than ions of the same charge. This particular scenario is classified as electric double layer (EDL) overlap and can influence ion and molecule transport through the nanochannel through means of ionic concentration polarization or depletion.[51-53]

1.7 – Electroosmotic flow and Drag

The migration of counterions to the charge of channel wall causes bulk fluid flow called electroosmotic flow (EOF). The directional motion of this bulk fluid flow is plug-like due to origination at the channel walls. For solids with negative wall charge the flow is in the direction of the cathode. The

Navier-Stokes equation (Eq 1.) and the Poisson-Boltzmann equation (Eq 5.) can be linearized to approximate the electroosmotic flow velocity in systems with a uniform wall surface charge and no external pressure gradients to arrive at the Helmholtz-Smoluchowski approximation:

$$\boldsymbol{u} = -\frac{\varepsilon \zeta E}{\eta} \tag{9}$$

where ζ is the zeta potential (potential at the stern layer), E is the electric field, and η is the dynamic viscosity of the solution. The utility of electroosmotic flow has enabled the development of numerous separation techniques in capillary electrophoresis applications.[54-56] However, electroosmotic flow is often detrimental to nanofluidic applications that rely on electrokinetic DNA injection into nanochannels. The EOF can be suppressed by dynamic coatings like polyvinyl pyrrolidone (PVP) that effectively coat channel walls to inhibit flow.[57] Electro-osmotic flow complicates DNA-nanochannel injection and therefore dynamic coatings like PVP are used as an EOF suppressant in nanofluidic devices.[25,26,58,59]

A charged biomolecule like DNA experiences electrical charge screening in an electrolytic solution. These screening counterions (EDL) around the DNA molecule are mobile and move in the opposite direction to the molecule. The movement of screening counterion movement causes fluid motion around the DNA in a similar fashion to electro-osmosis. This fluid motion has consequences for the electrophoretic mobility of DNA dependent on the thickness of the EDL. The thickness of an EDL can be divided into two categories, thick and thin, depending on the summation of the Debye-Hückel parameter K (inverse of debye length, $K=\frac{1}{\lambda}$) and the molecule radius r. If $Kr >> 1$, the EDL is classified as thin and resembles electro-osmotic flow:

$$\mu_{ep} = \frac{\varepsilon_r \zeta}{\eta} \tag{10}$$

where μ_{ep} is the electrophoretic mobility of the molecule. Conversely if $Kr << 1$, the EDL is classified as thick and the force acting on the molecule is a combination of both drag and Coulomb forces:

$$\mu_{ep} = \frac{Q}{6\pi\eta r} \tag{11}$$

where Q is the net charge of the molecule. In Eq. (10) the electrophoretic mobility of a DNA strand is independent from molecule length and is important to the high ionic strength solutions used in mapping applications. The equation describes the relative mobility of a molecule and assumes the solute to be at

rest. In thin EDL electrokinetic forces and drag are balanced for any DNA length. DNA mobility, velocity, and nanochannel transport are therefore all independent from molecule size. This conclusion has been experimentally vetted in electrophoresis applications, one of which is shown by Figure 1.4.[60-63] Nanofluidic mapping platforms leverage this phenomenon for ordered transport of digested DNA fragments in the nanochannel, as all digested fragments move at the same velocity and ensure fragments do not pass each other.

1.8 – Non-specific adsorption onto channel walls

The nanofluidic flow and charge-based phenomena introduced above are all relevant to DNA mapping devices. As stated above, a detrimental issue faced by micro- and nanofluidic devices in general is the nonspecific adsorption of biomolecules onto device surfaces.[40-44] This is commonly referred to as biofouling and can arise from any undesired interaction with channel walls including protein, peptide, polymer, or DNA itself. Non-specific surface interactions can have catastrophic consequences for mapping applications, including: degrading the DNA sample, influencing DNA transport behavior, or causing complete blockage of the nanochannel. Moreover, DNA fragment rearrangement in the nanochannel may occur if a subset of molecules are slowed during transport. The aforementioned in micro- and nanofluidic devices represent major failure modes for mapping applications, especially when complex chemistry occurs during DNA confinement in nanochannels.

The hydrophobicity of polymeric channels and steric interactions with channel walls theoretically inhibits DNA adsorption. In practice, however, this is not always true. Non-specific surface interactions in complicated buffer solutions may cause reversible DNA adhering to channel walls, empirically manifested as stick-slip motion during electrokinetic transport.[45,64] An important distinction between DNA adsorption or adherence in nanochannels is covalent vs. non-covalent bonding. Covalent bonding in nanochannels is irreversible, while stick-slip motion continually affects DNA during transport and is non-covalent. Stick-slip motion is observed when attractive DNA-wall interactions are greater than electrokinetic driving forces, but may be intermittently witnessed during transport. Increasing the driving E-field has been shown to decrease stick-slip motion.[45] Electrostatic, van der Waals, Lewis acid-base hydration forces, and dielectrophoretic trapping have all been proposed to be the cause of adsorption of proteins or DNA. However, the difficulty in decoupling the aforementioned forces has made identification of a leading

mechanism problematic. To further complicate the matter, many restriction endonucleases used in mapping techniques require a cationic cofactor like Mg^{2+} and complex restriction digest chemistry in the nanochannels. While polyanionic DNA is repelled from the negative charge of polymeric walls; conversely, positively charged Mg^{2+} can absorb or bind to the channel walls and associate with DNA. One specific example of this phenomenon, Magnesium-DNA bridging, has been witnessed in capillary electrophoresis applications,[65,66] and may contribute to the detrimental surface-wall interactions witnessed in DNA transport functionalities. Mg^{2+} affects the physicochemical properties of DNA by altering the stability of the double helix. In addition, Mg^{2+} binding to DNA has also been shown to attenuate molecule fluctuation,[67] decrease phosphate electrostatic repulsion,[68] and cause a dehydration effect dependent of Mg-DNA binding structure,[69] further complicating molecular behavior. In summary, non-specific wall interactions in complex buffer solutions cause stick-slip motion and impacting DNA transport, impairing DNA mapping platform utility.

Nanochannel surface passivation has been proposed as a potential way to avoid non-specific surface interactions between DNA and nanochannel walls. Bovine serum albumin (BSA) is widely used for this purpose, but has limited applicability as it relies on stochastic binding to the channel walls and therefore a uniform coating is unlikely.[70] Lipid bilayers have also been proposed and implemented as nanofluidic passivation agents.[44,71] However, adoption of lipid bilayers has been stymied due to the complicated coating mechanism, lipid vesicles, required to coat the nanochannels.[44] Further development of nanochannel passivations would benefit from dynamic coatings that are consistently replenished for homogeneity purposes. Notwithstanding, non-specific surface interactions in nanochannels in general remain understudied to date.

1.9 – Physical properties of DNA

The physical properties of DNA play an important role in mapping applications. DNA is a flexible polyelectrolyte that assumes a negative charge in electrolytic systems due to molecule's phosphate backbone. The physical characteristics of DNA have been studied in detail over the past few decades. Fluorescent staining of DNA is possible with a variety of dyes. Intercalating dyes like YOYO-1 bind to double stranded DNA through bis-intercalation, or insertion of the dye molecule between the planar bases

of DNA. The intensity of intercalated YOYO-1 increases ~3000x upon binding, making it particularly useful for studying the polymeric physics of DNA.[72]

DNA is defined by the following physical parameters: the contour length *(L_c),* effective width (*w*), and persistence length *(P)*. The contour length is the end-to-end length of a fully-stretched DNA molecule. The contour length of unstained DNA was found to be approximately 0.34 nm per basepair.[73] The contour length is affected by staining of DNA; YOYO-1 intercalation of DNA increases the contour length by approximately 0.44 nm per dye molecule.[74] Therefore the full contour length (nm) of YOYO-1 stained DNA increases by the bp:dye molecule ratio:

$$L_c=0.34(bp)+0.44(c_{bp:dye}) \tag{12}$$

where *bp* signifies the number of basepairs in a DNA molecule and $c_{bp:dye}$ is the ratio of basepairs per dye molecule. The effective width (*w*) of DNA takes both the biopolymer's physical width and the distance of charge influences into account. Historically, effective width has been estimated as the summation of the physical width and twice the Debye length, however, this approximation underestimates its actual value.[17] *Stigter et al.* estimated the effective width as the excluded volume of two charged cylinders, arriving at the equation:

$$w=\lambda_D\left[0.7704+\log\left(\frac{v^2}{2\varepsilon\varepsilon_0 KT}\right)\right] \tag{13}$$

here *v* is the effective DNA line charge and ε_0 is the vacuum permittivity.[75] Eq. (13) depends strongly on the ionic strength of the solution and is commonly used to estimate DNA effective width in electrolytic systems.[58,74,76] Lastly, the persistence length is a measure of the rigidity of DNA, and can be thought of as the physical length from a conformation where the DNA chain correlations to the starting configuration approach zero. The flexibility of a DNA molecule is governed by its persistence length, which like the effective width also depends strongly on the solution ionic strength. Dobrynin empirically determined the persistence length (nm) of DNA according to the following equation:[77]

$$P\approx 46.1+6.3\lambda_D \tag{14}$$

The contour length, effective width, and persistence length of DNA all influence the behavior of DNA in nanochannel confinement.

1.10 – DNA in Confinement

Injection of DNA into a nanochannel smaller than its radius of gyration forces extension along the nanochannel according to Figure 1.5. The degree of DNA extension is governed by polymeric physics. DNA assumes different conformations based on the degree of confinement. Two main regimes describing the extension of strongly confined and weakly confined DNA respectively exist: the Odijk regime, and the de Gennes regime. Both regimes are displayed in Figure 1.5. The Odijk regime in nanochannels smaller than *P* describes DNA extension as deflecting rigid rods.[78] The de Gennes regime described extension in nanochannels larger than *P* as a string of non-interpenetrating spherical blobs.[79] Two transitional regimes, the hairpin[80] and extended de Gennes,[39,81] have been proposed as intermediate regimes to Odijk and de Gennes. Long-range optical mapping of genetic information utilizes DNA extension in all extension regimes. Numerous simulations have investigated DNA extension; however empirical data has not been able to replicate simulation extension scaling results in the transitional regimes to date. *Reisner et al's* review provides a thorough perspective into the fundamental physical and statistical mechanics of DNA extension in nanochannels.[17] Optimization of mapping devices will be facilitated by a greater understanding of molecular behavior in extension regimes.

1.11 – Research Objectives

The motivation behind this work is to better understand the physical and chemical phenomena affecting DNA during electrokinetic transport in mapping devices. The nature of this work has obvious translational utility to mapping applications, but the conclusions also further advances basic research in DNA nanochannel transport and polymer physics. Chapter 2 investigates the extension physics of DNA in the extended de Gennes regime and serves as the first empirical extension data in agreement with theory and simulations. In Chapter 3 the development of an analysis method for high-throughput characterization of DNA transport in mapping devices is described. Chapter 4 utilizes the method described in Chapter 3 to analyze the effect of Mg cations, nanochannel path length, and oligonucleotide dynamic coatings on DNA transport efficiency in the attempts to minimize the influence of DNA-wall interactions during transport. Chapter 5 departs from the optical mapping theme, where a novel single cell capture device and preliminary testing of cell trapping, lysis, and whole genome manipulation is explored. The final chapter discusses future directions. The work contained in this dissertation is

expected to advance optical mapping platforms by proving a deeper understanding of DNA characteristics and transport physics in mapping-type scenarios.

1.12 – Figures

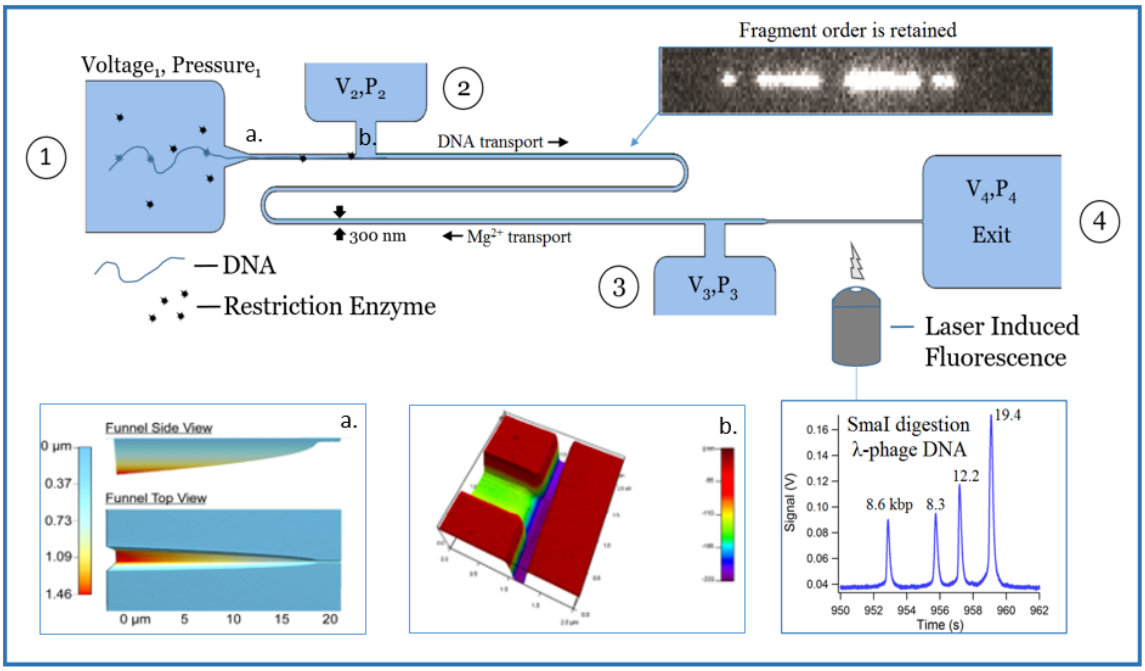

Figure 1.1: Schematic of a nanofluidic platform for the generation of ordered restriction site maps. Fluorescently stained DNA at ① is electrokinetically driven into the nanofluidic channel along with a cutting restriction endonuclease. The transport velocity of DNA through the serpentine nanochannel and provision of the enzyme cofactor (Mg^{2+}) is controlled by the voltage and pressure inputs at ①,②,③,④. This localization ensures that DNA digestions occurs solely within the nanochannel, where fragment order is maintained. Fragments are accelerated prior to fluorescence excitation at a focused laser spot. Baseline resolved peaks in the resulting emission signal are integrated to determine fragment sizes. (a.) is a AFM profile of the 3D injection funnel. (b.) shows one of the slits used for electrokinetic gating of DNA injection.

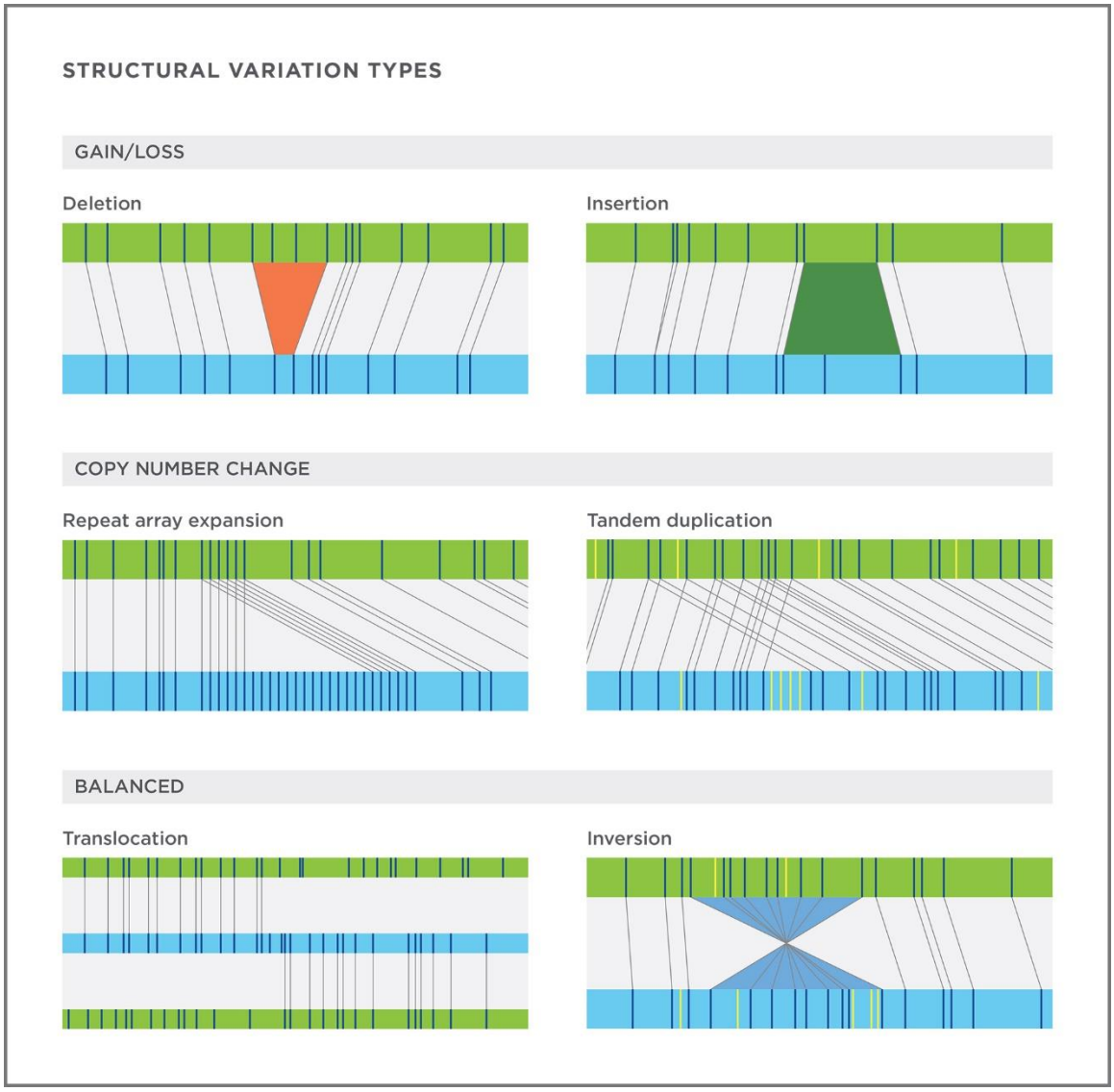

Figure 1.2: Examples of structural variant mutations. The green block represents a reference of a DNA molecule digested at sequence-specific sites. The blue block represents the mutated variant of the reference molecule. Structural variants range in size from 1 kbp to 3 Mbp. Illustration from Bionano Genomics.[82]

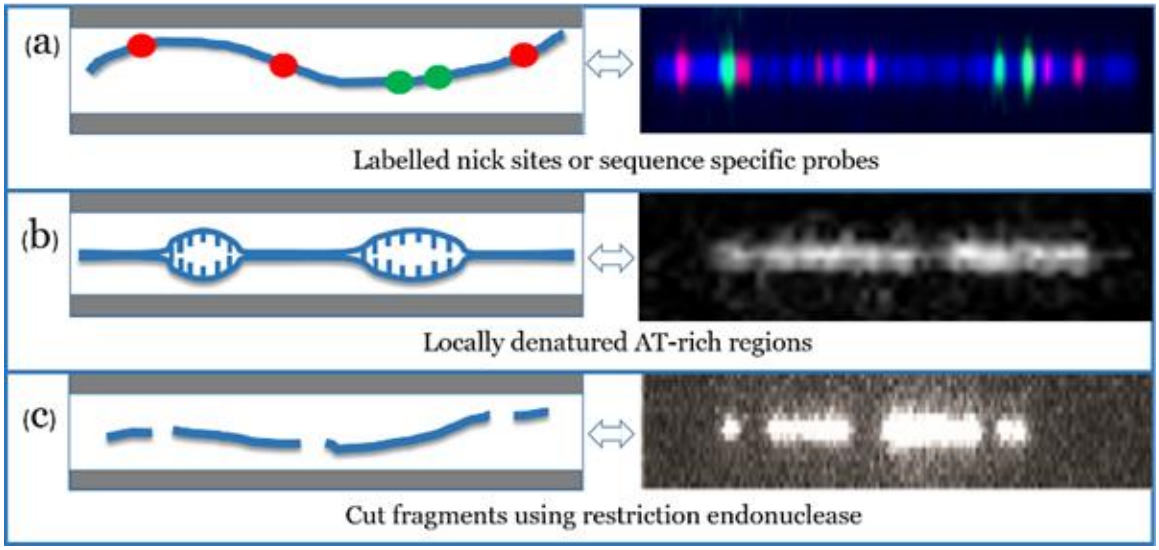

Figure 1.3: Methods of optical DNA genomic mapping. (a) DNA labelled with fluorescent molecules at two different restriction sites.[22] (b) DNA denatured at concentrated AT regions.[30] (c) Endonuclease-digested DNA fragments and unpublished YOYO-1 fluorescence data from Ramsey Lab. Right hand column consists of data from (a) published reference[22] (b) published reference[30] and (c) unpublished data from Ramsey group.

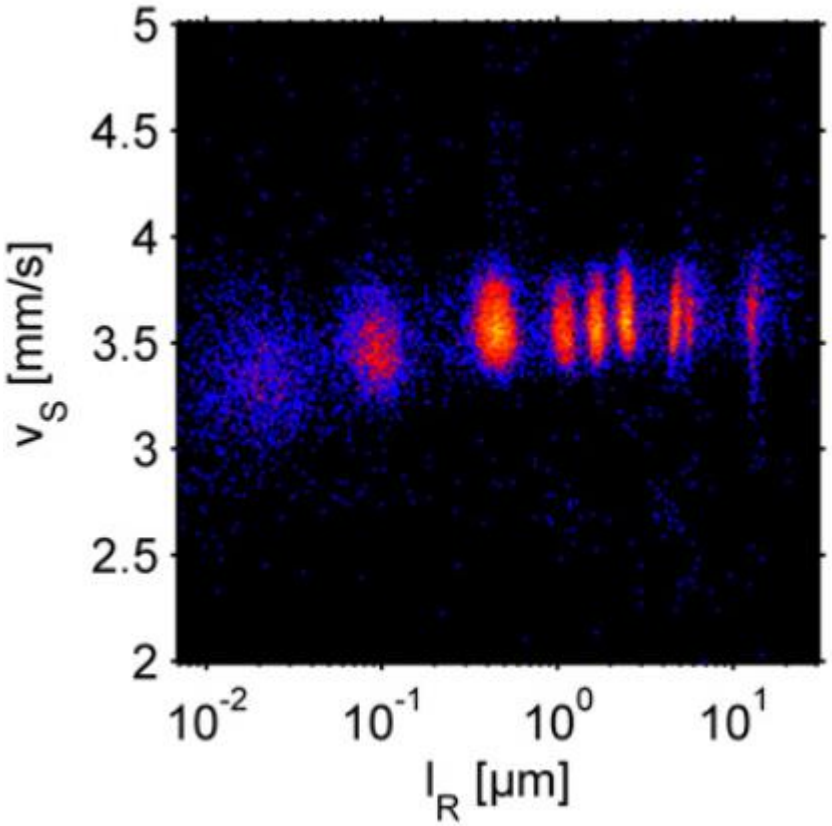

Figure 1.4: Modified figure of λ-HindIII digest and undigested λ DNA velocity measurements from *Reccius et al*. in nanoslits.[59] l_R is a measure of a DNA molecule length that includes extension length and length from looped DNA sections. DNA speed is essentially constant with length.

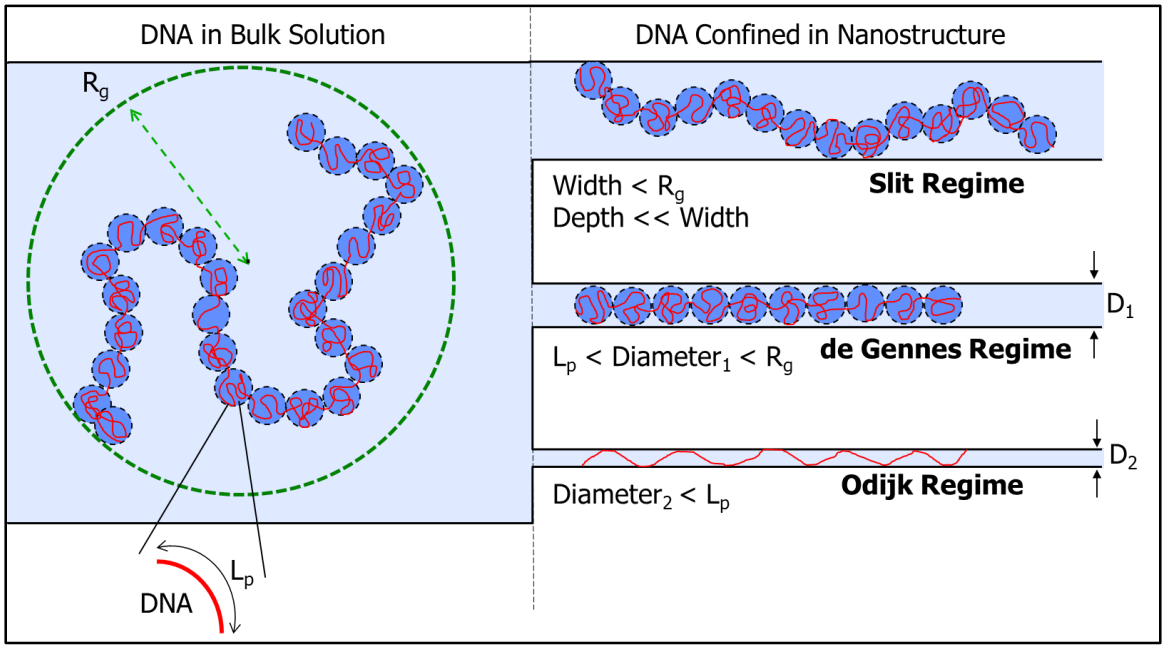

Figure 1.5: DNA extension in varied nanochannel confinement.

REFERENCES

1. Stratton, M. R., Campbell, P. J. & Futreal, P. A. The cancer genome. *Nature* **458**, 719-724 (2009).

2. Shulman, J. M. Structural variation and the expanding genomic architecture of Parkinson disease. *JAMA Neurol* **70**, 1355-1356 (2013).

3. Brandler, William M. *et al.* Frequency and Complexity of De Novo Structural Mutation in Autism. *Am. J. Hum. Genet.* **98**, 667-679 (2016).

4. Karayiorgou, M., Simon, T. J. & Gogos, J. A. 22q11.2 microdeletions: linking DNA structural variation to brain dysfunction and schizophrenia. *Nat Rev Neurosci* **11**, 402-416 (2010).

5. Nazarenko, M. S. *et al.* Genomic structural variations for cardiovascular and metabolic comorbidity. *Sci Rep* **7**, 41268 (2017).

6. Chiang, C. *et al.* The impact of structural variation on human gene expression. *Nat Genet* **49**, 692-699 (2017).

7. Antoniou, A. *et al.* Average risks of breast and ovarian cancer associated with BRCA1 or BRCA2 mutations detected in case Series unselected for family history: a combined analysis of 22 studies. *Am J Hum Genet* **72**, 1117-1130 (2003).

8. Alkan, C., Coe, B. P. & Eichler, E. E. Genome structural variation discovery and genotyping. *Nature Rev. Genet.* **12**, 363-376 (2011).

9. Medvedev, P., Stanciu, M. & Brudno, M. Computational methods for discovering structural variation with next-generation sequencing. *Nat. Methods* **6**, S13-S20 (2009).

10. Zheng, G. X. Y. *et al.* Haplotyping germline and cancer genomes with high-throughput linked-read sequencing. *Nat Biotech* **34**, 303-311 (2016).

11. Teague, B. *et al.* High-resolution human genome structure by single-molecule analysis. *Proc. Natl. Acad. Sci. USA* **107**, 10848-10853 (2010).

12. Hastie, A. R. *et al.* Rapid genome mapping in nanochannel arrays for highly complete and accurate de novo sequence assembly of the complex Aegilops tauschii genome. *PLoS One* **8**, e55864 (2013).

13. Lim, A. *et al.* Shotgun optical maps of the whole Escherichia coli O157: H7 genome. *Genome Res.* **11**, 1584-1593 (2001).

14. Lai, Z. *et al.* A shotgun optical map of the entire Plasmodium falciparum genome. *Nat. Genet.* **23**, 309-313 (1999).

15. Schwartz, D. C. *et al.* Ordered restriction maps of Saccharomyces cerevisiae chromosomes constructed by optical mapping. *Science* **262**, 110-114 (1993).

16. Lin, J. *et al.* Whole-genome shotgun optical mapping of Deinococcus radiodurans. *Science* **285**, 1558-1562 (1999).

17. Reisner, W., Pedersen, J. N. & Austin, R. H. DNA confinement in nanochannels: physics and biological applications. *Rep. Prog. Phys.* **75**, 106601 (2012).

18. Branton, D. *et al.* The potential and challenges of nanopore sequencing. *Nat. Biotechnol.* **26**, 1146-1153 (PMCID: PMC2683588) (2008).

19. Wanunu, M. Nanopores: A journey towards DNA sequencing. *Phys Life Rev* **9**, 125-158 (2012).

20. Reisner, W. *et al.* Single-molecule denaturation mapping of DNA in nanofluidic channels. *Proc. Natl. Acad. Sci. USA* **107**, 13294-13299 (2010).

21. Riehn, R. *et al.* Restriction mapping in nanofluidic devices. *Proc. Natl. Acad. Sci. USA* **102**, 10012-10016 (2005).

22. Jung, Y., Kim, J., Jun, S. & Ha, B.-Y. Intrachain Ordering and Segregation of Polymers under Confinement. *Macromolecules* **45**, 3256-3262 (2012).

23. Pendleton, M. *et al.* Assembly and diploid architecture of an individual human genome via single-molecule technologies. *Nat. Methods* **12**, 780-786 (2015).

24. Mostovoy, Y. *et al.* A hybrid approach for de novo human genome sequence assembly and phasing. *Nat. Methods* **13**, 587-590 (2016).

25. Zhou, J. *et al.* Enhanced nanochannel translocation and localization of genomic DNA molecules using three-dimensional nanofunnels. *Nat. Commun.* **8**, 807 (2017).

26. Menard, L. D. & Ramsey, J. M. Electrokinetically-Driven Transport of DNA through Focused Ion Beam Milled Nanofluidic Channels. *Anal. Chem.* **85**, 1146-1153 (2013).

27. Menard, L. D. & Ramsey, J. M. The fabrication of sub-5-nm nanochannels in insulating substrates using focused ion beam milling. *Nano Lett.* **11**, 512-517 (2011).

28. Menard, L. D., Mair, C. E., Woodson, M. E., Alarie, J. P. & Ramsey, J. M. A device for performing lateral conductance measurements on individual double-stranded DNA molecules. *ACS Nano* **6**, 9087-9094 (PMCID: PMC3482132) (2012).

29. Iancu, V. *et al.* Polaronic Transport and Current Blockades in Epitaxial Silicide Nanowires and Nanowire Arrays. *Nano Lett.* **13**, 3684−3689 (NIHMS ID: NIHMS512702) (2013).

30. Ramsey, J. M., Menard, L. & Gorbounov, V. Methods, systems, and devices for forming nanochannels. (2010). Patent.

31. Ramsey, J. M. & Menard, L. Nanofluidic devices for the rapid mapping of whole genomes and related systems and methods of analysis. (2016). Patent.

32. Menard, L. D., Ramsey, J. M., Zhou, J., Rubinstein, M. & Panyukov, S. Devices with fluidic nanofunnels, associated methods, fabrication and analysis systems. (2012). Patent.

33. Menard, L. D., Ramsey, J. M., McCrate, O. A. & Tycon, M. A. Fluidic devices with nanoscale manifolds for molecular transport, related systems and methods of analysis. (2015). Patent.

34. Menard, L. D. & Ramsey, J. M. Nanofluidic devices with integrated components for the controlled capture, trapping, and transport of macromolecules and related methods of analysis. (2013). Patent.

35. Genturi Inc, https://www.genturi.com/. Accessed - 6/16/2019. Web.

36. Pyle, J. R., Piecco, K. W. E. S., Vincente, J. R. & Chen, J. Optical Genome Mapping. *Encyclopedia of Chemical Processing* **Preprint** (2018).

37. Cao, H., Tegenfeldt, J. O., Austin, R. H. & Chou, S. Y. Gradient nanostructures for interfacing microfluidics and nanofluidics. *Appl. Phys. Lett.* **81**, 3058-3060 (2002).

38. Reisner, W. *et al.* Statics and dynamics of single DNA molecules confined in nanochannels. *Phys. Rev. Lett.* **94**, 196101 (2005).

39. Wang, Y., Tree, D. R. & Dorfman, K. D. Simulation of DNA Extension in Nanochannels. *Macromolecules* **44**, 6594-6604 (2011).

40. Yoon, J. Y. & Garrell, R. L. Preventing Biomolecular Adsorption in Electrowetting-Based Biofluidic Chips. *Anal Chem* **75**, 5097-5102 (2003).

41. Napoli, M., Eijkel, J. C. & Pennathur, S. Nanofluidic technology for biomolecule applications: a critical review. *Lab Chip* **10**, 957-985 (2010).

42. Tegenfeldt, J. O. *et al.* Micro- and nanofluidics for DNA analysis. *Analytical & Bioanalytical Chemistry* **378**, 1678-1692 (2004).

43. Rodriguez, I. & Li, S. F. Y. Surface deactivation in protein and peptide analysis by capillary electrophoresis. *Anal Chim Acta* **383**, 1-26 (1999).

44. Persson, F. *et al.* Lipid-based passivation in nanofluidics. *Nano Lett.* **12**, 2260-2265 (2012).

45. Uba, F. I. *et al.* Surface charge, electroosmotic flow and DNA extension in chemically modified thermoplastic nanoslits and nanochannels. *Analyst* **140**, 113-126 (2015).

46. Gavish, N. Poisson–Nernst–Planck equations with steric effects — non-convexity and multiple stationary solutions. *Physica D: Nonlinear Phenomena* **368**, 50-65 (2018).

47. Sparreboom, W., van den Berg, A. & Eijkel, J. C. T. Transport in nanofluidic systems: a review of theory and applications. *New Journal of Physics* **12** (2010).

48. van Hal, R. E. G., Eijkel, J. C. T. & Bergveld, P. A general model to describe the electrostatic potential at electrolyte oxide interfaces. *Advances in Colloid and Interface Science* **69**, 31-62 (1996).

49. Mela, P. *et al.* The zeta potential of cyclo-olefin polymer microchannels and its effects on insulative (electrodeless) dielectrophoresis particle trapping devices. *Electrophoresis* **26**, 1792-1799 (2005).

50. Schoch, R. B., Han, J. & Renaud, P. Transport phenomena in nanofluidics. *Rev. Mod. Phys.* **80**, 839-883 (2008).

51. Plecis, A., Schoch, R. B. & Renaud, P. Ionic transport phenomena in nanofluidics: experimental and theoretical study of the exclusion-enrichment effect on a chip. *Nano Lett* **5**, 1147-1155 (2005).

52. Zangle, T. A., Mani, A. & Santiago, J. G. Theory and experiments of concentration polarization and ion focusing at microchannel and nanochannel interfaces. *Chem. Soc. Rev.* **39**, 1014-1035 (2010).

53. Pu, Q. S., Yun, J. S., Temkin, H. & Liu, S. R. Ion-enrichment and ion-depletion effect of nanochannel structures. *Nano Lett* **4**, 1099-1103 (2004).

54. Jorgenson, J. W. & Lukacs, K. D. Capillary zone electrophoresis. *Science* **222**, 266-272 (1983).

55. Manz, A. *et al.* Electroosmotic pumping and electrophoretic separations for miniaturized chemical analysis systems. *J. Micromech. Microeng.* **4**, 257-265 (1994).

56. Lee, T. T., Dadoo, R. & Zare, R. N. Real-Time Measurement of Electroosmotic Flow in Capillary Zone Electrophoresis. *Anal. Chem.* **66**, 2694-2700 (1994).

57. Kaneta, T., Ueda, T., Hata, K. & Imasaka, T. Suppression of electroosmotic flow and its application to determination of electrophoretic mobilities in a poly(vinylpyrrolidone)-coated capillary. *J. Chromatogr. A* **1106**, 52-55 (2006).

58. Gupta, D. *et al.* Experimental evidence of weak excluded volume effects for nanochannel confined DNA. *ACS Macro Lett.* **4**, 759-763 (2015).

59. Persson, F. & Tegenfeldt, J. O. DNA in nanochannels--directly visualizing genomic information. *Chem. Soc. Rev.* **39**, 985-999 (2010).

60. Reccius, C. H., Stavis, S. M., Mannion, J. T., Walker, L. P. & Craighead, H. G. Conformation, Length, and Speed Measurements of Electrodynamically Stretched DNA in Nanochannels. *Biophys. J.* **95**, 273-286 (2008).

61. Viovy, J. L. Electrophoresis of DNA and other polyelectrolytes: Physical mechanisms. *Rev. Mod. Phys.* **72**, 813-872 (2000).

62. Olivera, B. M., Baine, P. & Davidson, N. Electrophoresis of the nucleic acids. *Biopolymers* **2**, 245-257 (1964).

63. Slater, G. W. *et al.* Theory of DNA electrophoresis: A look at some current challenges. *Electrophoresis* **21**, 3873-3887 (2000).

64. Luan, B. *et al.* Tribological Effects on DNA Translocation in a Nanochannel Coated with a Self-Assembled Monolayer. *J. Phys. Chem. B* **114**, 17172-17176 (2010).

65. Belotserkovskii, B. P. & Johnston, B. H. Denaturation and association of DNA sequences by certain polypropylene surfaces. *Anal Biochem* **251**, 251-262 (1997).

66. Budker, V. G., Godovikov, A. A., Naumova, L. P. & Slepneva, I. A. Interaction of polynucleotides with natural and model membranes. *Nucleic Acids Res* **8**, 2499-2515 (1980).

67. MacKerell Jr., A. D. Influence of magnesium ions on duplex DNA structural, dynamic, and solvation properties. *J. Phys. Chem. B* **101**, 646 (1997).

68. Cowan, J. A. *The Biological Chemistry of Magnesium*. (1995).

69. Buckin, V. A., Kankiya, B. I., Rentzeperis, D. & Marky, L. A. Mg2+ Recognizes the Sequence of DNA through Its Hydration Shell. *J Am Chem Soc* **116**, 9423-9429 (1994).

70. Sweryda-Krawiec, B., Devaraj, H., Jacob, G. & Hickman, J. J. A new interpretation of serum albumin surface passivation. *Langmuir* **20**, 2054-2056 (2004).

71. Yusko, E. C. *et al.* Controlling protein translocation through nanopores with bio-inspired fluid walls. *Nat Nanotechnol* **6**, 253-260 (2011).

72. Rye, H. S. *et al.* Stable fluorescent complexes of double-stranded DNA with bis-intercalating asymmetric cyanine dyes: properties and applications. *Nucleic Acids Res.* **20**, 2803-2812 (1992).

73. Sinden, R. R. *DNA Structure and Function*. (1994).

74. Gupta, D. *et al.* Mixed confinement regimes during equilibrium confinement spectroscopy of DNA. *J. Chem. Phys.* **140**, 214901 (2014).

75. Stigter, D. Interactions of Highly Charged Colloidal Cylinders with Applications to Double-Stranded DNA. *Biopolymers* **16**, 1435-1448 (1977).

76. Persson, F., Utko, P., Reisner, W., Larsen, N. B. & Kristensen, A. Confinement spectroscopy: probing single DNA molecules with tapered nanochannels. *Nano Lett.* **9**, 1382-1385 (2009).

77. Dobrynin, A. V. Effect of counterion condensation on rigidity of semiflexible polyelectrolytes. *Macromolecules* **39**, 9519-9527 (2006).

78. Odijk, T. On the Statistics and Dynamics of Confined or Entangled Stiff Polymers. *Macromolecules* **16**, 1340-1344 (1983).

79. Daoud, M. & Degennes, P. G. Statistics of Macromolecular Solutions Trapped in Small Pores. *J. Phys. (Paris)* **38**, 85-93 (1977).

80. Odijk, T. Scaling theory of DNA confined in nanochannels and nanoslits. *Phys. Rev. E* **77**, 060901 (2008).

81. Brochard-Wyart, F. & Raphael, E. Scaling Theory of Molten Polymers in Small Pores. *Macromolecules* **23**, 2276-2280 (1990).

82. Structural Variation, https://bionanogenomics.com/technology/structural-variation/. Accessed – 7/2/2019. Web.

CHAPTER 2: DNA EXTENSION IN THE EXTENDED DE GENNES REGIME

2.1 – Introduction

A variety of current and proposed future platforms leverage the extension of DNA molecules in fluidic nanochannels to enable long-range mapping of genomic and epigenomic information.[1-7] Optimization of these platforms will be facilitated by a greater understanding of molecular behavior under various degrees of confinement in nanochannels. Early experiments measuring double-stranded DNA molecule extension were discussed in the context of the classic Odijk and de Gennes models of strong and weak DNA confinement, respectively.[8-11] The Odijk model describes confinement in nanochannels having critical dimensions smaller than the DNA persistence length, where DNA behaves as a series of deflecting rigid rods.[9] The de Gennes model — appropriate when nanochannel critical dimensions are significantly greater than the DNA persistence length but less than the molecule's radius of gyration — describes extension of a polymer along the longitudinal axis of the nanochannel as a string of non-interpenetrating spherical blobs.[8] Most experiments investigating the nanochannel confinement of double-stranded DNA, however, have used nanochannels with critical dimensions between these regimes, giving rise to transitional behavior that has required extending the classic theories to model. In moving from strong confinement (Odijk) to weak confinement (de Gennes), two primary transitional regimes have been proposed. As the nanochannel dimensions begin to increase the energy of DNA backfolding approaches k_BT, giving rise to hairpin formation along the DNA molecule, an effect that can be described by a global persistence length greater than the molecule's intrinsic persistence length.[12-16] As nanochannel dimensions increase further, the DNA molecule has room to coil and the impact of channel walls on molecular alignment decreases. Extension is no longer dominated by chain deflection but is driven by excluded volume interactions, marking a transition to a blob model. For nanochannel diameters only marginally greater than the molecule's persistence length, however, the excluded volume interactions within each blob have energy less than k_BT and intrablob conformations thus deviate from real-chain behavior described by Flory statistics.[12,17-19] The blobs are anisometric with a length along the

nanochannel longitudinal axis that is greater than the confining nanochannel critical dimensions (blob diameter).[12,19] DNA extension in this anisometric blob regime follows the same scaling relationship as expected in the de Gennes regime and the regime has thus been termed the "extended de Gennes" regime.[13,19] *Doyle et al.* noted that the extended de Gennes model of a polymer confined in a nanochannel is analogous to that of semidilute solutions in marginal solvents.[18]

Numerous studies have modeled DNA extension across these multiple conformational regimes. The full spectrum of behavior is not captured by a single power law scaling relationship.[13,18,20] In the Odijk regime, DNA extension (R) weakly increases with decreasing nanochannel size as the deflection angle is reduced:

$$R_{Odijk} = L_c \left[1 - A \left(\frac{D_{eff}}{P} \right)^{2/3} \right] \quad (1)$$

where L_c is the end-to-end contour length, A is a geometry-dependent constant ($A \approx 0.18$ for a square channel), and P is the persistence length.[11,21] As nanochannel dimensions increase and confinement decreases, extension approaches $R \sim D_{eff}^{-1}$.[13,20] In both the classic and extended de Gennes regimes, DNA equilibrium extension (R) is expected to scale as

$$R_{de\ Gennes, extended\ de\ Gennes} \sim L_c\ (wP)^{1/3} D_{eff}^{-2/3} \quad (2)$$

where w is the effective width of the DNA molecule (including electrostatic effects).[8,13,18,19] Most experimental studies of DNA extension in nanochannels of various sizes have utilized nanochannels deemed sufficiently large that conformations described by the extended de Gennes model were expected. In these past studies, however, fitting the experimental data to a single power equation resulted in exponents ranging from -0.76 to -0.86, a significant deviation from theory and simulations.[11,22-25] Potential sources of error that have been noted include inaccuracies in the characteristic polymer and device lengths used in the analyses (w, P, D_{eff}), length distributions in relatively long DNA samples, nanochannel aspect ratios, and the range of nanochannel sizes over which data is analyzed.[13-15,22-33] Each of these elements is discussed below in a comparison of present and past results.

2.2 – Experimental

In order to investigate the extension of DNA molecules in nanochannels having various critical dimensions and aspect ratios, focused ion beam (FIB) milling was used as previously described to fabricate devices having fifteen nanochannels connected in series in which individual DNA molecules could be measured (Fig. 2.1).[34-36] While it is a relatively low throughput fabrication method, FIB milling has the advantage over lithography and etching techniques in being able to precisely alter both the nanochannel widths (area scanned by the beam) and depths (number of beam passes) in a single device. The nanofluidic device was fabricated from a 4" x 4" x 0.090" fused quartz substrate (Telic Corp. Valencia, CA) pre-coated with AZ1518 photoresist and chromium. Standard photolithography and wet etching techniques were used to create microchannels and a frustoconical nanochannel entrance (Figure 2.1A). The microchannels post-etch were profiled (P-15 profilometer, KLA Tencor, Milpitas, CA) and had a depth of 5 μm. A 100 nm thick chromium sacrificial layer was ion sputtered (Model IBS/e, South Bay Technology) onto the quartz substrate in preparation for focused ion beam milling the nanochannel structures. Nanofluidic channels were milled through the sacrificial layer with a FEI Helios Nanolab 600 DualBeam instrument, using a custom script to enable fine dimensional control (Figure 2.1B). These nanochannels are arranged in a parallel array and are connected through relatively wide and deep perpendicular endcaps. FIB milling was also used to create a nanoslit array from the gate microchannel to the measurement nanochannel to assist in electrokinetic injection of the DNA sample.[37] Next, the milled quartz substrate was coated with a protective photoresist (S1813, Microchem Corp, Westborough, MA) and power blasted (MB-1000-1, Comco, Inc, Burbank, CA) to create vias for fluidic transport. Afterwards the photoresist was stripped with acetone and the sacrificial chromium layer removed with a chromium etchant (Chromium 1020, Transene Corp, Danvers, MA). The quartz chip was then subjected to a cleaning regimen consisting of 2x Nanostrip (KMG Chemicals), acetone, methanol, and the organic solvent trichloroethylene (Fisher Electronic Grade) to remove debris and ensure fidelity. Vias were powder blasted from the back side of each device at the ends of the microchannels demarcated by the circular features in Figure 2.1A. Prior to bonding, each nanochannel's dimensions were measured using scanning electron microscopy (SEM) and atomic force microscopy (AFM) with a high-aspect-ratio probe. Figures 2.5-2.8 show the SEM images and AFM traces of each device used in this Chapter. As shown in

Figure 2.1C, each array consisted of nanochannels with various widths *and* depths. Figure 2.2 shows how the aspect ratio profiles of each of the three devices differed. After SEM and AFM measurements, the devices were cleaned and fusion bonded to fused silica coverslips at 1000 °C to form the networks of fluidic micro- and nanochannels.

The equilibrium extension lengths of individual T4-phage DNA molecules (165.6 kbp, Wako Chemicals) were measured in 1X TE buffer (10 mM Tris base, 1 mM EDTA, pH 7.9, Thermo Fisher). Beta-mercaptoethanol was added to the buffer (4% w/v, Themo Fisher) to reduce photoinduced damage in the system and 2% w/v polyvinylpyrrolidone (10kDA, Sigma-Aldrich) was added to reduce electroosmotic flow. The pH of the resulting solution was lowered to 6.8 by these additions and the conductivity was 1020 μS/cm at 25°C. The ionic strength of the solution (13.6 mM) was calculated from equilibrium molar concentrations and ionic charges and validated by comparing the measured solution conductivity to that calculated using the Nernst-Einstein equation, with the expected and measured conductivities differing by ~10%. DNA was stained with YOYO-1 intercalating dye (Thermo Fisher Scientific) at a 1:5 dye:base pair ratio for fluorescent imaging.

Single DNA molecules were electrokinetically transported from the sample microchannel into the initial nanochannel segment, at which point the voltages were turned off, the shutter of the excitation source was closed to avoid unnecessary photodamage, and the DNA molecule was allowed to relax for 60 seconds. The shutter was then opened, and the nanochannel-confined DNA molecule was imaged for 30 seconds at 10 frames/second using an EMCCD camera (Photometrics Cascade II). After image collection, the DNA molecule was electrokinetically transported to the next nanochannel segment where the processes of relaxation and imaging were repeated until all channels had been explored. The molecule's end positions at each time point were determined from the images using a MATLAB program.[38] The program extracted the highest intensity line profile along the DNA extension (*i.e.*, nanochannel) axis and the highest intensity point and baseline intensity levels along the profile. The ends of the molecule were identified as the extents of the profile that exceeded a threshold above baseline of 10%. This avoided truncating skewed distributions that occurred due to internal fluctuations captured at a particular time point. Control experiments where DNA molecules were repeatedly measured in the third nanochannel of a device, with intervening transport to the fourth nanochannel and back to the third

nanochannel to mimic the illumination dose, transport, and relaxation timescales of the actual experiments showed no significant dependence of DNA extension length on exposure time to the excitation source.

High-molecular-weight DNA molecules, such as T4-phage DNA, inherently experience some degree of shearing during preparation and handling.[39] Analyses in this Letter were constrained to molecules that showed extension lengths greater than 20 μm in nanochannels where D_{eff}~200 nm, corresponding to nearly intact (minimally sheared) T4-phage DNA molecules.[25,40] Past studies and the present study generally measure tens of molecules per condition.[22,24-26] The approach described here of measuring each molecule in a series of channels eliminates sampling errors from a population of molecules that, while nominally monodisperse, has a distribution of contour lengths.[22-26,41]

2.3 – Discussion

Figure 2.3a shows the average DNA extension length measured for ten molecules in each of the three nanochannel devices and is the main result of this Letter. Power law fits to the data are plotted as solid lines, yielding scaling relationships of $R \sim D_{eff}^{-0.67\pm0.04}$ (Device 1), $R \sim D_{eff}^{-0.68\pm0.05}$ (Device 2), and $R \sim D_{eff}^{-0.70\pm0.05}$ (Device 3), where the uncertainties represent 95% confidence intervals of the fit. These results are consistent with the extended de Gennes theory (Equation 2) and with simulations performed for rectangular ($R \sim D_{eff}^{-0.71\pm0.01}$) and square ($R \sim D_{eff}^{-0.69\pm0.03}$, $R \sim D_{eff}^{-0.695\pm0.004}$, $R \sim D_{eff}^{-0.72\pm0.01}$) profile nanochannels, which tend to predict a slightly stronger scaling.[13,18,25] For rectangular nanochannels with modest aspect ratios (*e.g.*, less than 5), simulations suggest that the use of the geometric mean of nanochannel width and depth reproduces the behavior of square channels.[15,24,25] Furthermore, as both the DNA molecule and the silica surfaces of the nanochannel walls are negatively charged, the nanochannel dimensions are effectively reduced by a depletion length, δ, originating from electrostatic repulsions.[13,27] The relevant critical dimension, D_{eff}, is thus given by Equation 3.

$$D_{eff} = \sqrt{(width - \delta)(depth - \delta)} \tag{3}$$

Previous experimental studies have omitted this depletion length,[11,22,23] or used the ionic strength dependent effective width, w, of the DNA molecule to approximate it.[24-26] Strictly speaking, the effective width, w, describes the excluded volume of charged cylinders representing local segments of the DNA molecule,[42] not the exclusion of a charged cylinder from a charged planar surface. A recent experimental study utilized a commercial nanochannel platform to assess hundreds of thousands of DNA molecules extended in nanochannels with well characterized dimensions in buffers with a range of ionic strengths, finding the relationship $\delta = 6.5\lambda_D - 0.64$, where λ_D is the Debye length.[27] We use this relationship to calculate δ=17.1 nm in the present study. We note, however, that the effective DNA width is calculated to be 13.8 nm in our buffer and that our results change marginally if we use $\delta = w$ (*i.e.*, the scaling exponents decrease by 0.005).

The dashed line in Figure 2.3a is an exact solution derived for DNA extension in the extended de Gennes regime (Equation 4).[43]

$$R_{extended\ de\ Gennes} = 1.1765\ L\ (wP)^{1/3} D_{eff}^{-2/3} \quad (4)$$

As this is an exact solution to mean-field arguments, in contrast to Flory mean-field approximations for an unconfined polymer, it does not require correcting the Flory exponent (ν = 3/5) with the value of 0.588 for a real chain in free solution. Such a correction has been alluded to in past reports of nanochannel confinement as it yields a predicted scaling of $R \sim D_{eff}^{-0.702}$, a result in closer agreement with simulation results.[18] In any case, the experimental results presented here are insufficiently precise to confidently make this distinction. To evaluate Equation 4, we used a contour length, L, of 71.7 µm; [26,38] an effective DNA width, w, of 13.8 nm; and a persistence length, P, of 62.6 nm. As in other studies, the effective width was calculated from the buffer ionic strength using the equation of Stitger.[42] Similarly, the persistence length was calculated from the buffer ionic strength using the empirical formula of Dobrynin.[44] Constraining the fits to the experimental data such that $R \sim D_{eff}^{-2/3}$ yields an average prefactor of 1.058±0.009. The 10% lower value for the experimental data compared to Equation 4 could be attributed to inaccuracies in the values of L, w, and P used for the calculation; however, the likely primary factor is the reality that the average extension lengths are measured from a population of molecules that include partially sheared T4-phage DNA. As described above, a coarse size selection process is employed but some degree of shearing is inevitable in samples of high-molecular-weight DNA. Important to note is that the exact values of w, P, and L used in the analysis do not affect the scaling relationship.

A prominent feature of the data analysis represented in Figure 2.3a is that some of the experimental data points have been excluded from the analysis — specifically data from the two smallest channels of Devices 1 and 2 and the four smallest channels of Device 3. We note that this removes data from some of the highest aspect ratio channels in Device 3, but the fact that large channels with aspect ratios greater than 2 (Device 2) do not systematically deviate from the power law fit suggests that absolute nanochannel dimensions may play a role. Figure 2.3b shows the nanochannel widths and depths for each of the 45 channels in which DNA molecules were measured and compares these dimensions to those reported in past experimental DNA confinement studies. The transitions between

the confinement regimes discussed above are gradual and consequently the data used for a single power law fit should be chosen such that regime mixing is minimized. The extended de Gennes regime has been predicted to apply in nanochannels with dimensions where $2P \ll D_{eff} \ll 4P^2/w$.[18] As these are strong inequalities, one would predict a degree of regime mixing if these limits were taken as the experimental limits defining the range of D_{eff}. Regime-crossing simulations provide more practical limits, namely the critical D_{eff} values where simulation results for the extended de Gennes regime begin to significantly deviate from theoretical expectations.[13-15,20,24,25] Implementing such treatments have found the lower limit of the extended de Gennes regime to lie at D_{eff} between 3*P and 4*P and the upper limit near $D_{eff} = 2.24\ P^2/w$.[12,18] Another estimate of the lower limit is provided by *Wang et al.* who suggest, by considering the requirement of chain flexibility within an anisometric blob, that the lower limit is $8(w/P)^{1/2}$ times the persistence length, or 3.75*P for the experimental conditions of this study.[13] Here we used a lower cutoff of 3.5*P to define the data analyzed and considered the effective widths and depths independently. This latter consideration assumes that strong confinement in one dimension imposes a perturbation to the molecule that manifests as a stronger scaling of DNA extension with the geometric mean dimension. In other words, as the smallest dimension (here depth) is sufficient to constrain backfolding of chain segments and cause hairpin tightening, it effectively increases the global persistence length under the anisotropic confinement. Odijk discusses this qualitatively and *Muralidhar et al.* simulated extension in a number of rectangular nanochannels of various depths and widths where

$$R_{rectangular} \sim L \left[\frac{wg}{D_2^{2/3} D_1 P^{1/3}}\right]^{1/3} \tag{5}$$

D_1 is the smaller nanochannel cross-sectional dimension, D_2 is the larger dimension, and g is the global persistence length.[12,15] The depths and aspect ratios of the nanochannels used in our study were bracketed by the simulations of *Muralidhar et al.* and we were able to interpolate values of g from their results, confirming that the off-trend extension lengths of Device 3 are consistent with this model of regime mixing driven by the shallow depths of the smallest nanochannels (Figure 2.10). The assumption that behavior in rectangular nanochannels can be mapped onto that in square nanochannels through use of the geometric mean is thus erroneous once one of either the nanochannel width or depth crosses a critical value. The use of 3.5*P as the lower cutoff for the extended de Gennes regime (including any

error in the exact value of P) is supported by an analysis showing that the scaling exponent reaches a consistent value when the fitting analysis for Device 3 is applied to the largest 11 channels, 10 channels, etc., down to the largest 5 channels with a value of -0.70±0.04 (mean ± standard deviation). Conversely, a power law fit to the four smallest channels of Device 3 yields a scaling exponent of -0.81±0.09. Their inclusion in the larger data set yields an exponent of -0.79±0.02, illustrating how a few data points in a transitional regime at one extent of the data series can strongly impact the results of a power law fit.

The serendipitous inclusion of the shallow nanochannels in Device 3 prompted a review of the literature with particular attention to nanochannel dimensions of previous experiments (Fig. 2.3b). Except for one study by *Gupta et al.* (discussed below), the present study is unique in exploring nanochannel dimensions — both width and depth — conservatively within the size range anticipated to produce extension according to blob theory.[25] It is also the first experimental study to show quantitative agreement with the theoretical $R \sim D_{eff}^{-2/3}$ scaling across multiple independent devices. In our comparison, we acknowledge that the values of w, P, and L vary across studies as a result of different buffers, ionic strengths, and staining ratios but also note also that each of the previous studies has been performed under conditions where the DNA persistence length is expected to be between 50-70 nm. The sub-threshold channel dimensions indicated by the grayed regions in Figure 2.3b are therefore appropriate for a comparison across studies. The scaling exponents measured from linear double-stranded DNA molecules in the other studies represented in Figure 2.3b are presented in Table 2.1. The seminal paper by *Reisner et al.* included nanochannels as small as 60 nm x 80 nm in the scaling analysis and regime mixing has been cited as an explanation for deviation from theory and stronger than expected scaling ($R \sim D_{eff}^{-0.85\pm0.05}$).[11] There are too few larger nanochannels to enable a scaling analysis wholly within the anticipated extended de Gennes regime. Similar scaling exponents ranging from -0.78 to -0.85 were reported by *Persson et al.*, who studied DNA extension in arrays of nanochannels having gradually tapering widths and a constant depth of 60 nm.[22] Slightly weaker scaling ($R \sim D_{eff}^{-0.76\pm0.05}$) was reported in a similar study by *Utko et al.*, who used deeper (150 nm) tapered nanochannels fabricated in a thermoplastic cyclic olefin copolymer.[23] We note that the nanochannel dimensions used in the analyses of these three earlier references above were physical dimensions unadjusted for a depletion length. Errors generated from this omission are expected to be relatively small (i.e., omission in our analyses results in an exponent

decrease of 0.03). *Gupta et al.* reported a study of individual molecules in a series of non-tapered nanochannels fabricated using electron beam lithography and reactive ion etching having a depth of 97 nm.[24] Accounting for a depletion length of 19 nm, this was effectively reduced to a 78 nm depth. Like the previous studies, stronger than predicted extension length scaling was observed ($R \sim D_{eff}^{-0.86 \pm 0.08}$). The consistent decreased scaling exponents in these studies suggests that the nanochannels in each are sufficiently shallow to result in increases to the global persistence length of DNA molecules to varying degrees. The global persistence length is affected by the nanochannel width in addition to its depth — as the width increases and confinement in that dimension decreases, the global persistence length approaches the molecule's bulk persistence length. Therefore, in the constant depth and varying width nanochannels extension length scaling does not conform to a single power law scaling per Equations 2, 4, or 5 because the global persistence length varies as the DNA molecules occupy different segments of the nanochannels. DNA behavior is expected to transition between regimes in this scenario.

The results by *Gupta et al.* would appear to contradict the hypothesis of regime mixing due to shallow nanochannels, with a nanochannel depth that is sufficiently larger than the lower threshold of the extended de Gennes regime (294 nm less a depletion length of 19 nm).[25] The SEM images of the nanochannels used by *Gupta et al.* that are provided in their supporting information, however, appear significantly shallower than 300 nm in our opinion. A sense of nanochannel depth can be inferred from top-down SEM images on the basis of contrast between the top surface of the substrate and the floors of the nanochannels that results from differing efficiencies in secondary electron collection. The AFM profile used by *Gupta et al.* to determine the nanochannel depth was scanned across a 2 μm wide region at the exit of the nanofunnel, rather than across the nanochannel segments themselves. The dependence of RIE etch rates on submicron feature widths (RIE lag) is a known phenomenon that may account for significant errors when using this approach. In the present study, each nanochannel that was used for DNA measurements was measured individually using both SEM and AFM. While this is absolutely necessary when using a serial fabrication process such as FIB milling, we strongly advocate for a similar approach in future channel-size-dependent studies using nanochannels fabricated by any method.

Figure 2.4 shows the end-to-end length variances of the DNA molecules in the nanochannels of each of the three devices. The variance is expected to have differing dependencies on nanochannel

dimensions in the de Gennes regime ($\sigma^2 \sim D_{eff}^{2/3}$) and extended de Gennes regime where an exact solution has been derived:

$$\sigma^2_{extended\ de\ Gennes} = 0.265\ L_c P \quad (6)$$

For this reason, it has been assessed in prior studies as a means of validating an extended de Gennes model over a classical de Gennes model under conditions of moderate confinement.[24-26,45] We present our results here to facilitate a full comparison to previous works but note that due to the significant spread in the data, neither model can be discounted with statistical significance. The dashed lines in Figure 2.4 are plots of Equation 6 using the values of L and P given above. The data show lower variances than the expected value (-20%, -25%, and -15% for Devices 1-3, respectively). Considering the extension length analysis discussed above and reflected in Figure 2.3a, we expect experimental values that are approximately 10% lower than the exact solution, assuming that the error results from an underestimation of the mean value of L_c. While we cannot confidently discriminate between the extended de Gennes and de Gennes regime on the basis of variance scaling, we note that all of the nanochannels used in this study have critical dimensions below the proposed upper size limit of the extended de Gennes range ($2.24\ P^2/w$ = 640 nm). It is also debated whether double-stranded T4-DNA molecules are sufficiently long to appreciably sample the de Gennes regime.[16]

2.4 – Conclusion

In conclusion, in studying the behavior of double-stranded DNA molecules in nanochannels where D_{eff} ranges from 220-640 nm, we report what is to our knowledge the first quantitative agreement with simulations and scaling theory describing the moderate confinement over a range of aspect ratios. Our results suggest that the inclusion of data from nanochannels with a single critical dimension below a threshold demarking a transition between conformational regimes can significantly impact the results, even if D_{eff} appears sufficiently large to permit analysis using a single model of DNA confinement. When both width and depth dimensions are above such a threshold value, the assumption that D_{eff} can be represented by their geometric mean — at least for rectangular nanochannels with modest aspect ratios — appears valid. This is consistent with findings from simulations. More broadly, the experimental results reported in this Letter are consistent with a cohesive picture of polymer confinement that has emerged in recent years through robust and comprehensive simulation and theoretical studies. We believe that the results presented here will accelerate the further experimental validation and development of these theories.

2.5 – Figures

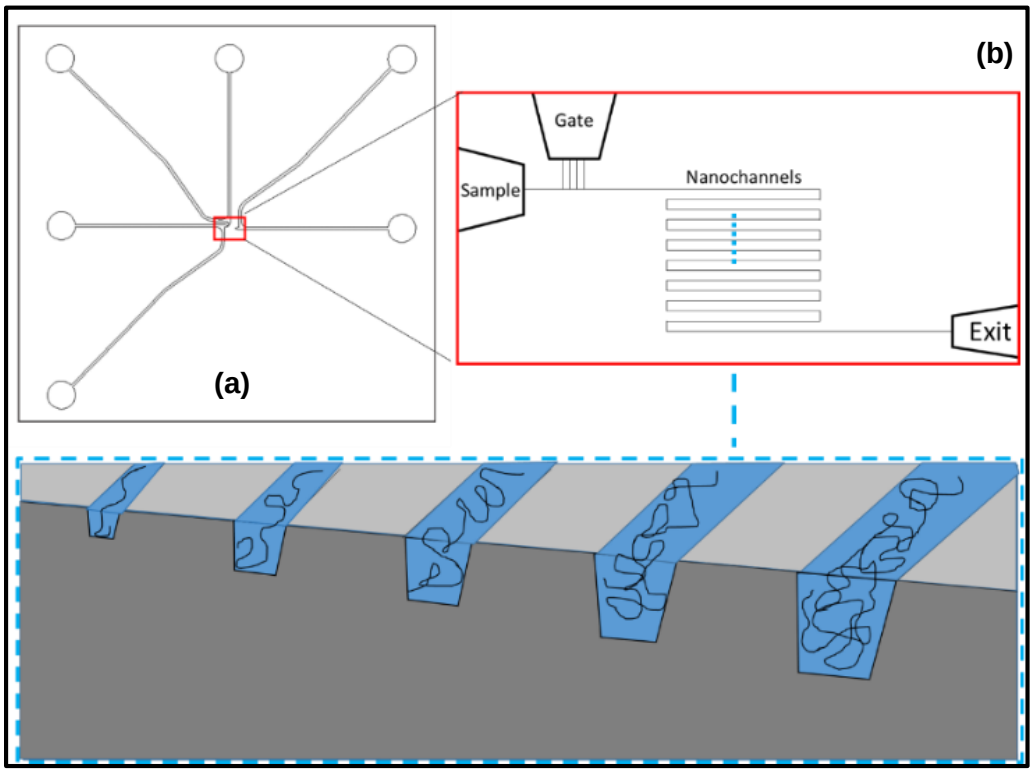

Figure 2.1: Representation of the fused silica nanofluidic DNA extension device. **(a)** illustrates the microfluidic sample, gate and exit microchannels. **(b)** shows the nanofluidic structures connecting the microfluidic segments of the device. The gate nanoslits are included to assist in electrokinetic DNA injection into the nanochannel entrance. The 15 horizontal measurement nanochannel segments in series combine to form one nanoconduit through which the DNA is transported. **(c)** is a profile view of the channels identified by the blue dashed line in (**b)**. Each horizontal nanochannel segment has a unique depth, width, and aspect ratio (width/depth).

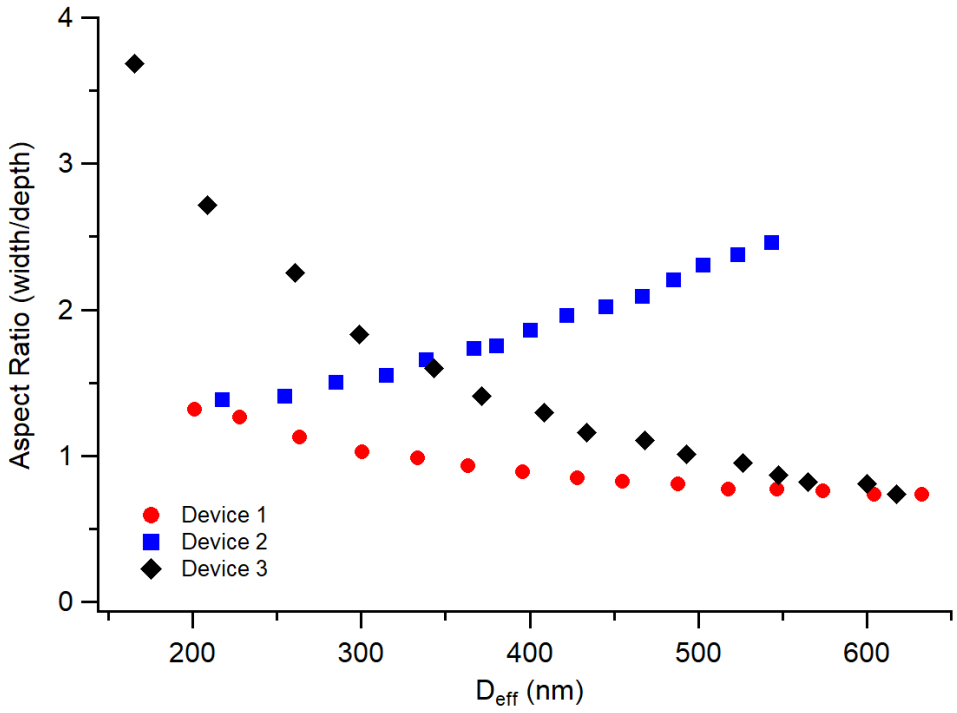

Figure 2.2: Aspect ratios (width/depth) of devices used in the present study. D_{eff} is the geometric mean of the nanochannel width and depth with each dimension reduced by a depletion length reflecting electrostatic interactions between the polyanionic DNA and the negatively charged fused silica walls: $D_{eff} = \sqrt{(\text{width} - \delta)(\text{depth} - \delta)}$. Device 1 offers the best approximation of a square cross-section across the nanochannel size range with aspect ratios ranging from 1.32 to 0.73.

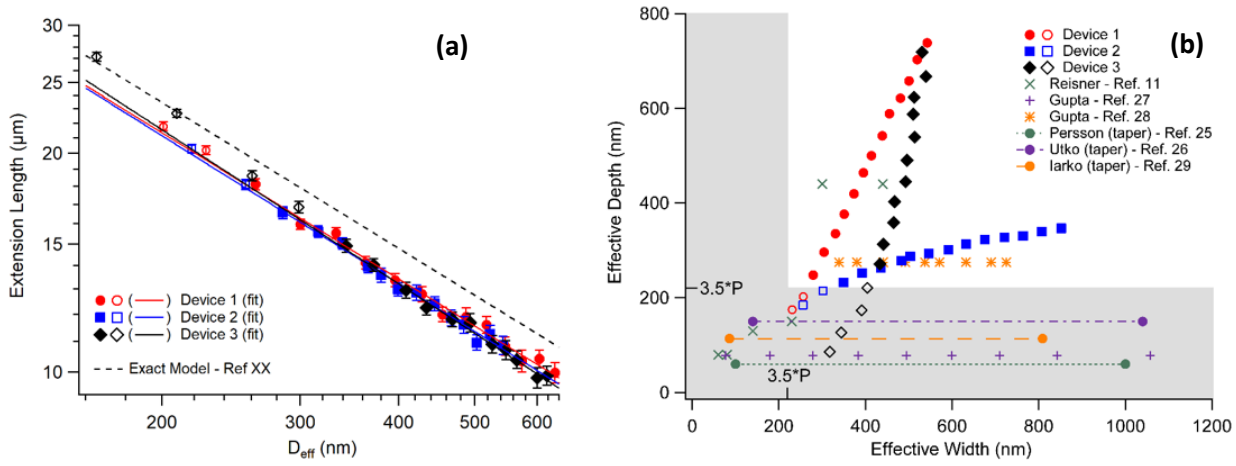

Figure 2.3: **(a)** Log-log plot of extension lengths as a function of critical nanochannel dimension (Deff). Each data point is an average of 10 molecules, with the error bars representing the standard error. Within a given device, the same population of molecules is measured in each of the fifteen nanochannels. The lines show the best power law fit to each data set. The unfilled markers are excluded from the fit as these data were collected from nanochannels with depths below a threshold value demarking the limits of the extended de Gennes regime (see text for details). The dashed line is an exact model of extension in the extended de Gennes regime reported by Werner and Mehlig (Ref. 37). The best fit scaling exponents (± 95% confidence intervals) are: Device 1: -0.67±0.04, Device 2: -0.68±0.05, Device 3: -0.70±0.05. **(b)** Comparison of dimensions of Devices 1,2, and 3 to previous works. The grayed regions indicate transitional regimes where nanochannel depth or width is less than 3.5*P. The first two channels of Devices 1 and 2 and the first four channels of Device 3 were shallower than this threshold value and were consequently omitted from the power law fits.

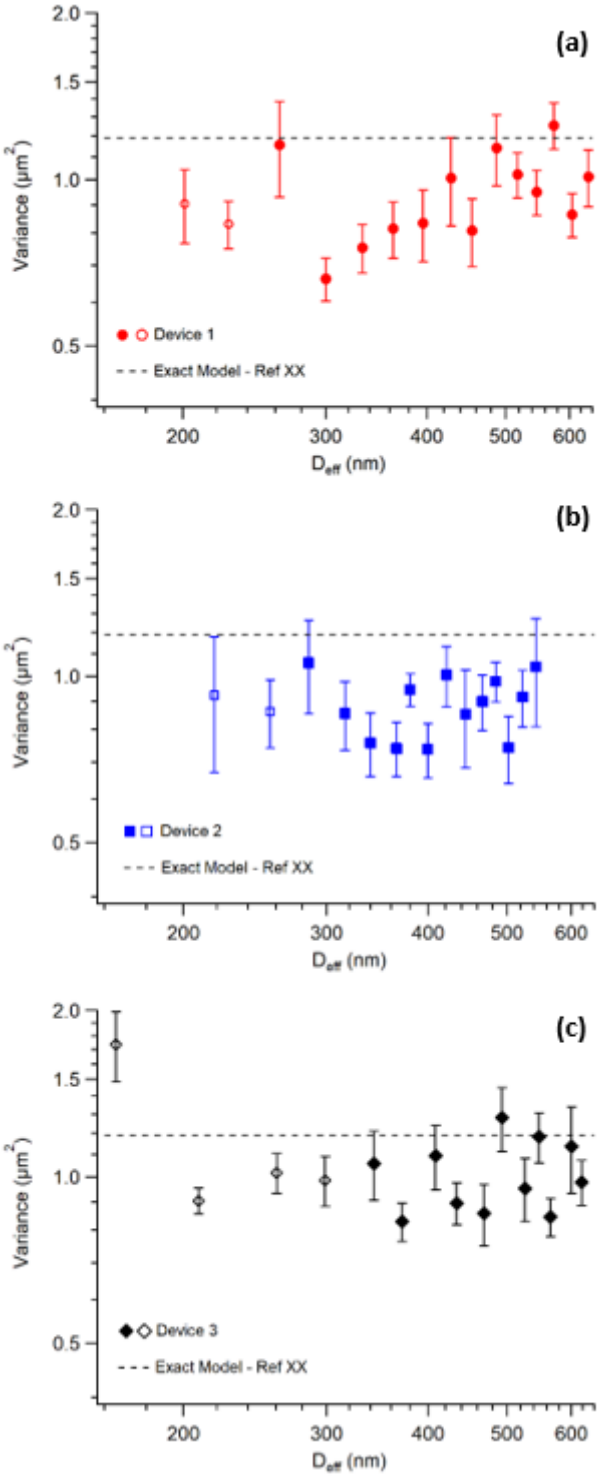

Figure 2.4: Plots of average DNA length variance vs Deff for (a) Device 1, (b) Device 2, and (c) Device 3. The conventions for unfilled symbols, error bars, and dashed lines are the same as in Figure 3a.

Device/ Reference	Scaling Exponent	DNA Sample	Buffer/Additives
Device 1	-0.67 ± 0.04 (95% CL)	T4, 1:5 YOYO-1:bp	1X TE, 4% BME, 2% PVP-10
Device 2	-0.68 ± 0.05 (95% CL)	T4, 1:5 YOYO-1:bp	1X TE, 4% BME, 2% PVP-10
Device 3	-0.70 ± 0.05 (95% CL)	T4, 1:5 YOYO-1:bp	1X TE, 4% BME, 2% PVP-10
Reisner 2005[11]	-0.85 ± 0.05 (std)	λ, 1:10 TOTO-1:bp	0.5X TE, 0.07 M BME, β-D glucose system
Persson 2009[25]	-0.85 ± 0.01 (std)	λ, 1:10 YOYO-1:bp	0.5X TBE, 3% BME, β-D glucose system
	-0.83 ± 0.01 (std)	T4, 1:5 YOYO-1:bp	0.5X TBE, 3% BME, β-D glucose system
	-0.78 ± 0.01 (std)	T4, 1:20 YOYO-1:bp	0.5X TBE, 3% BME, β-D glucose system
Utko 2011[26]	-0.76 ± 0.05 (std)	λ, 1:10 YOYO-1:bp	0.5X TBE, 3% BME
Gupta 2014[27]	-0.86 ± 0.08 (std)	λ, 1:10 YOYO-1:bp	1X Tris base, 6% BME
Gupta 2015[28]	-0.86 ± 0.03 (95% CL)	T4, 1:10 YOYO-1:bp	1X Tris base, 6% BME, 0.1% PVP-40

BME – βmercaptoethanol

β-D glucose system – 4 mg/ml β-D glucose 0.2 mg/ml glucose oxidase & 0.04 mg/ml catalase

PVP – polyvinylpyrrolidone (10 kDa or 40 kDa)

Table 2.1: Experimentally determined scaling exponents in moderate nanochannel confinement.

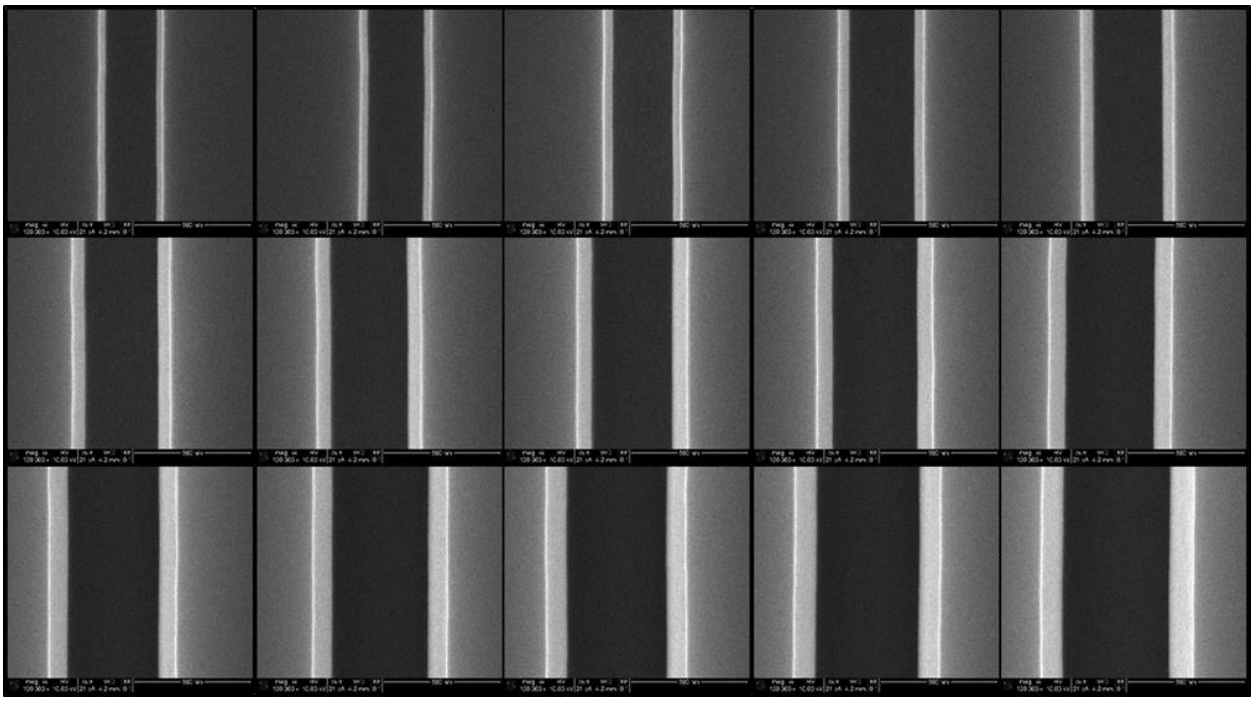

Figure 2.5: SEM images of Device 1 nanochannels.

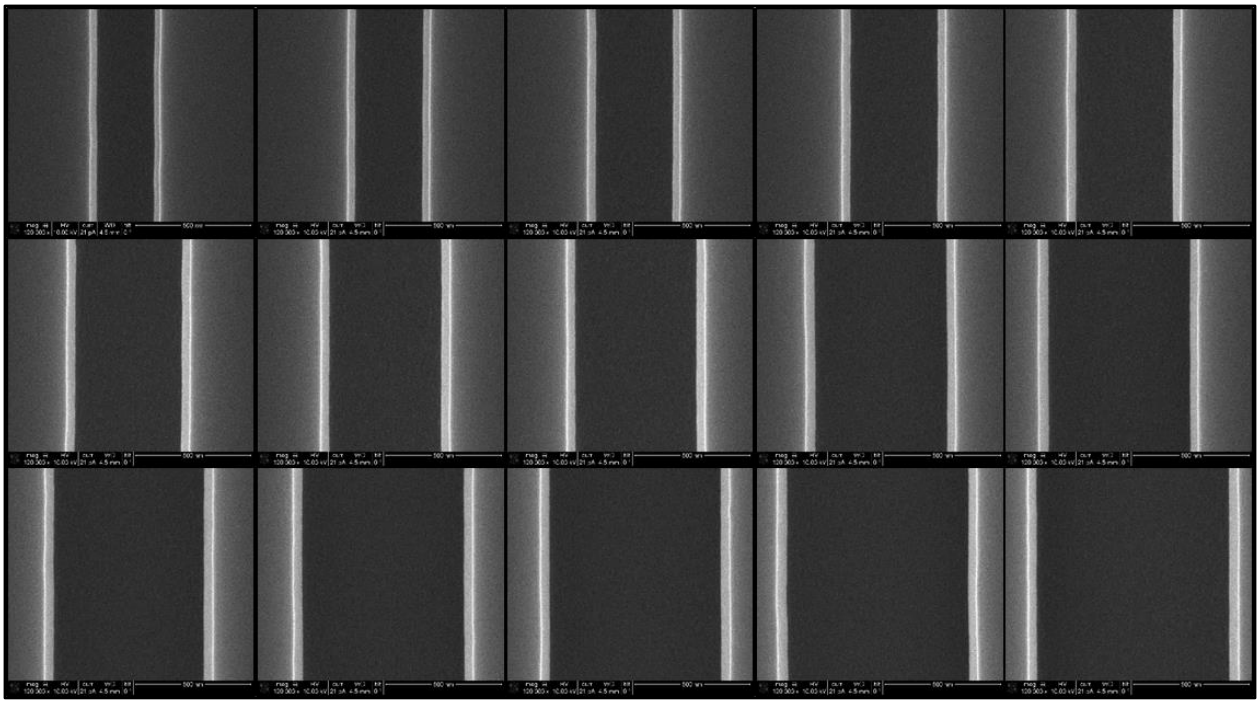

Figure 2.6: SEM images of Device 2 nanochannels.

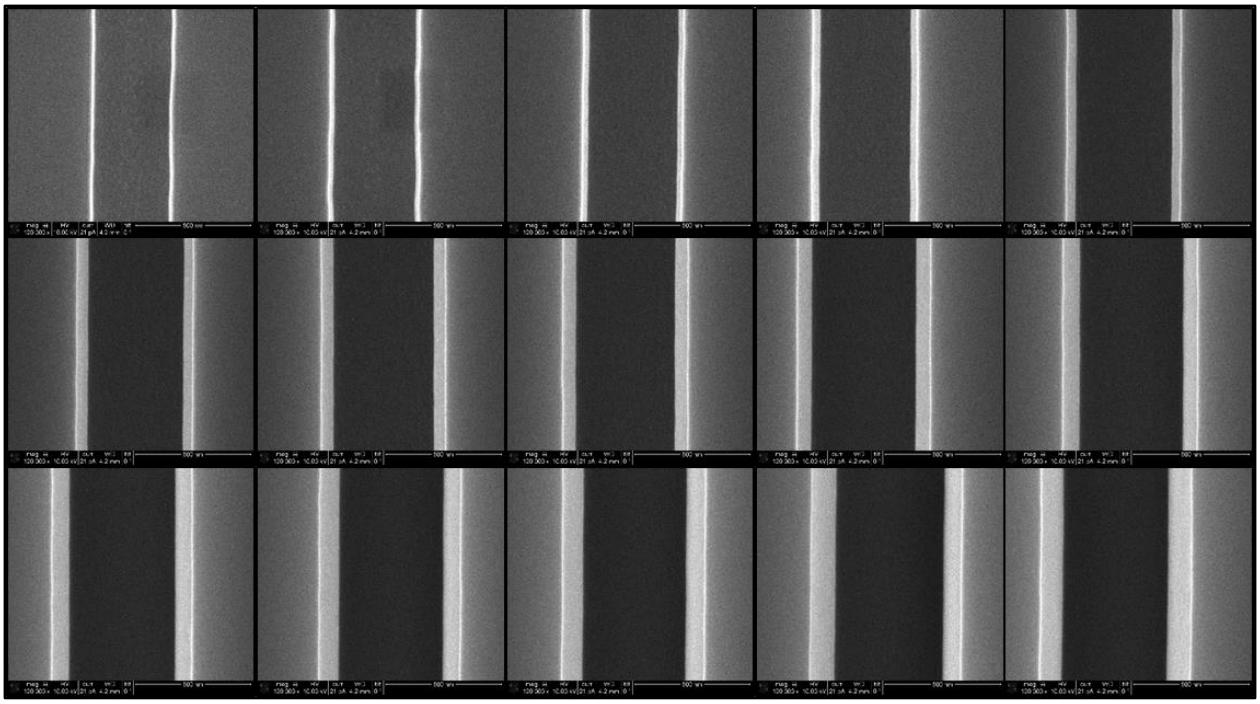

Figure 2.7: SEM images for Device 3 nanochannels.

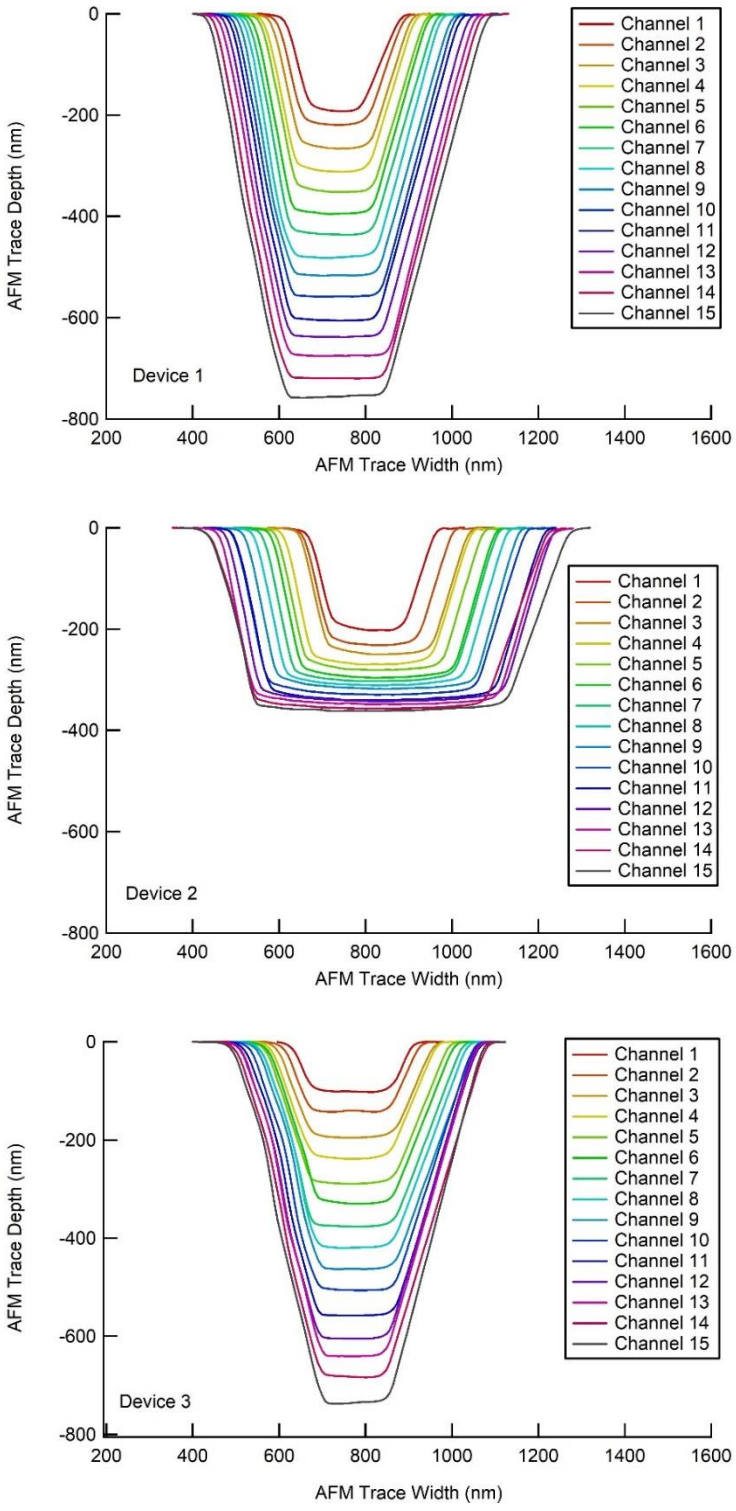

Figure 2.8: Overlaid AFM traces from Devices 1, 2, and 3. AFM standards measured pre and post device measurement indicated a <1% measurement error. AFM measurements were taken in the same locations where DNA extension would occur in subsequent experiments.

Channel (#)	Device 1 Width (nm)	Device 1 Depth (nm)	Device 2 Width (nm)	Device 2 Depth (nm)	Device 3 Width (nm)	Device 3 Depth (nm)
1	247.9	191.9	272.9	201.7	334.4	103.2
2	273.4	219.3	318.8	231.6	361.5	143.8
3	296.4	265.0	366.1	249.6	408.3	190.6
4	321.4	313.2	409.4	269.6	421.4	237.8
5	347.9	352.5	453.1	279.8	450.5	288.6
6	367.7	393.6	500.5	295.6	458.3	330.1
7	390.6	436.5	520.3	304.2	482.3	376.0
8	412.5	481.0	563.0	310.3	484.4	419.9
9	430.7	517.3	608.3	318.1	509.9	462.3
10	455.7	559.0	649.5	330.3	513.0	507.5
11	472.4	605.8	692.2	340.0	530.7	556.5
12	497.9	638.6	738.0	344.0	527.6	604.4
13	517.7	675.0	780.7	348.1	529.7	640.4
14	536.5	720.0	824.5	356.6	556.8	684.6
15	559.4	755.2	869.8	363.6	547.9	735.7

Table 2.2: Effective width and depth dimensions for Devices 1, 2, and 3, as determined by SEM and AFM measurements, respectively. These values reflect the physical dimensions minus the depletion length, δ=17.1 nm.

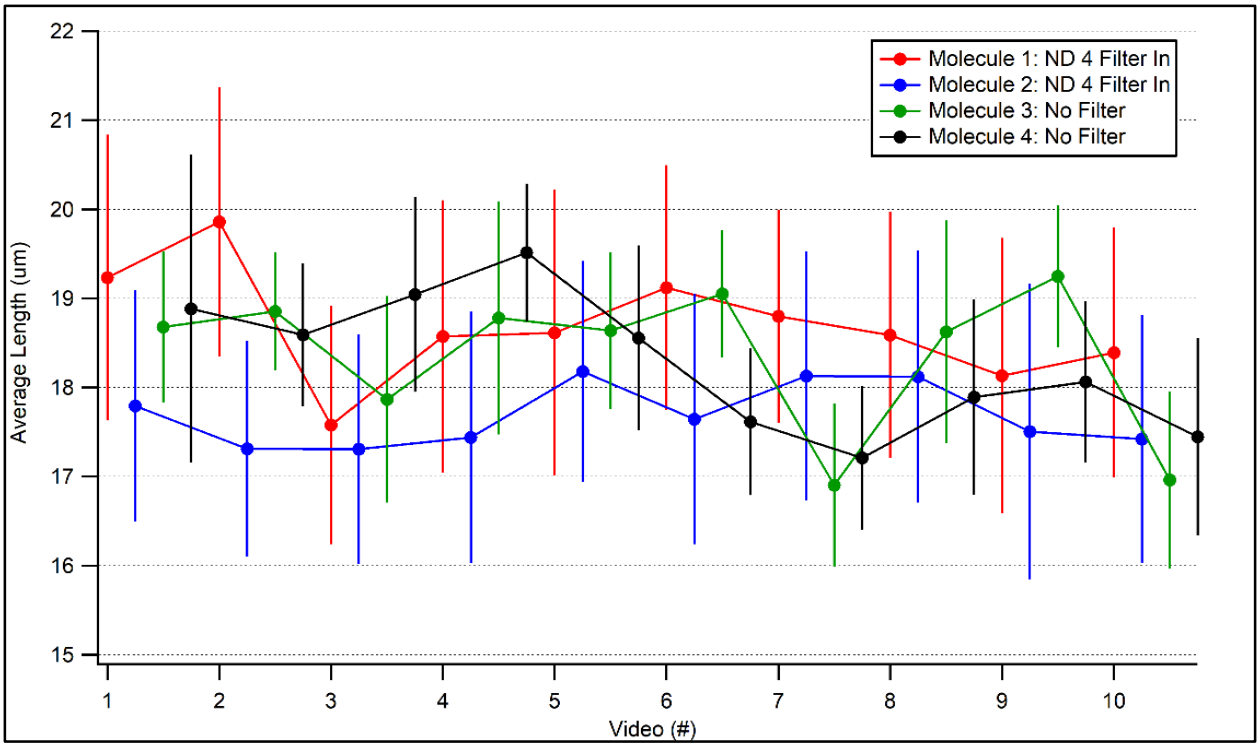

Figure 2.9: DNA Photodamage Control. Four molecules were brought into a nanochannel successively. Each molecule length was measured for 30s to obtain average end-to-end length. After measurement, the DNA molecule was electrokinetically transported into the next nanochannel before reversing the polarity to bring it back into the original channel. This was done to mimic experimental transport conditions through the nanochannel segments. This protocol was repeated 10 times for each molecule. The average DNA length was plotted to determine if prolonged exposure to 488nm light affected DNA length. The Video axis is horizontally offset for each successive molecule for ease of visualization. No trends could be reliably established from the resulting plot.

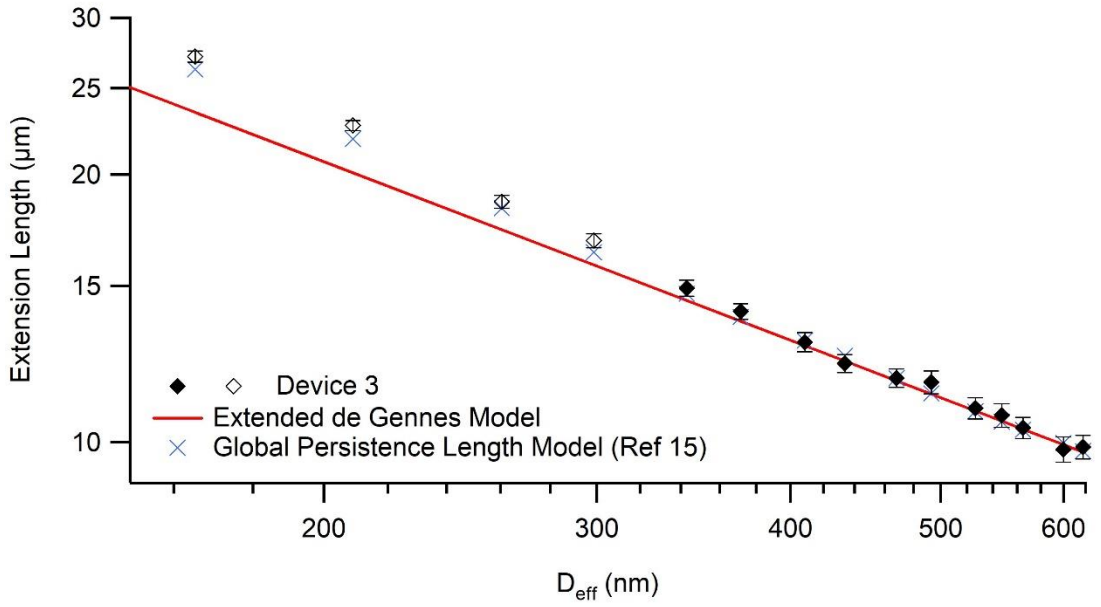

Figure 2.10**:** Expected extension in the extended de Gennes and Global Persistence Length models from *Muralidhar et al.* The global persistence length model was found from interpolating our results from their simulation, using their found values of 'g' from equation (5) in the main text. The Device 3 experimental extension lengths are in good agreement with the global persistence model for each nanochannel dimension. The difference in expected extension length between models becomes significant for the four smallest nanochannels where the nanochannel depth causes a departure from the extended de Gennes regime.

REFERENCES

1. Gabrieli, T. *et al.* Epigenetic Optical Mapping of 5-Hydroxymethylcytosine in Nanochannel Arrays. *ACS Nano* **12**, 7148-7158 (2018).

2. Zhang, D. *et al.* CRISPR-bind: a simple, custom CRISPR/dCas9-mediated labeling of genomic DNA for mapping in nanochannel arrays. (2018).

3. Reisner, W. *et al.* Single-molecule denaturation mapping of DNA in nanofluidic channels. *Proc. Natl. Acad. Sci. USA* **107**, 13294-13299 (2010).

4. Min, S. K., Kim, W. Y., Cho, Y. & Kim, K. S. Fast DNA sequencing with a graphene-based nanochannel device. *Nat. Nanotechnol.* **6**, 162-165 (2011).

5. Lam, E. T. *et al.* Genome mapping on nanochannel arrays for structural variation analysis and sequence assembly. *Nat. Biotechnol.* **30**, 771-776 (2012).

6. Hastie, A. R. *et al.* Rapid genome mapping in nanochannel arrays for highly complete and accurate de novo sequence assembly of the complex Aegilops tauschii genome. *PLoS One* **8**, e55864 (2013).

7. Lim, S. F. *et al.* DNA methylation profiling in nanochannels. *Biomicrofluidics* **5**, 34106-341068 (2011).

8. Daoud, M. & Degennes, P. G. Statistics of Macromolecular Solutions Trapped in Small Pores. *J. Phys. (Paris)* **38**, 85-93 (1977).

9. Odijk, T. On the Statistics and Dynamics of Confined or Entangled Stiff Polymers. *Macromolecules* **16**, 1340-1344 (1983).

10. Tegenfeldt, J. O. *et al.* The dynamics of genomic-length DNA molecules in 100-nm channels. *Proc. Natl. Acad. Sci. USA* **101**, 10979-10983 (2004).

11. Reisner, W. *et al.* Statics and dynamics of single DNA molecules confined in nanochannels. *Phys. Rev. Lett.* **94**, 196101 (2005).

12. Odijk, T. Scaling theory of DNA confined in nanochannels and nanoslits. *Phys. Rev. E* **77**, 060901 (2008).

13. Wang, Y., Tree, D. R. & Dorfman, K. D. Simulation of DNA Extension in Nanochannels. *Macromolecules* **44**, 6594-6604 (2011).

14. Werner, E., Persson, F., Westerlund, F., Tegenfeldt, J. O. & Mehlig, B. Orientational correlations in confined DNA. *Phys. Rev. E* **86**, 041802 (2012).

15. Muralidhar, A., Quevillon, M. J. & Dorfman, K. D. The Backfolded Odijk Regime for Wormlike Chains Confined in Rectangular Nanochannels. *Polymers* **8**, 79 (2016).

16. Chen, J. Z. Y. Self-Avoiding Wormlike Chain Confined in a Cylindrical Tube: Scaling Behavior. *Phys. Rev. Lett.* **121**, 037801 (2018).

17. Reisner, W., Pedersen, J. N. & Austin, R. H. DNA confinement in nanochannels: physics and biological applications. *Rep. Prog. Phys.* **75**, 106601 (2012).

18. Dai, L., van der Maarel, J. R. C. & Doyle, P. S. Extended de Gennes Regime of DNA Confined in a Nanochannel. *Macromolecules* **47**, 2445-2450 (2014).

19. Brochard-Wyart, F. & Raphael, E. Scaling Theory of Molten Polymers in Small Pores. *Macromolecules* **23**, 2276-2280 (1990).

20. Tree, D. R., Wang, Y. & Dorfman, K. D. Mobility of a Semiflexible Chain Confined in a Nanochannel. *Phys. Rev. Lett.* **108**, 228105 (2012).

21. Yang, Y., Burkhardt, T. W. & Gompper, G. Free energy and extension of a semiflexible polymer in cylindrical confining geometries. *Phys. Rev. E* **76**, 011804 (2007).

22. Persson, F., Utko, P., Reisner, W., Larsen, N. B. & Kristensen, A. Confinement spectroscopy: probing single DNA molecules with tapered nanochannels. *Nano Lett.* **9**, 1382-1385 (2009).

23. Utko, P., Persson, F., Kristensen, A. & Larsen, N. B. Injection molded nanofluidic chips: fabrication method and functional tests using single-molecule DNA experiments. *Lab Chip* **11**, 303-308 (2011).

24. Gupta, D. *et al.* Mixed confinement regimes during equilibrium confinement spectroscopy of DNA. *J. Chem. Phys.* **140**, 214901 (2014).

25. Gupta, D. *et al.* Experimental evidence of weak excluded volume effects for nanochannel confined DNA. *ACS Macro Lett.* **4**, 759-763 (2015).

26. Iarko, V. *et al.* Extension of nanoconfined DNA: Quantitative comparison between experiment and theory. *Phys. Rev. E* **92**, 062701 (2015).

27. Bhandari, A. B., Reifenberger, J. G., Chuang, H. M., Cao, H. & Dorfman, K. D. Measuring the wall depletion length of nanoconfined DNA. *J. Chem. Phys.* **149**, 104901 (2018).

28. Su, T., Das, S. K., Xiao, M. & Purohit, P. K. Transition between Two Regimes Describing Internal Fluctuation of DNA in a Nanochannel. *PLoS One* **6**, e16890 (2011).

29. Thamdrup, L. H., Klukowska, A. & Kristensen, A. Stretching DNA in polymer nanochannels fabricated by thermal imprint in PMMA. *Nanotechnology* **19**, 125301 (2008).

30. Manneschi, C. *et al.* Conformations of DNA in Triangular Nanochannels. *Macromolecules* **46**, 4198-4206 (2013).

31. Werner, E. & Mehlig, B. Scaling regimes of a semiflexible polymer in a rectangular channel. *Phys Rev E Stat Nonlin Soft Matter Phys* **91**, 050601 (2015).

32. Cheong, G. K., Li, X. & Dorfman, K. D. Wall depletion length of a channel-confined polymer. *Phys Rev E* **95**, 022501 (2017).

33. Cheong, G. K., Li, X. & Dorfman, K. D. Evidence for the extended de Gennes regime of a semiflexible polymer in slit confinement. *Phys Rev E* **97** (2018).

34. Menard, L. D. & Ramsey, J. M. The fabrication of sub-5-nm nanochannels in insulating substrates using focused ion beam milling. *Nano Lett.* **11**, 512-517 (2011).

35. Jacobson, S. C., Moore, A. W. & Ramsey, J. M. Fused Quartz Substrates for Microchip Electrophoresis. *Analytical Chemistry* **67**, 2059-2063 (1995).

36. Menard, L. D. & Ramsey, J. M. Electrokinetically-Driven Transport of DNA through Focused Ion Beam Milled Nanofluidic Channels. *Anal. Chem.* **85**, 1146-1153 (2013).

37. Tycon, M. A., Menard, L. D. & Ramsey, J. M. in *Proceedings of the 18th International Conference on Miniaturized Systems in Chemistry and Life Sciences.* 997-999 (Chemical and Biological Microsystems Society).

38. Zhou, J. *et al.* Enhanced nanochannel translocation and localization of genomic DNA molecules using three-dimensional nanofunnels. *Nat. Commun.* **8**, 807 (2017).

39. Kovacic, R. T., Comai, L. & Bendich, A. J. Protection of megabase DNA from shearing. *Nucleic Acids Res.* **23**, 3999-4000 (1995).

40. Zhang, C., Zhang, F., van Kan, J. A. & van der Maarel, J. R. Effects of electrostatic screening on the conformation of single DNA molecules confined in a nanochannel. *J. Chem. Phys.* **128**, 225109 (2008).

41. Menard, L. D. & Ramsey, J. M. in *MicroTAS.*

42. Stigter, D. Interactions of Highly Charged Colloidal Cylinders with Applications to Double-Stranded DNA. *Biopolymers* **16**, 1435-1448 (1977).

43. Werner, E. & Mehlig, B. Confined polymers in the extended de Gennes regime. *Phys. Rev. E* **90**, 062602 (2014).

44. Dobrynin, A. V. Effect of counterion condensation on rigidity of semiflexible polyelectrolytes. *Macromolecules* **39**, 9519-9527 (2006).

45. Gupta, D., Bhandari, A. B. & Dorfman, K. D. Evaluation of Blob Theory for the Diffusion of DNA in Nanochannels. *Macromolecules* **51**, 1748-1755 (2018).

CHAPTER 3: QUANTITATIVE METHOD FOR ANALYSIS OF DNA TRANSPORT

3.1 – Introduction

Nanofluidic phenomenon such as electrical double layer overlap,[1,2] high surface to volume ratios,[3] confinement effects on macromolecules,[4,5] entropic effects,[6,7] and manipulation of electroosmotic flows[8-10] have all been investigated in great detail over the past few decades. Of particular importance to long-read mapping applications is the large surface-to-volume ratio of nanochannels and the confinement effects on macromolecules like DNA. Transport of large macromolecules at the nanoscale is commonly accomplished by electrophoresis made possible by the negative charge of the DNA phosphate backbone. In charged electrophoretic environments nanochannel walls in both silicon and polymeric substrates gain a characteristic surface charge due to deprotonation.[11-13] Highly-confined DNA transport in nanochannels is influenced by charge based interactions between molecules and channel walls. Charged interactions can be beneficial as in the case of ion enrichment, ion depletion, and electroosmotic flow-based transport;[1,14,15] however, surface charge can also lead to detrimental surface-wall interactions like unwanted stick-slip motion or molecule adsorption.[3,16,17] Detrimental surface-wall interactions are collectively known as non-specific surface interactions and are currently not well understood. Non-specific surface interactions between DNA and nanochannel walls can have severe consequences for long-read mapping of genetic material that relies on confinement to remain ordered during transport.

Solid-state nanochannels used for long-read mapping applications do so by leveraging DNA confinement. DNA confinement in nanochannels restricts DNA movement and digested fragments remain ordered through the course of nanochannel transport.[4,18-20] However, if a subset of DNA fragments interact with the channel walls, it may lead to adjacent fragments interpenetrating or passing one another during transport. Any reordering of digested DNA fragments in the nanochannel are miscategorized as genomic structural variants upon assembly, limiting the utility of such systems as analytical tools. Much of the current analysis of DNA transport and non-specific surface interactions is qualitative in nature. Long-read mapping analysis is highly quantitative but only provides a single data

point at a single location in a nanochannel,[21-24] and thus does not provide sufficient information into how non-specific surface interactions affect DNA transport.

The motivation of this chapter is therefore the development of a quantitative method to track DNA transport at successive locations in a nanochannel. For this work, fluorescent dye intercalated DNA fragment sizes will be analyzed at 3 successive regions of interest (ROIs) in order to provide snapshots of transport through the nanochannel. Identified fragments at the first ROI will attempt to be located in the 2 downstream ROIs using time windowing and with use of appropriate size tolerances. Analysis of detrimental surface-wall interactions and DNA transport characteristics in various buffers will be investigated by determining the number of fragments delayed during transport. Fragments will be sorted as either correctly-called, incorrectly-called or missing. Correctly-called fragments would be fragments transported from ROI 1 to a successive ROI in the 'correct' transport time and are the same size fragment. Incorrectly-called would be fragments that arrived at the 'correct' transport time, but the traces came from different sized fragments (implications discussed below), and missing fragments would be fragments not found again after ROI 1. Establishing a baseline DNA transport efficiency (percentage of fragments that transport unaffected divided by total number of transported DNA fragments) in simple buffers will facilitate comparison to DNA transport in more complex digestion buffers. A brief outline of the analysis method is as follows:

1. Define 3 ROIs along the nanofluidic channel
2. Determine DNA appearance time and peak area from fluorescence signal
3. Normalize fragment sizes with multivariate Gaussian fits from peak areas
4. Establish fragment-size-specific size tolerances
5. Align transport data signals between ROIs with cross-correlation
6. Factor effects of diffusion on transport data
7. Assign compared DNA fragments: correctly-called, incorrectly-called, and missing fragments – based on transport time and fragment size.

Empirical DNA transport experiments were performed in this chapter to provide real data for method development. Further results from empirical DNA transport experiments will be discussed in the following chapter in detail.

3.2 – Experimental

Devices used in this chapter were obtained from Genturi Inc. Figure 3.1 illustrates the device design. Similar to the quartz devices described in Chapter 2, the devices used in chapter 3 and 4 consists of four microfluidic channels connected by a single serpentine nanochannel 315 nm wide and 210 nm deep. Injection molding and fusion bonding were used to make the Genturi devices out of cyclo olefin polymer (COP). Entrance and exit vias (V1-V4 source and sink) for buffer transport and subsequent electrode placement were incorporated into each microchannel. As shown in the inset (Figure 3.1B) the nanochannel design is serpentine with the arrows showing the direction of DNA transport. A well-placed laser-line can be used to inspect multiple regions of interest of the nanochannel. Each device was used for a period of one experiment before they were discarded at the end of the experiment.

3.2.1 – Device Priming Protocol

New out-of-the-box devices underwent a priming protocol prior to experiment. A buffer similar to Cutsmart (New England BioLabs) was used in all priming and experiment buffers. The similar solution was made in house and contained similar components to commercially-available Cutsmart (0.5 M potassium acetate, 0.2M tris-acetate, 1g/L BSA) only without Mg acetate. Regardless, the house-made solution will be referred to as Cutsmart. The following components were mixed in the following order to create a passivation solution:

1. 100 µL 10X Cutsmart (no Mg^{2+})
2. 100 µL 20% 10 kDa polyvinylpyrrolidone in water
3. 723 µL nuclease-free water
4. 50 µL 2% Tween-20 in nuclease-free water
5. 25 µL 4% BSA in nuclease-free water
6. 2 µL 1 M dithiothreitol

The resulting solution was mixed for 60 s at 3000 RPM and filtered through a 0.2-micron PES syringe filter (Fisher Scientific). The device was primed by adding 30 µL passivation solution into the source reservoir of V4, and pulling on the V4 sink reservoir for 1 min with house vacuum (-542 mBar). Next, the aforementioned loading and buffer transport step occurred for V4, V3, V2, and finally V1 in order. Microchannels were loaded in order for each experiment to ensure consistent nanochannel wetting. After

the initial addition of passivation solution to each reservoir, all eight (4 source, 4 sink) vias were balanced with additional passivation solution to inhibit additional head pressure induced flow. Lastly, each device was stored at 4 °C in a parafilm-sealed petri dish for 24 h before the experiment. After 24 h the passivation solution was aspirated out of each via before the additional of experimental buffers.

3.2.2 – Experimental Buffers

DNA was stained in an EDTA-based solution at a concentration of 66.6 ng/μL, 34 mM EDTA, and 10:1 bp:dye ratio of YOYO-1. A Cutsmart base solution was used as the experimental buffer and were mixed in the following order:

1. 200 μL 10X Cutsmart
2. 200 μL 20% 10 kDa PVP in water
3. 1300 μL nuclease-free water
4. 2 μL 1 mM DTT

The resulting solution was mixed for 60 s at 3000 RPM and then filtered with a 20 nm anodisc filter (Whatman – GE Healthcare Life Sciences) to remove any particulates that could clog the nanochannel. The exact experimental buffer constituents differed depending on if oligonucleotide dynamic coatings or Mg-acetate was added, the components and results of which will be discussed in the following chapter.

3.2.3 – HindIII ladder

λ DNA HindIII digest (New England Biolabs) was used as the DNA source for the transport experiments. The DNA ladder consists of six main fragment sizes:

- 2,027 bp
- 2,322 bp
- 4,361 bp
- 6,557 bp
- 9,416 bp
- 23,120 bp

λ DNA HindIII digest was chosen so that a distribution of fragment sizes could be isolated and analyzed for determination of potentially unique DNA transport characteristics.

3.2.4 – Optical Setup

An inverted fluorescence Nikon Eclipse Ti microscope was used in conjunction with a Photometrics Prime 95B sCMOS camera for data acquisition (Figure 3.2). A laser-line was used to facilitate data collection of DNA transport characteristics in locations where the laser intersected with the nanochannel and is illustrated in Figure 3.2. Three regions of interest (ROI 1, ROI 2, ROI 3) encompassing the areas where the laser line intersected with the serpentine nanochannel were created. Important to note, a single DNA fragment transporting from V1-V4 through the nanochannel will enter all three ROIs in order, enabling comparisons between fluorescence data collected between ROIs. A Coherent Obis 488 nm laser was used as the laser source for the experiments. The laser-line was created by inserting a cylindrical lens (Thor Labs: LJ1212L1-A) into the laser path. A Nikon Perfect Focus System was used to maintain optical focus in the nanochannel over the course of the experiment. Micromanager 2.0 was used as the data acquisition software. At the start of each experiment the field of view was binned to cover only the three ROIs to increase the frame rate capability of the camera. The camera was run at 10 ms acquisition times for approximately 2.3 min or 23,000 frames for each video. A subset of 16 frames and the resulting florescence data of DNA transporting through the laser line over 16 frames, or 160 ms, is presented in Figure 3.3.

3.2.5 – Experimental operation and data collection

Experimental buffers were loaded onto the device after passivation was complete. Each reservoir was loaded with vacuum-assisted buffer transport, which consisted of pulling on the sink reservoir of each via for 2 minutes. Afterwards, all vias were balanced with their respective experimental buffer solutions to inhibit head pressure induced flow. Platinum electrodes were inserted into the fluidic conduit of each microfluidic leg. A USB-6363 National Instruments Multifunction DAQ board and in-house Labview software program was used for voltage control to drive electrophoretic transport. Electrokinetic DNA injection was driven by tuning voltage potentials at each via. A combination of nodal analysis, modeling the fluidic system as resistors in series, and the circuit simulator program LTspice were used in unison to determine the magnitude of electric field in the main nanochannel, 50 V/cm. V2 and V3 nanoslits were used to elicit DNA injection into the nanochannel by increasing the electric field near the entrance funnel. DNA transport reached steady state approximately 3 minutes after the 50 V/cm electric field was

established. The z-axis focus was set on the Perfect Focus System to eliminate focus drift. Once established, DNA translocation continued unaltered until data collection was finished. At least 10 DNA translocation videos were taken for each experiment performed (~40 min). In many cases > 15,000 fragments passed through the nanochannel/laser line setup over a period of 3 – 4 hours. A subset of fragments, approximately 8,000 total fragments on average, were analyzed for each experimental day. DNA transport and DNA-wall interactions were visually observed in a subset of experiments and were quantitatively observed using the following data analysis method.

3.3 – Data Analysis

3.3.1 – Defining Regions of Interest

A custom MATLAB script was written to analyze the data. First, raw image stacks from each experiment were imported into MATLAB. The magnitude of the background was determined by the intensity (arbitrary units, a.u.) of a 10 x 10 pixel region in the top left corner of the first frame (Figure 3.4). This value was subtracted from all subsequent images in the image stack. To select the three regions of interest (ROI 1, ROI 2 and ROI 3) where DNA translocates through the laser line and generates a fluorescence signal, the average intensity over the entire image stack (approx. 23,000 frames) was calculated and shown in Figure 3.4. The brightest pixel in each ROI area was set as the center of the respective ROI. The ROI area was determined by drawing a 7-pixel wide by 13-pixel tall box centered around the brightest pixel. The average intensity of the pixels in the 7 x 13 ROI for each frame was taken as the fluorescence signal.

As shown in Figure 3.4, each ROI had slightly different average intensity values (ΔROI1 (%)), with ROI 1 having a lower intensity than ROI 2 or ROI 3. This phenomenon was observed for all image stacks and is due to the Gaussian shape of the incident laser beam, which is not uniform along its longitudinal axis. Non-uniform fluorescence data between successive ROIs complicates tracking of DNA in successive ROIs. Because of this, efforts were undertaken to normalize the fluorescence data at each ROI.

3.3.2 – Sizing DNA and Peak Appearance Time from Fluorescence Signal

DNA signal residence time and fluorescence intensity can be used to determine DNA fragment size. Previous work indicates that the area under a fluorescence peak vs. time plot directly correlates with DNA size.[25] Therefore, the first step to analyzing the fluorescence data was to size all of the DNA fragments at each ROI. The average fluorescence data from each image's ROIs were imported into Clampfit 9.2 software (Molecular Devices), where the area under each fluorescent peak was calculated. A minimum fluorescent signal threshold was used to filter out background noise and sheared DNA fragments smaller than 500 bp. The data from each ROI was sized and thresholds were set just below the 500 bp fragment distribution as illustrated in Figure 3.5. Separation of HindIII fragment size populations were visible, also illustrated in Figure 3.5, due to the general fluorescence intensity increase

of larger fragments in the ladder. The Clampfit software was used to calculate the area under each signal peak and register the appearance time (t_a) of the peak relative to the data acquisition start. This data is then plotted as a histogram of DNA sizes as shown in Figure 3.6 with peaks corresponding to each fragment population expected from the HindIII digest. The histogram shows 5 distinct peaks (2.2 kbp, 4.4 kbp, 6.6 kbp, 9.2 kbp, 23.1 kbp), with a 6th potential peak (546 bp) cut off at x=0. The largest peak (47 counts) is a combination of the 2.0 and 2.3 kbp fragments in the HindIII ladder. Since in the majority of the data the two peaks cannot be resolved, the peak is referred to as the '2.2 kbp' peak. The subplot of Figure 3.6 shows the linear relationship between the area found from the Clampfit software and expected bp size of the HindIII ladder, further confirming the correlation between the two. The 564 bp peak was the smallest discernable fragment identified in this analysis, however was cut off by design due to the placement of the sizing threshold. The 564 bp peak and 23,130 bp peaks were not analyzed to the same degree as the intermediary peaks because many of the ~564 bp population fell under the threshold and the shape of the 23,130 bp peak varied from experiment to experiment, inhibiting direct comparisons.

3.3.3 – Calibrating Fragment Sizes with Gaussian Fits

While commercially available HindIII digests are expected to be nominally monodisperse, DNA sizing experiments have shown HindIII to have a distribution of contour lengths.[5,26-29] Further illustrated by the width of the histogram peaks in Figure 3.6, HindIII ladder fragment populations were also found to have a distribution of contour lengths. DNA contour length distributions are well approximated by Gaussian functions and can be fit to a Gaussian curve to accurately determine the centroid.[25] For this analysis the centroid of each sizing peak distribution was assumed to be the actual bp size of that specific fragment population. The center of the sizing peak of each DNA fragment was found by utilizing a multipeak Gaussian function for each ROI and image stack. Preset multivariate Gaussian functions in MATLAB had difficulty fitting the data accurately, so multivariate Gaussian fits were plotted alongside the raw data and were used as an indicator to guide centroid identification. Figure 3.7 shows an example of the multivariate Gaussian peak fit analysis and how it was used as a guide to find the center of each peak distribution. The multivariate Gaussian peak assessment was done individually for each ROI and each image stack, as the DNA area data differed for each ROI.

The centroid of each Gaussian peak (I*t) was recorded and assigned the expected HindIII ladder size (2.2, 4.4, 6.6, 9.4 kbp). An example of the magnitude of normalization and a comparison of the raw data vs. normalized data are illustrated in Figure 3.8 and Figure 3.9, respectively. In Figure 3.9, the raw mean area for each ROI is substantially different (ROI 1: 46,139 a.u. vs. ROI 2: 134,183 a.u. vs. ROI 3: 137,580 a.u.) due to intensity differences in the laser-line (Table 3.1). The normalized mean area for each ROI is in closer agreement (ROI 1: 14,031 a.u. vs. ROI 2: 14,600 a.u. vs ROI 3: 14,578 a.u.) as it removes the effect of the laser-line intensity variance. The agreement of normalized mean area is shown by the overlapping traces for each ROI in Figure 3.9. Now that each ROI has been normalized to the expected HindIII digest bp size they can be directly compared.

3.3.4 – Fragment Size Tolerances

In order to compare fragment sizes between ROIs, fragment size specific tolerances should be established for peak assignment. As illustrated by the width of the Gaussian peaks in Figure 3.6, 3.7, and 3.9, each fragment size population is not monodisperse but rather has a distribution of sizes corresponding to the width of each Gaussian peak. Therefore, a method for determining an appropriate sizing tolerance was required. Similar to the area/bp normalization method, fragment size specific peaks were individually fit to multivariate Gaussian curves. Individual Gaussian peaks were isolated as illustrated in Figure 3.10. Two times the standard deviation from the mean of the Gaussian fit - approximately 95% of the respective distribution - was used to determine an appropriate percent-based size tolerance for each fragment population. The 2 kbp DNA fragments (Figure 3.10) were found to require the largest size tolerance, approximately 45%, to capture 95% of the molecules in the 2 kbp distribution. For example, if a fragment trace in ROI 1 was sized to be 2.12 kbp then a 2.4 kbp sizing at ROI 2 would meet the 45% sizing tolerance requirement, and would be labelled as a 2.2 kbp fragment. On the other hand, if a fragment trace in ROI 1 was sized to be 2.12 kbp and sized at 5.1 kbp at ROI 2 then the comparison of fragment traces would fail the sizing requirement. In this case it is likely that the two traces are not from the same fragment moving from ROI 1 to ROI 2, but rather two different fragments. Figure 3.10 shows the sizing tolerances found empirically from the Gaussian fits. More stringent tolerances were applied to larger fragments (4 kbp = 40%, 6 kbp = 36%, and 9 kbp = 30%) as 95% of their Gaussian distributions ($2*\sigma$ / centroid) were a smaller percentage of their average size.

3.3.5 – Aligning Data Signals Using Cross-Correlation

At this point DNA has been sized and normalized at each ROI, analyzing comparisons between ROIs, and furthermore DNA transport, is now possible. Yet, an additional unanalyzed metric obtained from the laser-line experiment is the appearance time (t_a) of each DNA fragment translocation through a ROI location. As a reminder, a DNA fragment transporting through the nanochannel encounters ROI 1, 2, and 3 in order. Once DNA passes the V2 slits both the channel dimensions and electric field are constant; therefore, the DNA velocity is expected to be constant during transport. This experimental factor, coupled with the established independence between DNA molecule length and velocity in nanochannels with dimensions greater than the contour length,[25] allows for use the of cross-correlation techniques to determine the average transit time (τ) between ROIs. Cross correlation is defined as:

$$(f * g)(\tau) \triangleq \int_{-\infty}^{\infty} \overline{f(t-\tau)} g(t) dt \tag{15}$$

or for discrete functions is equivalent to:

$$(f * g)[n] \triangleq \sum_{m=-\infty}^{\infty} \overline{f[m-n]} g[m] \tag{16}$$

where f and g are two signals with a shift along the x-axis. The signal data presented here is by nature discrete, nonetheless, the variable τ will be used to denote the transit time found by cross-correlation. Analyzing the cross-correlation function of a single DNA molecule provides time-averaged information about transport. In this analysis the MATLAB function *Alignsignals* was used to find τ.[30] The *Alignsignals* function determines the cross-correlation between the pair of signals at all possible time steps. The estimated delay is chosen by the normalized cross-correlation where the signals are best aligned. Figure 3.11 shows the signal vs. time trace of ROI 1 and ROI 2. The time trace of ROI 2 can be shifted by τ found by cross-correlation, allowing for direct comparison of DNA signal traces in two locations. The cross-correlated data, ROI 2 time-shifted to align with ROI 1, will henceforth be referred to as aligned data. There are three ROIs that can be investigated by cross-correlation. For most analyses here, ROI 1 – the first location transporting DNA would experience – was compared to ROI 2.

3.3.6 – Establishment of Appropriate Time Window for Aligned Data

DNA fragments axially diffuse as they travel through the nanochannel.[31] The axial diffusion coefficient, D_t, is estimated as:

$$D_t \cong D_R \left(\frac{D^2}{w l_p}\right)^{\frac{1}{3}} \quad (17)$$

where w is the effective width of a DNA molecule, l_p is the persistence length, D is the channel diameter, and D_R is the Rouse diffusivity of a freely draining chain. The Rouse diffusivity is dependent on both solvent viscosity and contour length, η and L_c, respectively:

$$D_R = \frac{k_B T}{6\pi\eta L_c} \quad (18)$$

where $k_B T$ is the measure of free energy of the molecule.

According to the equation above, axial diffusion is dependent on a DNA fragment's length. A time tolerance, henceforth discussed as a 'time window' to avoid confusion with the sizing area tolerance, is therefore necessary if tracking transport of DNA at two ROIs. Figure 3.12 illustrates how DNA diffusion can affect comparison of fragments between two locations after applying the transit time shift found from cross-correlation. DNA diffusion is illustrated by horizontal distance between fragments in the Figure. In theory, without diffusion or non-specific surface interactions, traces at ROI 1 and ROI 2 would perfectly align after applying the transit time shift. However, the effects of diffusion are found in empirically gathered data, illustrated by the time differences between adjacent fragments in Figure 3.12. Therefore, the final necessary metric needed for comparing DNA fragments at two separate locations is a time window accounting for molecule diffusion where the majority of fragments at ROI 1 are found at ROI 2. Preliminary experiments found that the vast majority of fragments translocated from ROI 1 to ROI 2 within ± 80 ms (8 frames) of the cross-correlation transit time, providing a good starting condition for this analysis. A number of time window sizes ranging from 80 – 140 ms were tested, and 140 ms was chosen as a conservative time window for subsequent analysis. Changing the time window size from 80 – 140 ms had negligible effect on the conclusions described in Chapter 4.

3.3.7 – DNA fragment assignment: Correctly Called, Incorrectly Called, and Missing fragments

With an appropriate time window and fragment-specific size tolerances well defined, the normalized and aligned data from a comparison of two ROIs were analyzed and assigned to three specific categories: correctly-called, incorrectly-called, and missing fragments.

A custom MATLAB script analyzed the normalized / aligned data by comparing the time and size of identified fragments in ROI 1 to identified fragments in ROI 2 with time window and size tolerances. First, the script searched for identified fragments with 0 ms time difference (reminder: ROI 1 (t), ROI 2 (t-τ)) and assigned fragments based on if they were within or out of size tolerance. Next, the script searched for identified fragments in ROI 1 to ROI 2 with a 10 ms time tolerance and assigned accordingly. Fragments that were found within the time window and were within the specified size tolerance were labelled 'correctly-called' fragments. The arrows in Figure 3.12a point to an example of correctly-called 2 kbp fragments. In this example the fragments are separated by 100 ms, within the 140 ms time window, and are within the size tolerance for the 2 kbp fragments. Important to notice here are the other fragments in the 12a frame. All other fragments are much closer than 100 ms – shown by their overlapping traces for both ROI 1 and ROI 2 – and are also correctly-called fragments. This shows the varied degrees of diffusion in the nanochannel and highlights the need for a time window.

Conversely, fragments that were found within the time window and were NOT within the size tolerance were labelled 'incorrectly-called' fragments. Correctly-called fragments were removed from successive time window iterations as they had been matched and thus their inclusion in larger time differences would create false 'incorrectly-called' assignments. Incorrectly-called fragments were kept in the total fragment pool for additional analysis in larger time window iterations. Figure 3.12b illustrates an example of incorrectly-called fragments. Both ROI 1 and ROI 2 trace is within the time tolerance, but they are outside of the size tolerance. Incorrectly-called fragments would often correctly match with other fragments in larger time differences (did not size match with fragment at 0 ms, however did size match with a different fragment at 20 ms). When this occurred the incorrectly-called fragment would be reassigned to a correctly-called fragment and sequentially removed from the incorrectly-called list / count. It is important to note that in 12B there are no other fragments of correct size in the time window. This

protocol continued until the end of the specific time window, from 0 - 140 ms in 10 ms increments, had been reached.

All resulting fragments in ROI 1 that had not been assigned, moreover were not found within 140 ms of any other fragments in ROI 2, were labelled ‘missing’ fragments. Figure 3.12c illustrates a missing fragment. A fragment exists in ROI 1 but does not at ROI 2, therefore the fragment transport has been interrupted and is ‘missing’. Ratios of the correctly-called, incorrectly-called, and missing fragments were compared from experiment to experiment and serve as metrics of utility from this data analysis method.

To reiterate, the first listed modality, correctly-called fragments, are fragments that successfully translocated without detrimental wall interactions (without adherence, adsorption, or a large degree of stick-slip motion). These fragments were identified in ROI 1 and successively identified at ROI 2 in both the defined time window and size tolerance. The simplified flowchart in Figure 3.13 shows molecule assignment for correctly-called, incorrectly-called, and missing fragments as color-coded examples. In this system, correctly called fragments are the most common modality seen in well-functioning experiments without sticking or detrimental wall interactions.

The second modality, incorrectly-called fragments, occur when a fragment is identified in ROI 1 and a different sized fragment is identified within the time window at ROI 2. Moreover, incorrectly called fragments fall outside of the specific size tolerance, AND the correctly sized (within size tolerance) fragment was NOT found within the specific time window. This specific modality is perhaps the most difficult to understand. There are two possible reasons that a fragment could result in being assigned incorrectly called: there is a degree of slick-slip motion or reversible DNA adherence to the channel wall during DNA transport that results in the correct fragment being delayed and an earlier fragment appearing instead in the time window, or the fragment that appears in the time window is actually the same fragment and sized incorrectly at the second ROI. Additional information can be gained by examining the ratio of the total matched fragment sizes at ROI 2 to ROI 1.

$$Average\ Size\ Difference = \frac{\sum ROI\ 2_{fragments}}{\sum ROI\ 1_{fragments}} \tag{19}$$

While correctly-called fragments have an average size difference of approximately 17%, incorrectly-called fragments have an average size difference of 97%. Moreover, the average incorrectly-called fragment

size is substantially different from what was expected in ROI 1. The metric incorrectly-called fragment percentage is susceptible to a certain degree of random error due to Brownian motion of DNA fragments during transport. For example, two fragments touching each other during transport through the first ROI may diffuse away from each other by the time they pass through the second ROI. Transport through the first ROI would result in one large DNA trace since the two closely-touching strands are indistinguishable at that point. The total incidence rate of this type of random error was investigated by comparing the total number of fragment signals at each ROI. This analysis found very good agreement between the number of fragments in each ROI, with an approximately 3% difference on average in the total number of fragment signals, which discounts Brownian motion (close DNA fragments counted as a single fragment in successive ROIs) as the leading cause of incorrectly-called fragments in the system.

The third modality, missing fragments, occur when a fragment is identified at ROI 1 and nothing is identified in ROI 2 within the specified time window. There are three potential explainations that would cause this modality. In the first scenario, a subset of DNA molecules experience DNA-wall interactions during transport leading to stick-slip motion or other friction-like force that would slow transport to the point where arrival of the fragment would fall outside of the time window. In the second scenario, a subset of DNA fragments permanently adhere to the COP channel wall. Lastly, in the third scenario the laser line causes significant photocleavage of transporting DNA fragments, leading to additional fragmentation in successive ROIs. The last two explanations were discounted by a number of controls discussed in detail in the following chapter. Missing fragments pose the greatest risk to mapping applications, therefore minimizing the total number of missing fragments, either through experimental design or buffer component, is of high importance.

3.3.8 – Metrics to Facilitate Experimental Comparison

The ratios of correctly-called, incorrectly-called, and missing fragments were used as metrics to facilitate experimental comparison. The following ratios were used as metrics; where M is the number of missing fragments, IC is the number of incorrectly-called fragments, and CC is the number of correctly-called fragments.

$$Missing\ Fragments\ (\%) = \frac{M}{CC+IC+M} \tag{20}$$

$$Incorrectly\ Called\ Fragments\ (\%) = \frac{IC}{CC+IC+M} \quad (21)$$

The occurrence of both incorrectly-called and missing-fragments signify potential issues with DNA transport. To capture imperfect transport, incorrectly-called and missing fragments were collectively labelled as 'impacted transport' fragments.

$$Fragments\ with\ Impacted\ Transport\ (\%) = \frac{IC+M}{CC+IC+M} \quad (22)$$

These three metrics will be used to compare the effect of different buffers on the transport of DNA through nanochannels.

3.4 – Conclusion

Development of a quantitative method for DNA transport analysis has been presented. Fluorescence from YOYO-1 labelled HindIII digest fragments were analyzed at three regions of interest where a laser-line intersected a serpentine nanochannel. Fragment transport from successive ROIs was compared by use of cross-correlation, DNA fragment sizing, calibration of ROI fluorescence intensity at each ROI with multivariate Gaussian fits, inclusion of size and window tolerances, and finally fragment assignment based on size and transport time. The fragment assignment modalities, correctly-called, incorrectly-called, and missing fragments are used to classify fragment transport between the successive ROIs. Incorrectly-called and missing fragments are both classified as impacted transport fragments, signifying potential stick-slip motion or detrimental DNA-wall interactions influenced transport of the molecule. Assigned molecules and their respective ratios will be used to facilitate experimental comparison between buffer components, DNA fragment size, and the use of dynamic coatings.

3.5 – Figures

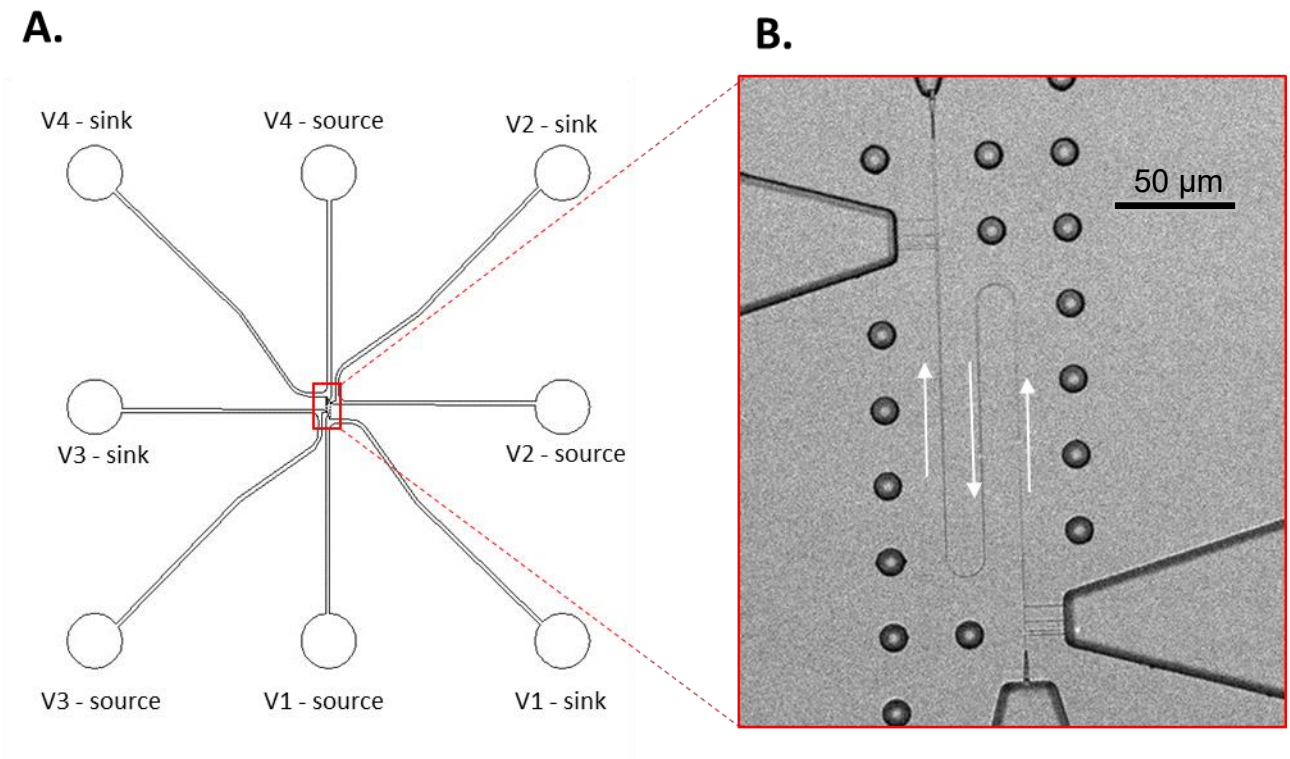

Figure 3.1: **A** The nanofluidic device design of Genturi Chips. A single nanofluidic conduit is connected by four sets of entrance/exit microchannels. V1-V4 nomenclature was used to identify the four entrance and exit vias. **B** is a closer view of the nanofluidic features. DNA transport occurred in the direction of the white arrows. Microfluidic funnels on the right and left – coupled with the attached nanoslits – were used to aid in electrokinetic injection of DNA fragments into the nanochannel.

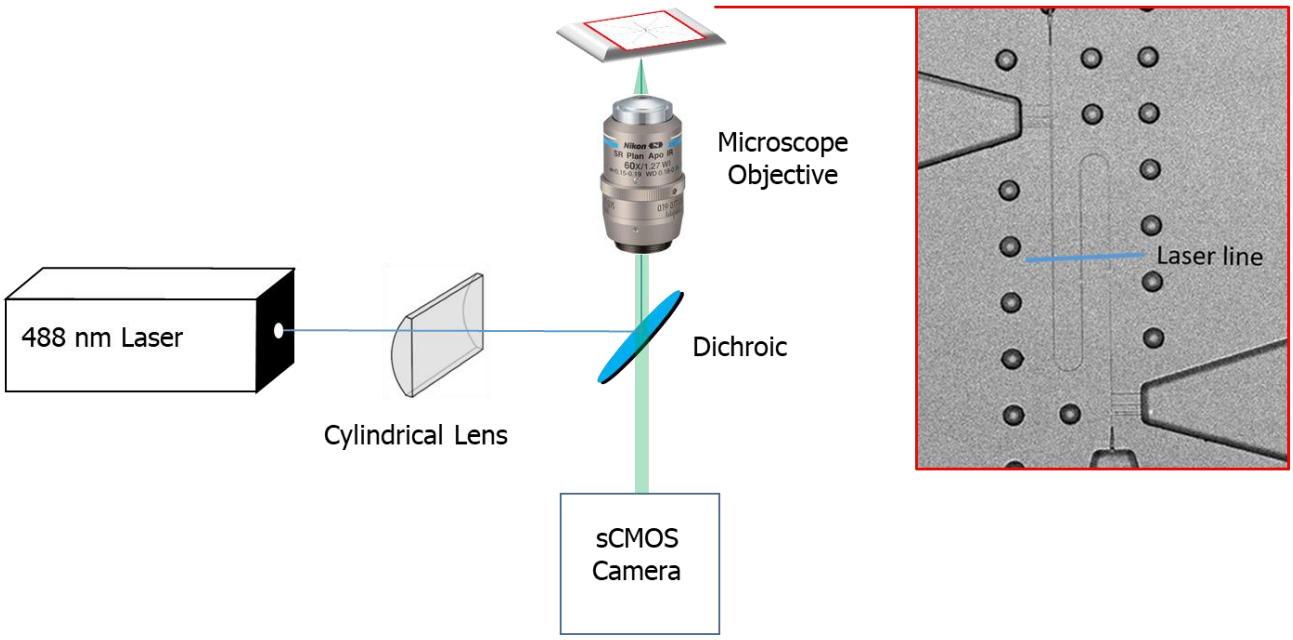

Figure 3.2: Simplified overview of the microscope setup. Placing a cylindrical lens in the 488 nm laser line path created a laser line for enabling inspection of DNA transport at multiple locations. The laser crossed the nanochannel path a total of three times, creating three regions of interest where DNA fluorescence was analyzed.

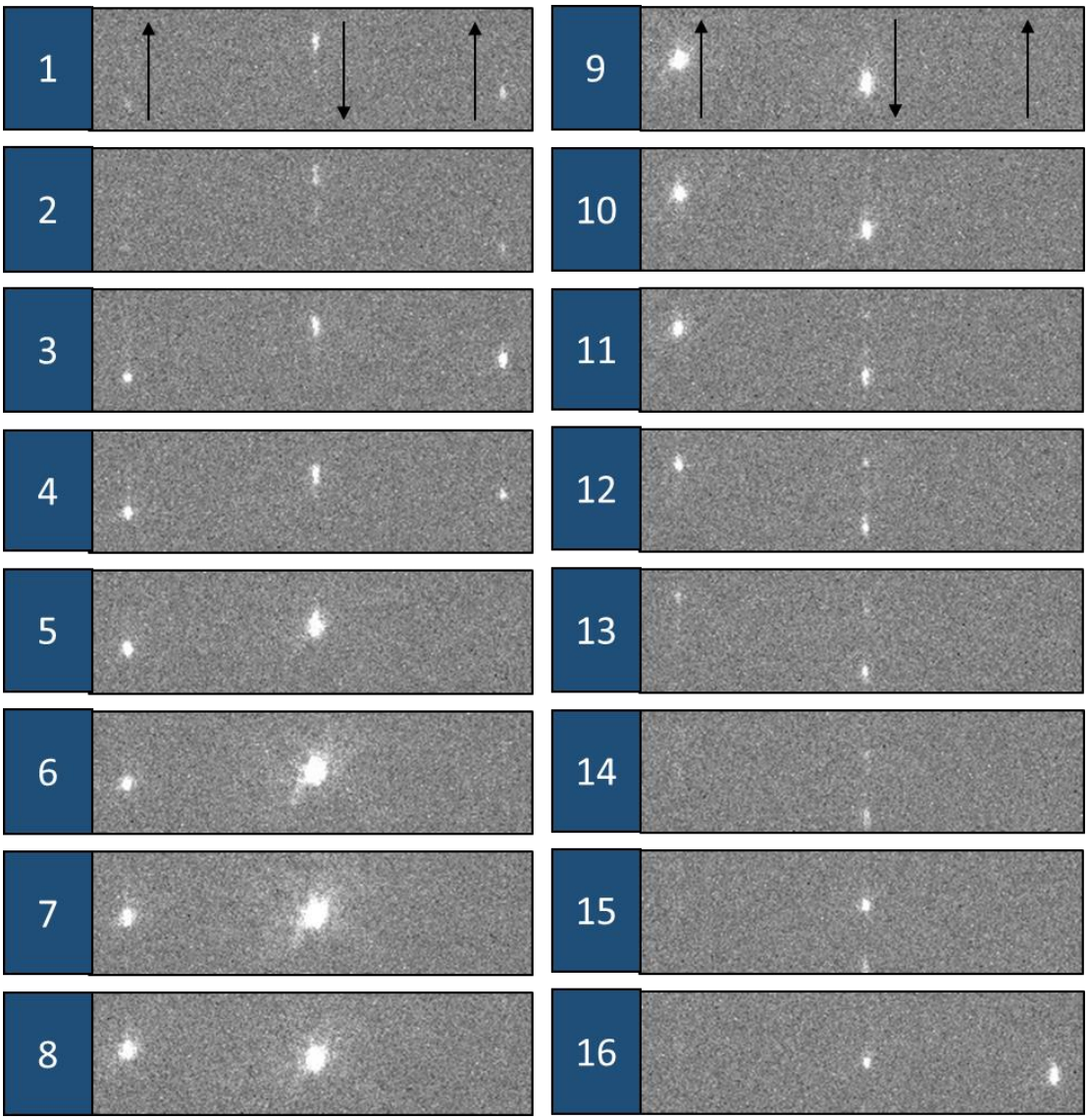

Figure 3.3: Transport of YOYO-1 labelled HindIII digest DNA fragments through the laser line. Each slide corresponds to an individual frame, 10 ms apart, with multiple DNA fragments transporting through the nanochannel simultaneously. The black arrows indicate DNA direction of travel in the nanochannel.

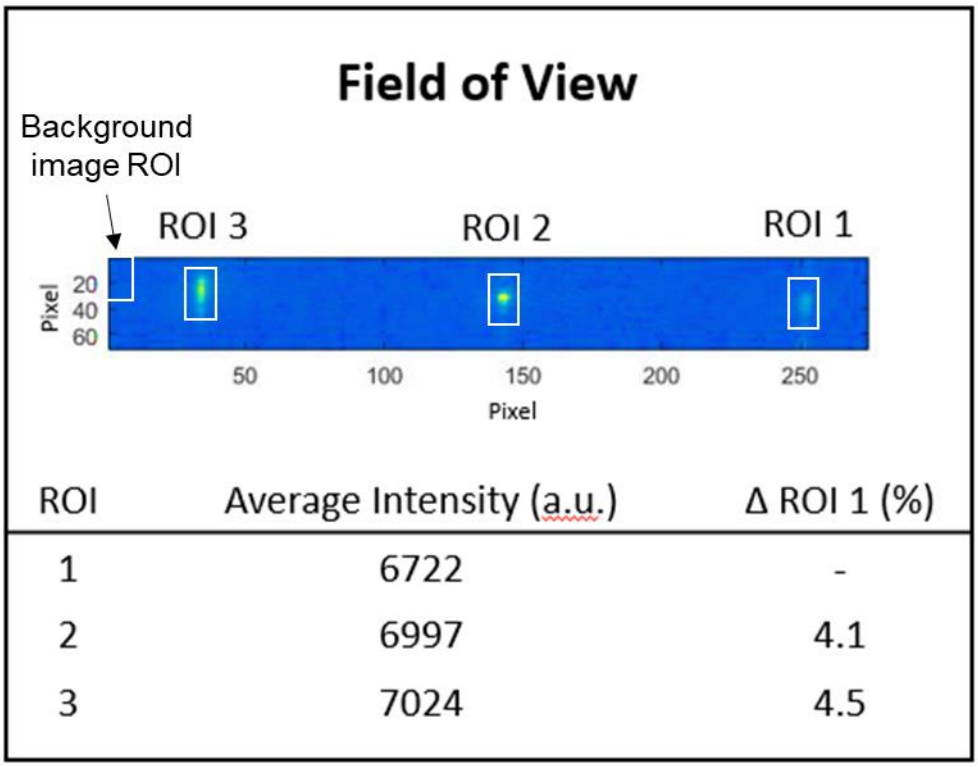

ROI	Average Intensity (a.u.)	Δ ROI 1 (%)
1	6722	-
2	6997	4.1
3	7024	4.5

Figure 3.4: YOYO-1 labelled DNA fragments fluoresce as they translocate through the laser line. Three ROIs are created by intersections of the nanochannel and laser line, where a 13x7 pixel box is drawn surrounding the brightest pixel. The average intensity of the ROI is recorded and used for further analysis. The intensity of the laser line is not uniform, pointing to the need for intensity normalization.

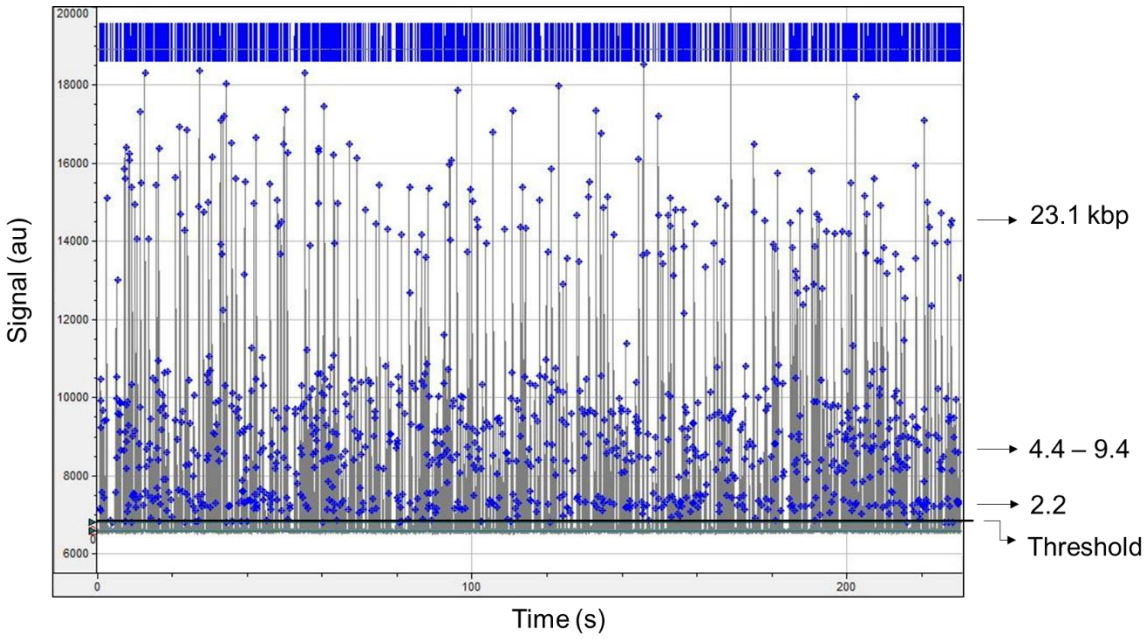

Figure 3.5: Screenshot of the DNA fragment distributions in the Clampfit software. The distribution of fragments, namely the separation between the 2.2 kbp, 4.4 – 9.4 kbp, and 23.1 kbp fragments, can be visually identified. The black line near the bottom of the figure is where the threshold was set at the 500 bp fragment size.

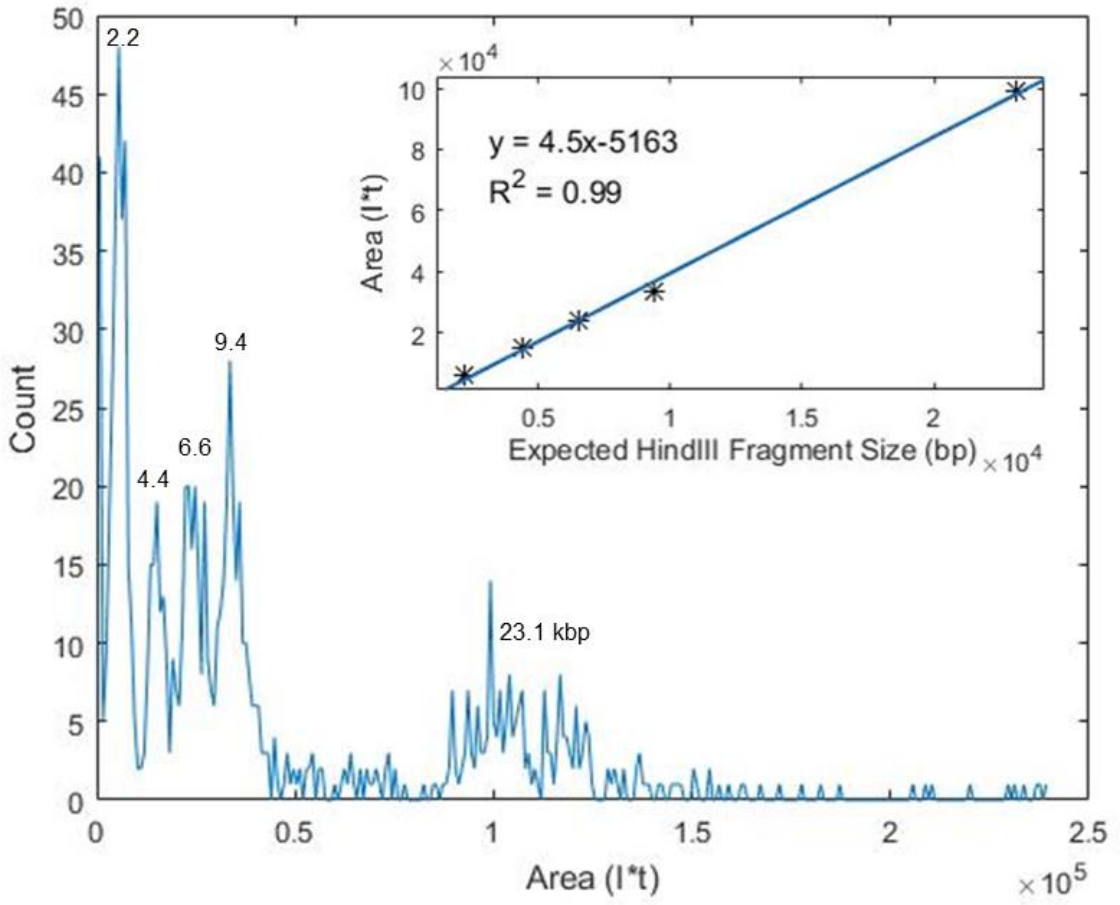

Figure 3.6: DNA sizing proof of principle. The number of fragments (Count) vs. Area (I*t) shows distinct peaks that correlate with expected HindIII fragment size.

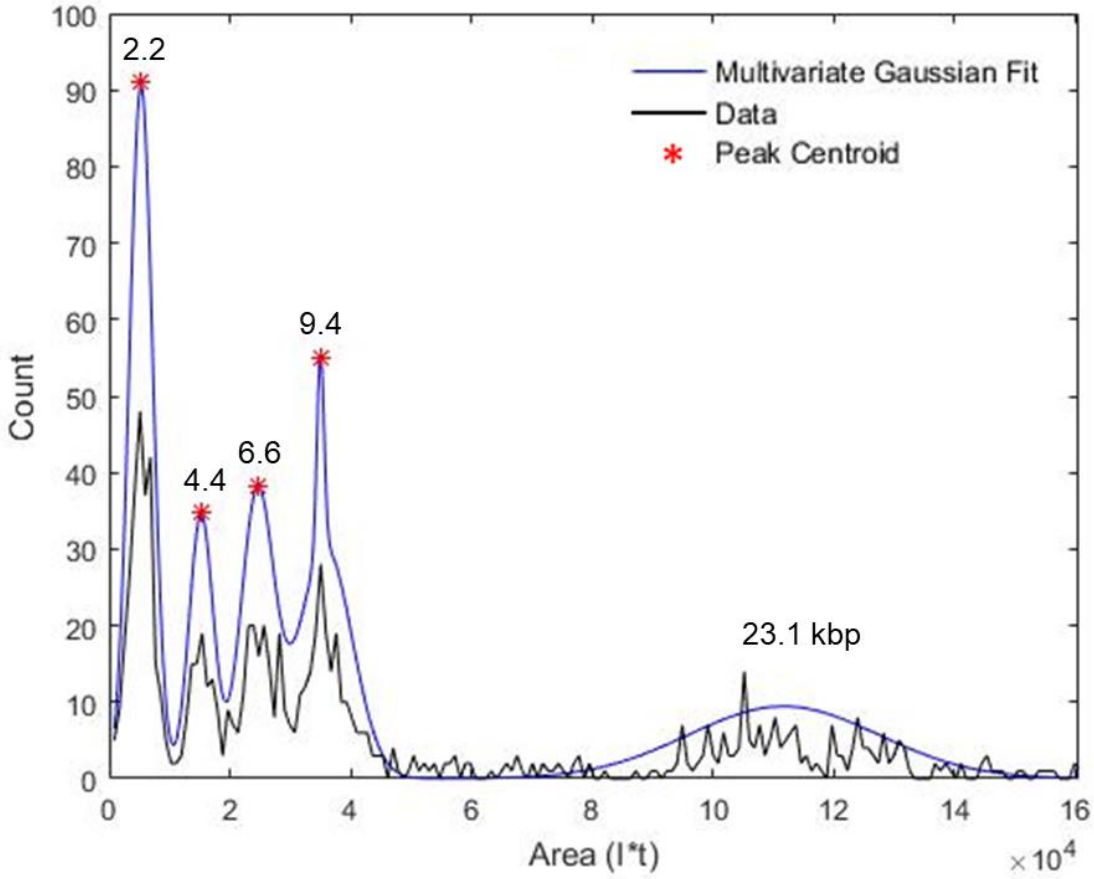

Figure 3.7: Example of the multivariate Gaussian fit on raw data pre area normalization. The multivariate Gaussian fit found 5 peaks corresponding to the 2.2, 4.4, 6.6, 9.2, and 23 kbp fragments in the HindIII ladder. The peak centroids of the 2.2-9.2 kbp fragments were used to calibrate intensity measurements at each ROI.

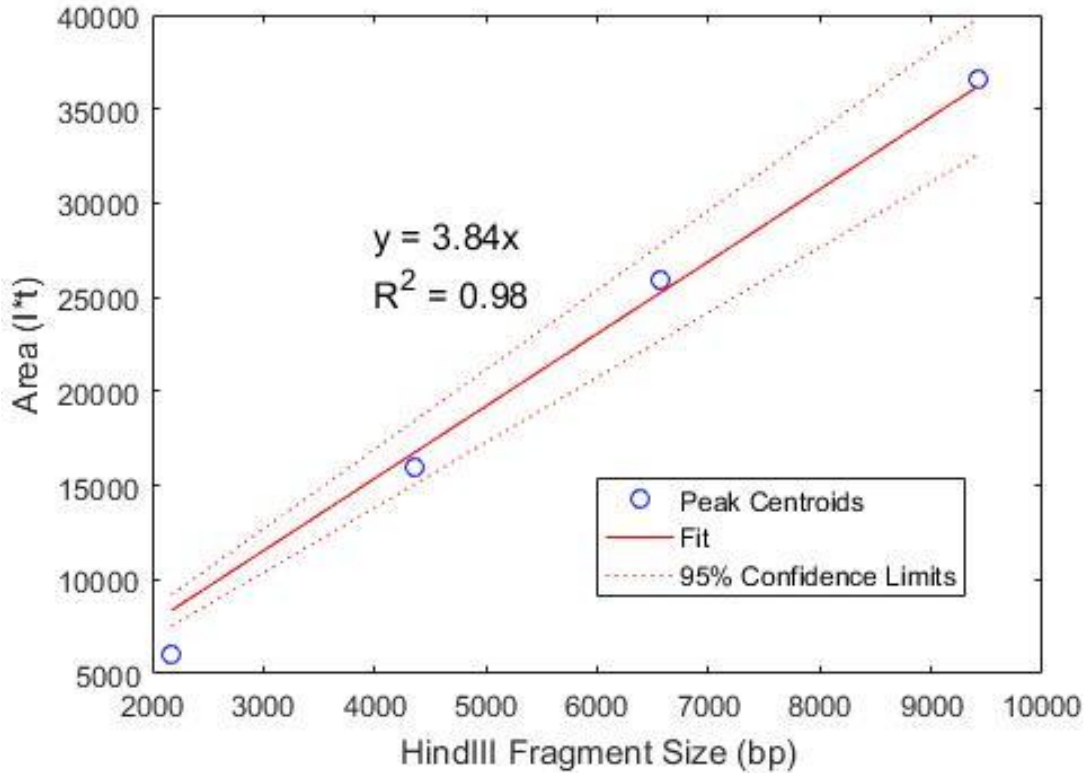

Figure 3.8: HindIII fragment size vs. peak area found from DNA sizing. Y-intercept = 0 was chosen as a constraint to the fits. Peak areas were calibrated according to the unique slope of each ROI.

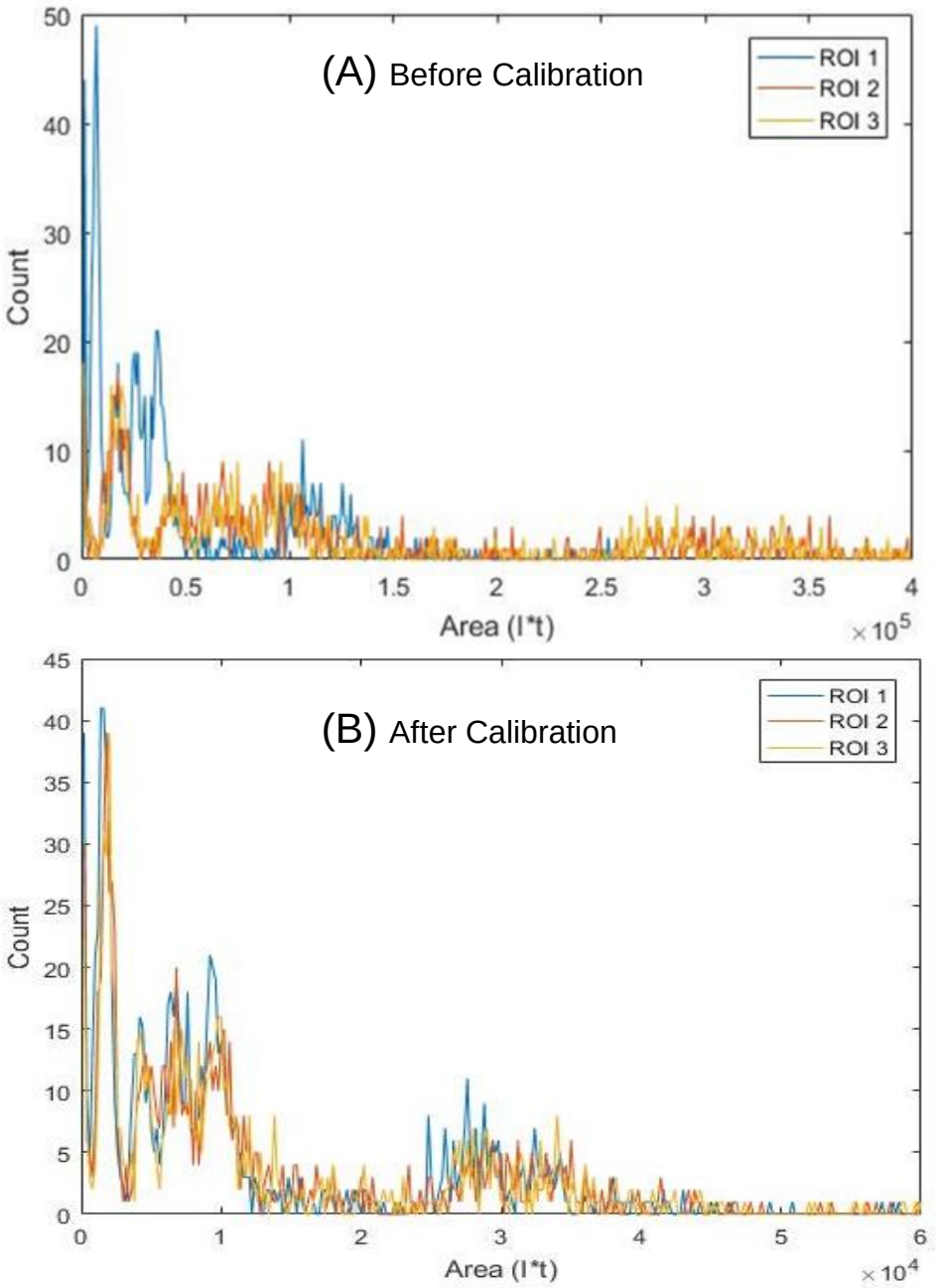

Figure 3.9: Sized DNA fragment data before (A) and after (B) calibration to expected HindIII fragment sizes. The shape of the traces of ROI 1, 2, and 3 are more highly uniform after calibration, shown by the overlapping traces in (B).

Raw vs. Normalized Data		
ROI	Raw Data Mean Area (a.u.)	Calibrated Data Mean Area (a.u.)
1	46,139	14,031
2	134,183	14,600
3	137,580	14,578

Table 3.1: Raw vs. Normalized representation of Figure 9 data.

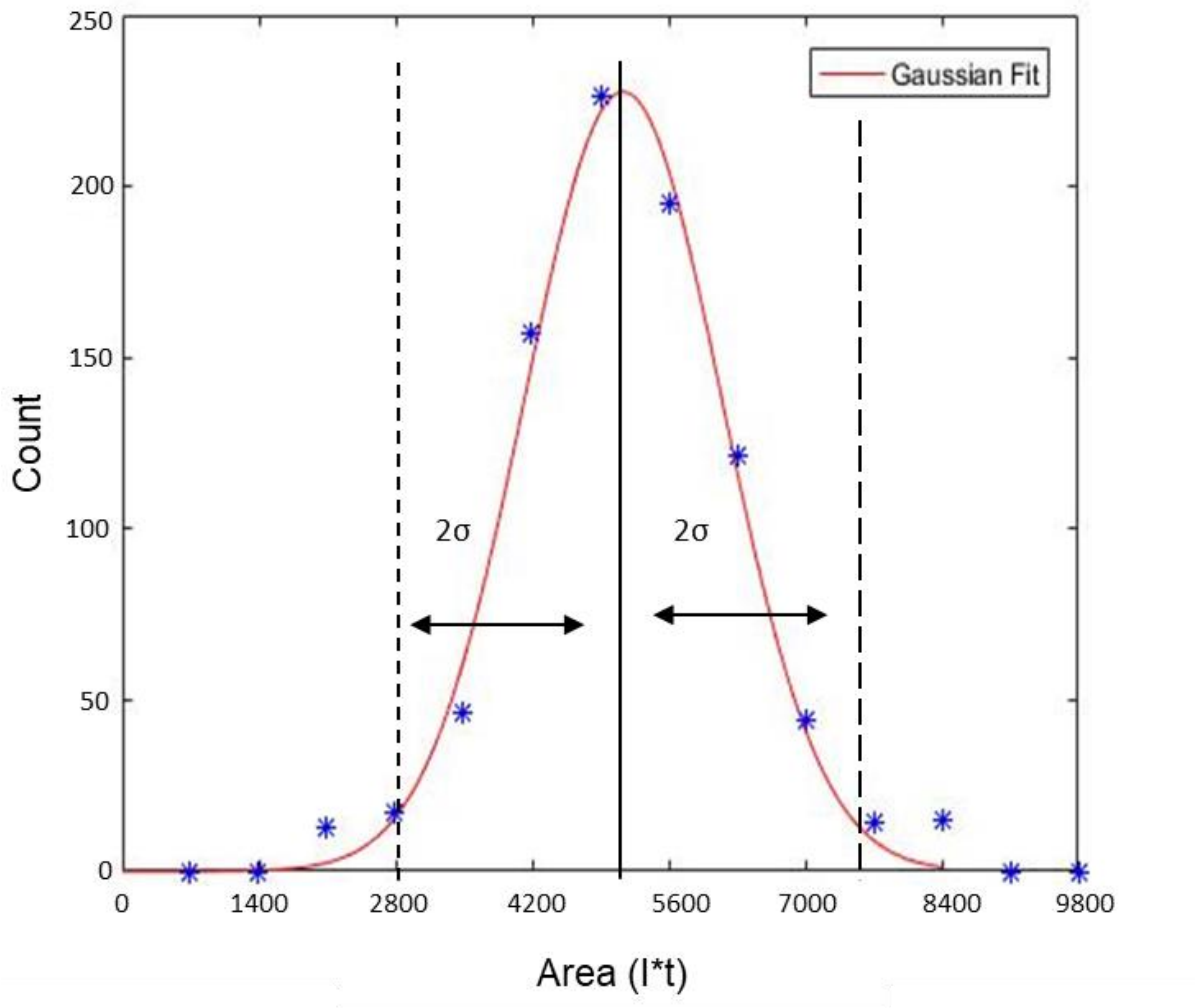

Fragment Size Tolerances	
Fragment Size (kbp)	Tolerance (2*STD/Average Area)
2.2	45%
4.4	40%
6.6	36%
9.4	30%

Figure 3.10: Fragment size specific sizing tolerances. A Gaussian fit was applied to determine the centroid / average area of each fragment size. Tolerances were set at approximately 2 X standard deviation so 95% of the molecules in the distribution would be captured in the tolerance. Each fragment size was investigated with a unique tolerance according to the table above – found by taking 2*STD / average area.

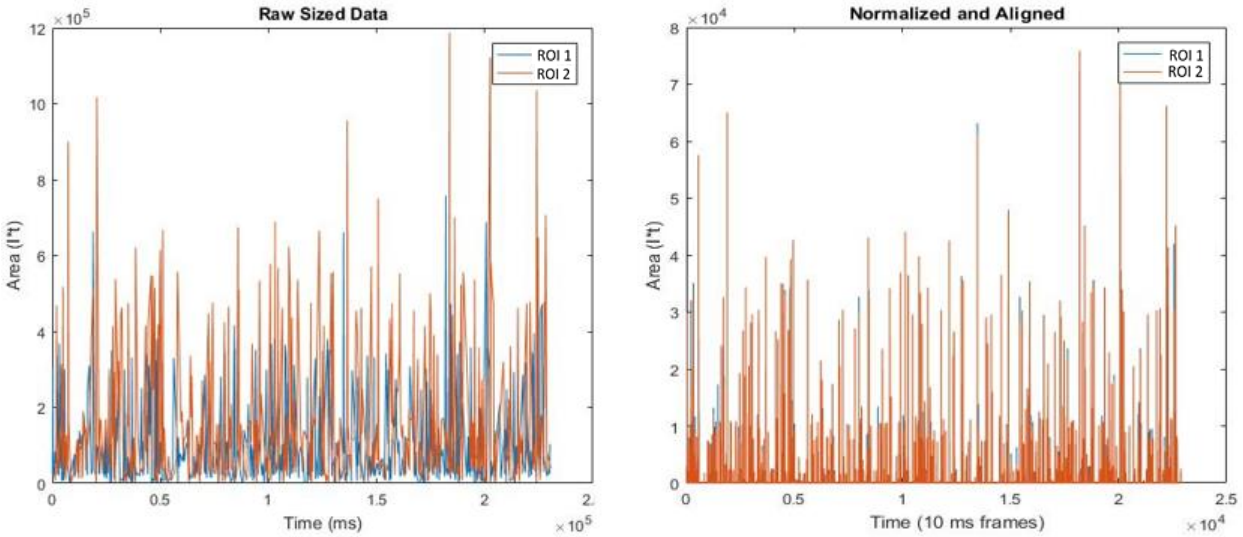

Figure 3.11: Comparison of raw data to Normalized and Aligned data. The time lag for this data set was 2.43 s, found by cross-correlation. The Normalized and Aligned data from ROI 2 and 3 is close to perfectly overlapped, setting the stage for molecule assignment.

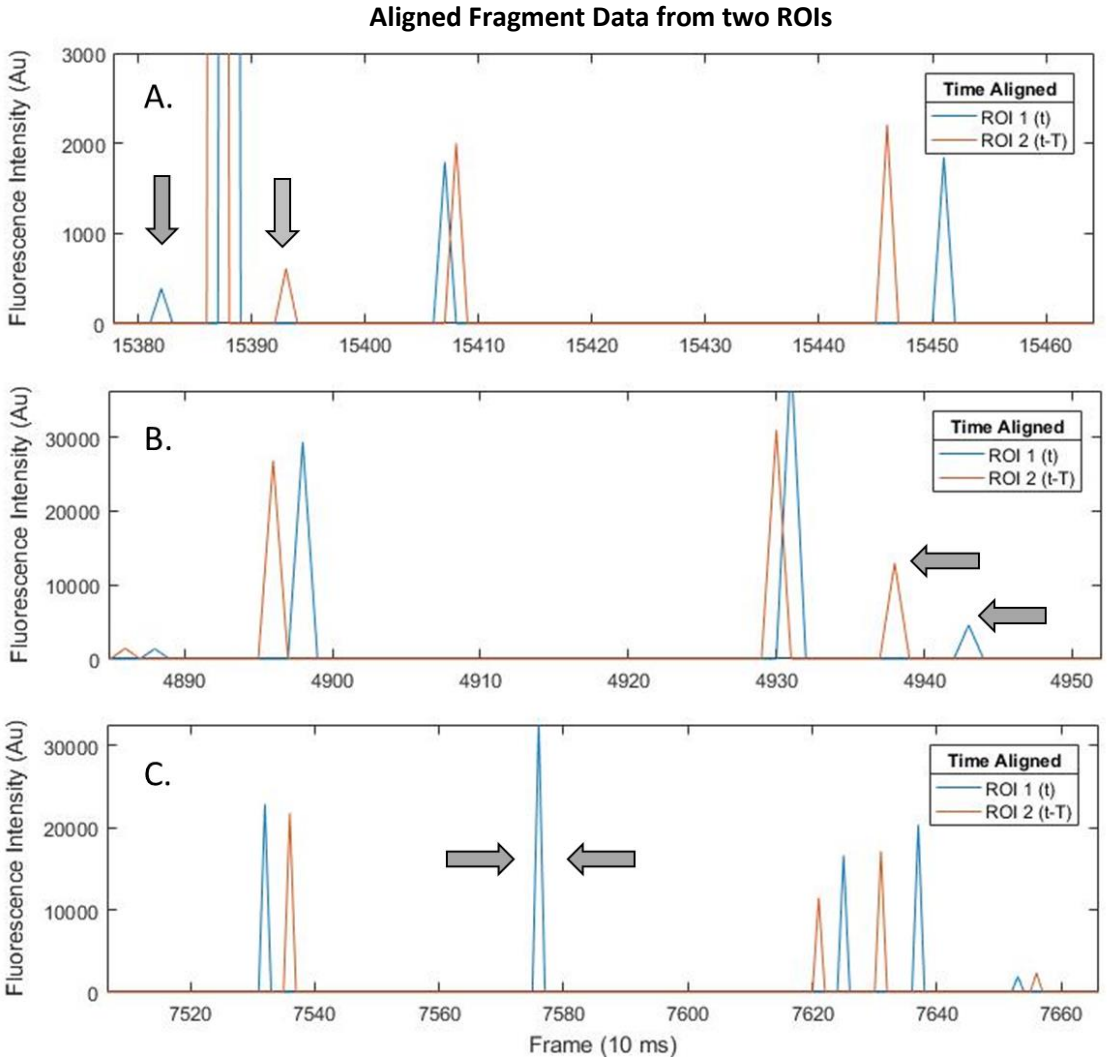

Figure 3.12: Example of molecule assignment modalities. **(A.)** The arrows point to two similarly sized fragments spread by approximately 100 ms, an example of diffusion in the system. However, this would be assigned 'correctly-called' as it is within the specified time window and size tolerance along with the rest of the paired traces in the subplot. **(B.)** The arrows point to two dissimilarly sized fragments. This would be assigned 'incorrectly-called' as they are not within the specified 30-45% size tolerance. **(C.)** The arrows point to a lone fragment in ROI 1 that does not have a coupled fragment in ROI 2. This would be assigned as a 'missing' fragment as the fragment's transport was strongly impacted between ROI 1 and 2.

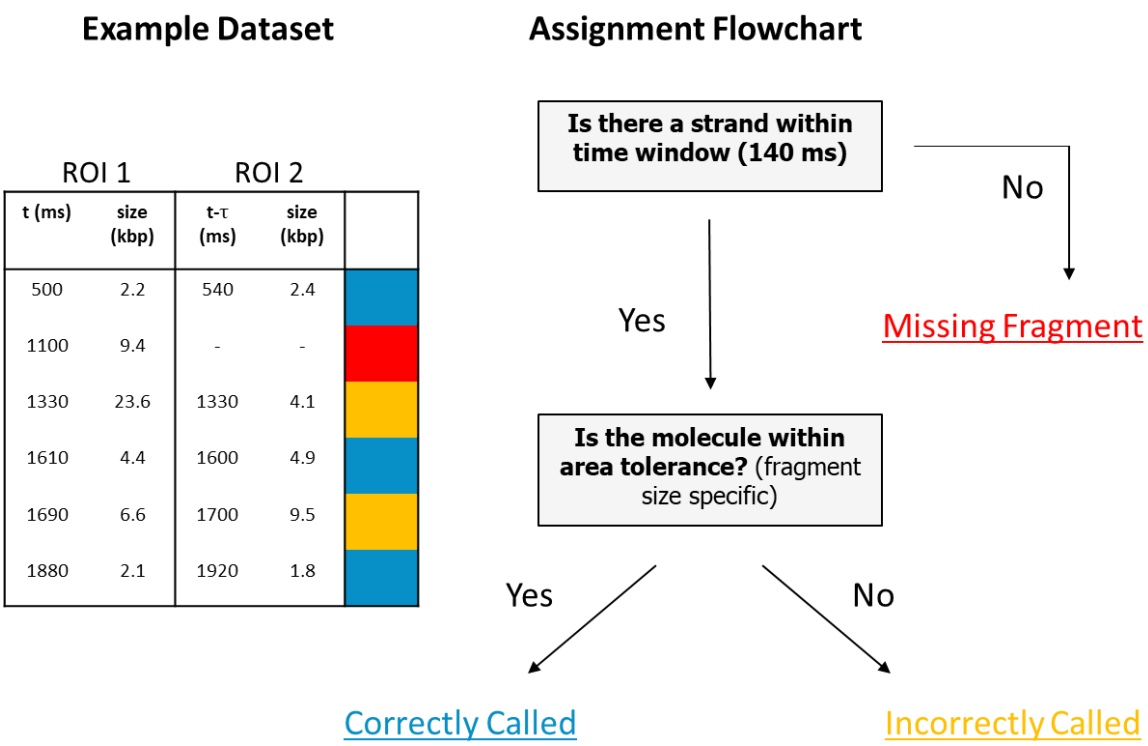

Figure 3.13: Flowchart of molecule assignment. The color code presented here is unique to this figure. Incorrectly-called and missing fragments will be classified as fragments with 'impacted transport' in Chapter 4. Missing fragments are highly detrimental to long-read optical mapping applications.

REFERENCES

1. Pu, Q. S., Yun, J. S., Temkin, H. & Liu, S. R. Ion-enrichment and ion-depletion effect of nanochannel structures. *Nano Lett* **4**, 1099-1103 (2004).

2. Baldessari, F. & Santiago, J. G. Electrophoresis in nanochannels: brief review and speculation. *Journal of Nanobiotechnology* **4**, 12/11-16 (2006).

3. Tegenfeldt, J. O. *et al.* Micro- and nanofluidics for DNA analysis. *Analytical & Bioanalytical Chemistry* **378**, 1678-1692 (2004).

4. Reisner, W., Pedersen, J. N. & Austin, R. H. DNA confinement in nanochannels: physics and biological applications. *Rep. Prog. Phys.* **75**, 106601 (2012).

5. Persson, F., Utko, P., Reisner, W., Larsen, N. B. & Kristensen, A. Confinement spectroscopy: probing single DNA molecules with tapered nanochannels. *Nano Lett.* **9**, 1382-1385 (2009).

6. Mannion, J. T., Reccius, C. H., Cross, J. D. & Craighead, H. G. Conformational analysis of single DNA molecules undergoing entropically induced motion in nanochannels. *Biophys. J.* **90**, 4538-4545 (2006).

7. Zhou, J. *et al.* Enhanced nanochannel translocation and localization of genomic DNA molecules using three-dimensional nanofunnels. *Nat. Commun.* **8**, 807 (2017).

8. Qiao, R. & Aluru, N. R. Ion concentrations and velocity profiles in nanochannel electroosmotic flows. *The Journal of Chemical Physics* **118**, 4692-4701 (2003).

9. VanOrman, B. B., Liversidge, G. G., McIntire, G. L., Olefirowicz, T. M. & Ewing, A. G. Effects of buffer composition on electroosmotic flow in capillary electrophoresis. *J. Microcol. Sep.* **2**, 176-180 (1990).

10. Yeung, K. K.-C. & Lucy, C. A. Suppresion of Electroosmotic Flow and Prevention of Wall Adsorption in Capillary Zone Electrophoresis Using Zwitterionic Surfactants. *Analytical Chemistry* **69**, 3435-3441 (1997).

11. Stein, D., Kruithof, M. & Dekker, C. Surface-charge-governed ion transport in nanofluidic channels. *Physical Review Letters* **93** (2004).

12. Karnik, R., Castelino, K., Fan, R., Yang, P. & Majumdar, A. Effects of biological reactions and modifications on conductance of nanofluidic channels. *Nano Lett* **5**, 1638-1642 (2005).

13. Martins, D. C., Chu, V. & Conde, J. P. The effect of the surface functionalization and the electrolyte concentration on the electrical conductance of silica nanochannels. *Biomicrofluidics* **7**, 34111 (2013).

14. Schoch, R. B., Han, J. & Renaud, P. Transport phenomena in nanofluidics. *Rev. Mod. Phys.* **80**, 839-883 (2008).

15. Bocquet, L. & Charlaix, E. Nanofluidics, from bulk to interfaces. *Chem Soc Rev* **39**, 1073-1095 (2010).

16. Rodriguez, I. & Li, S. F. Y. Surface deactivation in protein and peptide analysis by capillary electrophoresis. *Anal Chim Acta* **383**, 1-26 (1999).

17. Persson, F. *et al.* Lipid-based passivation in nanofluidics. *Nano Lett.* **12**, 2260-2265 (2012).

18. Riehn, R. *et al.* Restriction mapping in nanofluidic devices. *Proc Natl Acad Sci U S A* **102**, 10012-10016 (2005).

19. Xiao, M. *et al.* Rapid DNA mapping by fluorescent single molecule detection. *Nucleic Acids Res* **35**, e16 (2007).

20. Mak, A. C. Y. *et al.* Genome-Wide Structural Variation Detection by Genome Mapping on Nanochannel Arrays. *Genetics* **202**, 351-362 (2016).

21. Marie, R. *et al.* Single-molecule DNA-mapping and whole-genome sequencing of individual cells. *Proc Natl Acad Sci U S A* **115**, 11192-11197 (2018).

22. Reisner, W. *et al.* Single-molecule denaturation mapping of DNA in nanofluidic channels. *Proc. Natl. Acad. Sci. USA* **107**, 13294-13299 (2010).

23. Teague, B. *et al.* High-resolution human genome structure by single-molecule analysis. *Proc. Natl. Acad. Sci. USA* **107**, 10848-10853 (2010).

24. Hastie, A. R. *et al.* Rapid genome mapping in nanochannel arrays for highly complete and accurate de novo sequence assembly of the complex Aegilops tauschii genome. *PLoS One* **8**, e55864 (2013).

25. Reccius, C. H., Stavis, S. M., Mannion, J. T., Walker, L. P. & Craighead, H. G. Conformation, Length, and Speed Measurements of Electrodynamically Stretched DNA in Nanochannels. *Biophys. J.* **95**, 273-286 (2008).

26. Gupta, D. *et al.* Mixed confinement regimes during equilibrium confinement spectroscopy of DNA. *J. Chem. Phys.* **140**, 214901 (2014).

27. Gupta, D. *et al.* Experimental evidence of weak excluded volume effects for nanochannel confined DNA. *ACS Macro Lett.* **4**, 759-763 (2015).

28. Utko, P., Persson, F., Kristensen, A. & Larsen, N. B. Injection molded nanofluidic chips: fabrication method and functional tests using single-molecule DNA experiments. *Lab Chip* **11**, 303-308 (2011).

29. Iarko, V. *et al.* Extension of nanoconfined DNA: Quantitative comparison between experiment and theory. *Phys. Rev. E* **92**, 062701 (2015).

30. Function - Alignsignals. https://www.mathworks.com/help/signal/ref/alignsignals.html?s_tid=doc_ta Web. Accessed - 6/12/2019.

31. Gupta, D., Bhandari, A. B. & Dorfman, K. D. Evaluation of Blob Theory for the Diffusion of DNA in Nanochannels. *Macromolecules* **51**, 1748-1755 (2018).

CHAPTER 4 – CHARACTERIZATION OF DNA TRANSPORT

4.1 – Introduction

Solid-state optical mapping platforms will be advanced by a deeper understanding of DNA transport in nanochannels. The influence of non-specific surface interactions on DNA fragments can lead to stick-slip motion and other detrimental DNA-wall interactions like Mg bridging, limiting the utility of optical mapping applications. Experiments analyzed according to the methods described in Chapter 3 were performed to investigate DNA transport characteristics in a multitude of mapping-type scenarios with the ultimate goal of reducing detrimental DNA-wall interactions. All experiments performed on COP devices were from the same fabrication batch to facilitate accurate experimental comparisons. Additionally, numerous experimental controls were developed and performed pre- and post-DNA transport experiment to gain additional information about device performance and verify experimental conditions. The following characteristics and conditions of DNA transport were analyzed:

1. DNA transport in Quartz vs. COP devices
2. DNA size-dependent diffusion characteristics
3. The influence of Mg cations on DNA transport
4. Using herring sperm oligonucleotides as a dynamic nanochannel coating to minimize detrimental DNA-wall affects
5. DNA size-dependent transport efficiency
6. The influence of nanochannel path length on DNA transport

DNA transport controls were developed to verify analogous conditions existed for comparative studies and offer additional information about device performance. The following controls were explored and developed:

1. Laser-induced photodamage control
2. Using conductivity measurements to determine device performance
3. Using Mg Green as a Mg indicator for experimental quality assurance

Briefly, laser power control was used to determine an appropriate laser power and verify that the laser did not cause DNA photocleavage as it transported through the serpentine nanochannel. Conductivity measurements were used to measure the resistance and electrolytic current through various nanochannel paths of the device, and was used to troubleshoot nanochannel blockages and otherwise malfunctioning devices. Experiments that included Mg cations used a Mg Green quality control step prior to the experiment to verify the presence of Mg in the nanochannel at steady-state electrophoresis. Each DNA transport experiment in this section utilized the laser-line setup, HindIII digest, and data acquisition process previously described to offer new insights into DNA transport characteristics on the Genturi devices. While the research here has obvious translational use to mapping applications, it also has additional utility to basic research in advancing nanofluidic manipulation of macromolecules – particularly in the sections describing diffusion characterization, the size-dependence of transport efficiency, and development of oligonucleotide dynamic coating to minimize DNA-wall interactions.

4.2 – Developing Controls for DNA Transport Experiments

4.2.1 – Laser-induced Photocleavage

A potential concern for DNA under light illumination, especially higher intensity laser sources is that polynucleotides can be photocleaved into smaller fragments. For these experiments, DNA transports through the laser line three times, schematically illustrated by the three ROIs in Figure 4.1. Moreover, it is possible that DNA transporting through ROI 1 can be photocleaved by the laser excitation, creating smaller DNA fragments that will appear at ROI 2 and inhibit DNA fragment calling between ROIs. A control experiment was designed to determine the amount of photodamage sustained by the DNA as it is transported through the ROIs with the goal of identifying and subsequently minimizing the number of photocleaved fragments at ROI 2 compared to ROI 1. Two main factors determine the degree of DNA fragmentation: electric field strength or transport velocity through the ROI, and laser power. A COP device was primed according to the protocol described in Chapter 3 to test for DNA photocleavage. DNA was electrokinetically transported through the nanochannel at field strengths of 52 and 9 V/cm and laser powers of 0.9, 0.5, and 0.2 mW. Table 4.1 lists the magnitude of fragmentation sustained taken as the percentage increase of fluorescent molecules detected in ROI 2 compared to ROI 1. The increase in molecules detected signifies the DNA is photocleaved into smaller fragments. DNA driven at 52 V/cm

(approximately 72 μm/s) sustains less total laser illumination than DNA at 9 V/cm and had less than a 2% increase in detected fragments at ROI 2 compared to ROI 1. DNA driven under the 9 V/cm field strength exhibited fragmentation rates of 25%, 38%, and 92% as the laser power increased. As expected, the 0.9 mW laser power photocleaved the most molecules (92%) while the 0.2 mW power damaged the fewest molecules (25%). All succeeding experiments utilized a 52 V/cm E-field to minimize DNA fragmentation; in addition, the laser power was attenuated at 0.2 mW as an added precaution.

4.2.2 – Utilizing Conductivity Measurements to Determine Device Performance

Early DNA transport experiments were plagued by malfunctioning devices and experimental inconsistencies. For example, in a large subset of experiments, DNA transport through the nanochannel did not occur. One potential explanation for the lack of DNA transport witnessed was that the nanochannel interface for that batch of devices was partially occluded or blocked. Visually inspecting the nanochannel is difficult at the sub-micron length scales; instead, the use of conductivity measurements was chosen to characterize ion transport and subsequently device performance at the nanoscale.[1-3] Therefore, conductivity controls measuring the current through the nanochannel pre- and post-experiment were developed in order to obtain more information about device performance.

4.2.2.1 – Conductivity Measurements in Nanochannels

Multiple measurable paths exist in the Genturi device design. Figure 4.2 illustrates the networked nanochannel segments, each of which serves as a potential path for conductivity measurement. A total of six paths were measured: V1-V2, V1-V3, V1-V4, V2-V3, V2-V4 and V3-V4. Since the nanochannel is an order of magnitude smaller in both dimension and cross-sectional area it will have the greatest resistance to flow and largest voltage drop; therefore, it was assumed that the conductivity measurements were dominated by the nanochannel and nanochannel/microchannel interface. For these experiments, all devices were primed using the priming protocol described in Chapter 3. As a reminder, the priming buffer contains: 1X Cutsmart (tris acetate), 2% PVP, 0.1% Tween-20, 0.1% BSA, and 0.2 mM DTT. Devices were stored at 4 °C for 24 h prior to use, after which they were removed and allowed to come to room temperature prior to measuring the conductivity. A Keithley picoammeter/voltage source (Model 6487) was used to make conductivity measurements using an applied voltage of 3 V. Platinum electrodes were inserted into the vias to measure the conductivity through different sections of the microchannel and

nanochannel. Each measurement was taken after the current reading was allowed to equilibrate for 60 seconds after placing the electrodes. Current in both directions were measured by switching the positive and negative electrodes to determine consistency in the conductivity measurement and to inspect for ion depletion or other factors that could negatively influence measurement utility.

4.2.2.2 – Conductivity Model

Creating a model of the expected current across the nanochannels was required to facilitate comparison of empirical results. The nanochannel conduit is separated into segments based on the channel dimensions and fluidic network. The resulting modeled segments were as follows: the entrance nanochannel, the V2 slits and slit interspacing, the serpentine nanochannel, the V3 slits and slit interspacing, and finally the exit nanochannel (Figure 4.2). These segments were modelled as resistors in series and parallel using Pouillett's law, Kirschoff's circuit law, and Ohm's law:

$$\textit{Pouillett's Law} \qquad R = \rho \frac{L}{A} \tag{23}$$

$$\textit{Kirschoff's Circuit Law} \qquad \sum_{k=1}^{n} V_k = 0 \tag{24}$$

$$\textit{Ohm's Law} \qquad V = I\,R \tag{25}$$

where R is the resistance, ρ is the resistivity, L is the length of the nanochannel segment, A is the cross-sectional area, n is the number of voltages measured, V is the voltage, and I is the current. Equations 1-3 were used to calculate the expected currents and resistances through each nanochannel segment with 3 V applied and are shown in Table 4.2. As a comparison, these numbers were in good agreement with numbers determined with the circuit modelling program LTspice.

If a nanochannel defect or blockage exists, it is possible to isolate the affected nanochannel segment by comparing measured to expected conductivity. Therefore, including conductivity measurements at V2 and V3 in addition to V1 - V4 provides further comparison points for identification of the blockage location. For example, if all permutations of conductivity paths are close to the expected values except for the paths containing V4, that suggests that there is a problem at the nanochannel exit/ microchannel interface or there is a blockage in the exit nanochannel segment. Blockages manifested themselves in current measurements < 1 nA, and therefore served as identification of non-functional devices unsuitable for experiments.

4.2.2.3 – Current Measurement Validation in Quartz Devices

Quartz devices with a similar design to the COP devices have been used by the Ramsey group for mapping applications in the past.[4] A quartz device was chosen to validate the conductivity model first because of the demonstrated substrate-coverslip bonding fidelity from thermal bonding at 1000 °C. The quartz device was fabricated with the same design and dimensions as the Genturi devices – four microfluidic channels connected by a single serpentine nanochannel.[4-6] The quartz device was primed using the same protocol as the COP devices. Conductivity measurements were taken to determine the current through each nanochannel segment in the priming buffer (5.57 µS/cm bulk conductivity), the results of which are shown in Figure 4.3 along with the expected currents. The empirical measurements taken from the quartz device were in very close agreement with the conductivity model, ranging from a 20-35% difference depending on the path. Any small differences between the measured and expected values, particularly of the V1-V2 and V3-V4 paths, are attributed to the nanochannel funnels which are not included in the model. Of particular importance to note here is that the empirical current measurements agree with the model and the thermal bonding of the quartz coverslip to the quartz substrate is highly uniform and robust.[7]

4.2.2.4 – Current Measurements in COP Devices

Currents were measured in COP devices in the same manner as the quartz devices. The measured currents in the COP devices were significantly different from the expected currents. Figure 4.4 shows the currents measured in three devices compared to the expected current. The measured currents were significantly higher than expected for every path, ranging from a 500 - 50,000% increase over the model. The orders of magnitude higher current measurements in COP devices was surprising given the current agreement in the quartz device in the same priming buffer. The presence of nanoscratches or incomplete bonding was thought to be a contributing factor in this increased current. An experiment was designed to test the possible contribution of surfactants in the passivation buffer to wet the nanoscratches/unbonded areas potentially creating shorts. The effect on the current of the amount of time the surface was exposed to the buffer was also investigated. In these experiment the conductivity was tested at various time points over two days. First, a COP device was primed and the currents immediately measured. The priming buffer (1X Cutsmart (tris acetate), 2% PVP, 0.1% Tween-

20, 0.1% BSA, and 0.2 mM DTT) was measured with an Orion conductivity probe (Thermo Scientific) to have a bulk electrical conductivity of 5.57 µS/cm at 20 °C. Next, the priming buffer was replaced with 1X Cutsmart (2% PVP, and 0.1% BSA, no Tween-20 or DTT) which was measured to have a bulk conductivity of 5.41 µS/cm at 20 °C. Figure 4.5 shows the results from the current measurements on the first day. There was only a 5-15 nA difference between conductivity measurements taken in the priming buffer and the 1X Cutsmart, with both measurements orders of magnitude greater than the expected conductivity. The device was then stored for an additional 24 h at 4 °C in 1X Cutsmart. The following day the device was removed and allowed to return to room temperature for 2 hours before additional conductivity measurements were performed. The conductivity was measured again at 1 and 2 h after reaching room temperature (3 and 4 hours after removal from the refrigerator). Figure 4.6 illustrates the resulting trend in the measured current. There was little to no difference between measurements taken in the passivation solution (with surfactant) and in 1X Cutsmart (without surfactant). However, measurements taken after 24 hours at 4 °C plus 2 hours at room temperature resulted in conductivity measurements that more closely approximated the model. The current continued to move closer to the expected current values over time.

The COP conductivity results led to the following conclusions. First, seemingly identical devices out-of-box have entirely different current measurements and subsequently different DNA transport capabilities. Second, primed COP devices have current measurements an order of magnitude greater than expected. However, these values decrease over time / active electrophoresis. It is apparent from the data that the passage of time appears to result in current measurements closer to expected from the model. More difficult to comprehend is the potential role active transport of ions / active electrophoresis may have on the system since it is impossible to isolate the two as testable variables. Approximately 10 minutes of active electrophoresis occurred during the measurements necessary to create Figures 4.5 and 4.6. The following question still exists, what would cause the current to decrease towards the expected values? Or rather, why are the initial current measurements so high? The leading hypothesis is that the COP devices are actually not completely sealed fluidic conduits, but instead may have small nanoscratches or local debonded regions between the substrate and coverslip. These small interface defects (likely < 15 nm) become filled fluidic conduits when in the presence of the surfactants present in

the priming buffer. This would explain both the large current values obtained and the difference in current values from device-to-device. When the surfactants are removed from the buffer, the current measurements approach the expected values by two potential methods: either the surfactants diffuse out of the debonded areas / nanoscratches, or those small areas become clogged by PVP or BSA and thus no longer actively transport ions.

4.2.2.5 – Establishment of Conductivity Control

Dissimilar current measurements from device-to-device pose issues for establishing consistency in DNA transport experiments. Thus, a control step where the conductivity of the channels for each device are measured using priming buffer was implemented to determine chip suitability for experiments. Potential nanochannel blockage issues that exist were immediately apparent and indicated by abnormally low current values in the respective blocked path (< 1 nA). Priming buffers were then replaced with experiment buffers. The DNA transport experiment would be performed, successfully or unsuccessfully, and the conductivity measured post experiment in the experimental buffer (1X Cutsmart, DNA, and Mg^{2+} depending on the experiment). Figure 4.4 illustrates the differences in conductivity for three devices pre-experiment. DNA successfully transported through the nanochannel for 3+ hours in all three devices. Similar to the aforementioned time/electrophoresis experiment, the post-experiment conductivity of all three devices in Figure 4.7 is in close agreement with expected values. The conductivity data in Figure 4.7 provides additional support for the performance of the device, and is necessary when building out replicates for buffer component variables or inspecting the utility of dynamic coatings. Each device used for experiments was fully vetted by this conductivity control step pre and post experiment and measured currents were in general agreement with the expected currents from the model. Devices with nanochannel blockages or significant debonded regions were recognized and discarded.

4.2.3 – Quality Assurance: Using Mg Green to Determine Presence of Mg in the Nanochannel

4.2.3.1 – Mg Green Verification with Mercury Arc Lamp Illumination

The presence of Mg ions in the nanochannel is critical to mapping applications that rely on cofactors for restriction digestion in nanochannel confinement. Therefore, experiments were designed to confirm the presence of Mg ions in the nanochannel during DNA transport. In these experiments Magnesium Green (Thermo Fisher Scientific) was used as a Mg indicator to verify the presence of Mg in

the nanochannel. Mg Green is a pentapotassium salt (506/531 nm absorption/emission spectra) that exhibits a high affinity for divalent cations and has a negative charge due to a number of deprotonated oxygen atoms on the molecule. Conversely, Mg cations are positively charged (2+). Mg Green molecules and Mg cations will transport towards the positive and negative electrodes, respectively. The counter-directional transport of Mg cations and Mg Green molecules causes interaction and subsequent binding of the two molecules to occur in the nanochannel, where complexed Mg – Mg Green fluoresces (531 nm) at an increased emission intensity compared to uncomplexed Mg Green. In these experiments, with similar buffer composition to both DNA fragment transport and mapping experiments, the presence of 5 mM EDTA in V1 chelates many free Mg ions available to bind to Mg Green. This is necessary in mapping experiments to avoid DNA digestion prior to injection to the nanochannel. EDTA has a negative charge and is expected to transport in the same direction as DNA, meaning that EDTA continually flows through the nanochannel during electrophoresis. EDTA was also added to the Mg Green experiments at a 5 mM concentration to confirm the presence of unchelated Mg ions in the same conditions as transport experiments. The fluorescence intensity increase of complexed Mg-Mg Green was used as the chosen verification metric.

Experimental buffers were applied to the same vias as a typical transport experiment (V1 - 1X Cutsmart 5 mM EDTA, V2 – 1 X Cutsmart, V3 & 4 – 1 X Cutsmart 5 mM Mg), except 30 μM Mg Green was added to the V1 buffer instead of the HindIII digest DNA. Furthermore, Mg Green and Mg cations were driven into the nanochannel with a 52 V/cm electric field. Instead of a laser line excitation source, a mercury arc lamp (Nikon) and filter cube with a 488 nm long-pass filter (Semrock) were used to illuminate the majority of the serpentine nanochannel. Figure 4.8 illustrates the result of the Mg – Mg Green complex fluorescence at steady-state averaged over 30 s in the nanochannel. The first thing to note is the uniform fluorescence intensity throughout the nanochannel. Figure 4.9 attempts to quantify the fluorescence intensity with use of line profiles. The fluorescence intensity uniformity of Mg-Mg Green through the nanochannel suggests that transporting DNA experiences a constant concentration of Mg ions during transport. Serendipitously, a small fabrication defect was discovered in all devices tested, shown by the blue circle in Figure 4.8. The slight change in fluorescence intensity at the beginning of the first curve in the nanochannel indicates that the beginning segment of the nanochannel is smaller than

the rest. The defect is not visible using brightfield illumination. This defect was detected in all tested devices; therefore, it is not expected to influence any of the outcomes discussed in this chapter. The use of a fluorescent indicator like Mg Green made the identification of defects in the nanochannel and other batch quality issues possible. Most importantly, the uniform concentration of Mg in the nanochannel is a positive result for optical restriction mapping applications that require cofactor activation.

4.2.3.2 – Mg Green Control-step Development

Mg Green was used in the development of a control step pre-transport experiment, where it was used to verify Mg ions were present in the nanochannel at steady state electrophoretic flow. This control step was performed prior to the DNA transport experiment and after the device had completed the 24 hour priming protocol. First, priming solution was aspirated from each via with house vacuum. Next the following solutions were added to each via to determine the background fluorescence of Mg Green without Mg.

V1: 1X Cutsmart, 5 mM EDTA, 30 μM Mg Green

V2: 1X Cutsmart

V3: 1X Cutsmart

V4: 1X Cutsmart

Charge–dependent transport of Mg Green was driven by a 52 V/cm electric field in the nanochannel. The laser-line setup was used to measure the non-complexed Mg Green fluorescent intensity in regions where the laser-line intersected the nanochannel. Voltages and electric field were zeroed for 40 seconds before changing to 52 V/cm for 40 seconds and finally returning to zero for an additional 40 seconds. The following solutions were subsequently added to each via to determine the fluorescence with Mg.

V1: 1X Cutsmart, 5 mM EDTA, 30 μM Mg Green

V2: 1X Cutsmart

V3: 1X Cutsmart, 5 mM Mg

V4: 1X Cutsmart, 5 mM Mg

Figure 4.10 illustrates the fluorescence of complexed Mg-Mg Green. The voltage scheme at the top of the figure corresponds to the 80 seconds where electrophoretic transport was switched off (V_{off}) and the

40 seconds in between where it was activated (V_{on}). The difference between Figure 4.10(A) and (B) is readily apparent. Figure 4.10(A) is fluorescence signal from unbound Mg Green. Figure 4.10(B) is in the presence of Mg cations, and thus has a greater fluorescence response due to complexed Mg-Mg Green. All of the DNA transport experiments discussed in this chapter saw a similar Mg-Mg Green response to Figure 4.10(B), indicating that Mg ions were present in the nanochannel.

4.3 – Results and Discussion

4.3.1 – DNA Transport in Quartz and COP Devices

Comparing DNA transport properties in quartz vs COP served as a good starting point given the prior DNA extension work in Chapter 2. A comparative study was designed to determine if there were differences in transsport efficiency between quartz and COP devices as measured by the relative quantities of correctly-called, incorrectly-called, and missing fragments. Both devices featured the same nanofluidic design and were primed in accordance to the priming protocol found in Chapter 3. The first experiments did not contain Mg. Instead, 1X Cutsmart 5 mM EDTA was added to each via and 10 ng/μL λ-HindIII ladder stained with YOYO-1 at a 10:1 bp:dye ratio was added to V1.

Figure 4.11 shows the DNA fragment size histograms generated by each device. There are a few things to consider. First, the peak shapes (fragment size) on the quartz device are slightly different from the COP peaks as there is a clear separation between the 6.6 kbp and 9.4 kbp fragments in the quartz device. In addition, peaks in the COP device are not as pronounced. In this case the peak shape can be attributed to DNA handling prior to YOYO-1 staining. It was discovered that λ-HindIII digests require a heating step prior to electrophoresis to dissociate annealed 4.4 kbp fragments from 23.1 kbp fragments.[8] Without this heating step the 4.4 kbp fragment peak nearly disappears as seen for the DNA transport in the quartz device. The ratio of missing fragments in the quartz histogram (2.2 kbp: 8.3%, 4.4 kbp: 3.8%, 6.6 kbp: 3.0%, and 9.4 kbp: 2.5%) is similar to the ratio of the COP histogram (2.2 kbp: 8.4%, 4.4 kbp: 8.1%, 6.6 kbp: 3.3%, and 9.4 kbp: 2.6%). The ratio of incorrectly-called fragments in the quartz histogram (2.2 kbp: 12.0%, 4.4 kbp: 32.8%, 6.6 kbp: 11.6%, and 9.4 kbp: 10.2%) is slightly lower than the ratio of the COP histogram (2.2 kbp: 19.5%, 4.4 kbp: 31.0%, 6.6 kbp: 17.6%, and 9.4 kbp: 15.4%). In summary, the COP device performed slightly worse than the quartz device in the number of incorrectly-called fragments and equal in the number of missing fragments; however, the COP devices has the benefit of cheap production while quartz devices are expensive and laborious to fabricate. COP mapping devices are marketable for commercial use and represent the future of mapping platforms; therefore, all following DNA transport experiments were performed on the COP devices.

4.3.2 – DNA fragment-size-dependent Transport

To mimic a mapping experiment where DNA fragments of different sizes would be transported, a HindIII digest with varying fragment sizes was used. The analysis method enabled investigation into fragment-size-dependent diffusion by comparing the arrival time of each fragment to the cross-correlation lag. As discussed in previous chapters, DNA molecules experience axial diffusion during transport through nanochannels and nanoslits.[9-13] The axial diffusion coefficient (diffusivity), D_t, is approximated as:

$$D_t \cong D_R \left(\frac{D^2}{wP}\right)^{\frac{1}{3}} \quad (26)$$

where w is the effective width of a DNA, P is the persistence length, D is the square channel size, and D_R is the Rouse diffusivity of a freely draining chain.[14] The Rouse diffusivity is dependent on both solvent viscosity and contour length, η and L_c, respectively:

$$D_R = \frac{k_B T}{6\pi\eta L_c} \quad (27)$$

Combining equations (4) and (5) leads to the following equation:

$$D_t \cong \left(\frac{k_B T}{6\pi\eta L_c}\right)\left(\frac{D^2}{wP}\right)^{\frac{1}{3}} \quad (28)$$

In equation (6) the vast majority of variables are constants in the DNA transport system given the temperature, nanochannel dimensions, solution viscosity, and ionic strength of the solution are independent of molecule size. However, the contour length (length at full extension) is fundamentally based on molecule size, serving as the basis for the dependence of axial diffusion on molecule length.

DNA molecules were isolated based on their size to calculate the diffusivity of each fragment. Each DNA fragment size found in the HindIII digest, 2.2, 4.4, 6.6, 9.4, and 23.1 kbp were investigated. The transport time difference between ROI 1 and ROI 2 post cross-correlation transport shift was determined for each molecule as a first step in determining the axial diffusion each molecule experienced.

DNA travels at a constant velocity independent of fragment size,[15] eliminating the need to determine size-specific velocities. Figure 4.12 shows the probability of fragment position experienced by each fragment size population due to axial diffusion. A trend emerges, the distribution of smaller fragments is wider than large fragments, signifying a greater degree of axial diffusion. All fragments experienced axial diffusion; however, it is important to note that the total distance diffused is not captured here as this figure serves as a snapshot of the effects of diffusion after a period of time and transport. In addition, all of the histograms in Figure 4.12 are centered at 0 μm. Negative diffusion (to the left of 0 μm) came from fragments that appeared late, or ms after they were expected. Positive diffusion (to the right of 0 μm) came from fragments that were earlier then the cross-correlation lag. The normality of each histogram shape suggests that diffusion is the main cause of the fragment arrival distribution. For example, if viscous drag or friction affected a subset of the molecules only the left side of the histogram or varying distances of molecule 'slowing', would be expected. However, the histogram in Figure 4.12 shows both positive and negative directions and serves as evidence that diffusion is the main cause of the distribution. The standard deviation of each histogram was taken to determine the diffusivity of each fragment size population.

The diffusion of DNA free in solution is well-studied. *Robertson et al.* found that the diffusivity of linear DNA in free solution scales according to $D \sim L_c^{-0.571 \pm 0.01}$.[16] Yet, empirical work investigating diffusion in nanochannels is nearly non-existent.[9] Simulations of DNA diffusivity in nanochannels at sizes expected to force the backfolded Odijk regime (approximately ~50 - 100 nm) suggest that diffusivity should be independent of channel size:

$$D_t \approx 1.75 \, ln\left(\frac{P}{a}\right) D_R \qquad (29)$$

where a is the DNA hydrodynamic radius.[14] The simulations agree with the scaling of a nondraining object whose friction is proportional to the fragment bp size (-1) and therefore remains valid for the extended de Gennes and classic de Gennes regime.

DNA contour lengths, radius of gyration, and persistence length, were calculated to investigate the relationship between diffusivity theory and nanochannel experiments. Unstained DNA contour length

is 0.34 nm per base pair,[17] but YOYO-1 intercalation is expected to increase the contour length by approximately 0.44 nm per dye molecule.[18] Experiments were performed with 10:1 bp:dye ratio, so the stained DNA contour length was approximately 0.384 nm/bp. Table 4.3 shows the expected contour length for each HindIII fragment. The radius of gyration and persistence length were 3.2 Å and 50 μM, respectively.[19] The predicted diffusivity of each HindIII fragment is compared to experimental results in Figure 4.13. Important to note here is that the red trace of *Muralidhar et al.*'s simulation is an exact solution, not just a scaling representation, and that it also approximates the diffusivity in channels with critical dimensions 4x smaller than the devices used. The experimental, simulation, and bulk diffusivity power law scalings are -0.77±0.03, -1, and -0.57±0.01, respectively. The prefactors used in equation (7) were used to plot the data for the Rouse diffusivity simulation in accordance with the HindIII fragment sizes. Experimental and simulation comparisons hence represent actual expected diffusivity for the DNA at their respective sizes. The simulation and experimental data agree for the 2.2 kbp fragment size, but quickly depart given the more negative scaling of the Rouse simulation. On the other hand, prefactors were not available for *Robertson et al.*'s work; consequently, the trace in Figure 4.13 does not represent actual expected diffusivity but rather illustrates expected scaling instead for comparison purposes. Further experimentation with additional DNA ladders is necessary to draw conclusions and was not possible here due to the number of available devices for further experimentation. In addition, the magnitude of diffusivity of DNA fragments is highly sensitive to changes to ionic strength which were not measured as part of this experimental series. All withstanding the diffusivity data should be treated as suggestive instead of definitive and is included as preliminary data to highlight additional areas of potential utility obtained through the data analysis method.

4.3.3 – The Influence of Mg in the Nanochannel System

Numerous DNA transport experiments were performed in COP devices to determine the influence of buffer constituents on DNA transport. One major motivation for developing a method capable of analyzing DNA transport was to determine how divalent cations influenced DNA transport. Divalent cations are critical components of mapping applications as they serve as activators for restriction enzymes.[20,21] In addition they also may affect a variety of phenomena at the nanoscale due to their

charge. Cations like Mg^{2+} are positively charged while the walls of COP take on a negative charge due to deprotonation from the basicity of the experimental buffers.[22] It was hypothesized that Mg^{2+} may associate with the oppositely charged COP walls and influence DNA transport behavior. Comparative experiments were therefore designed to determine the influence Mg cations had on DNA transport. Transport data from experiments without Mg served as a control for comparative purposes and are labelled 'No Mg' in subsequent figures.

COP devices were primed, measured for conductivity, and passed the Mg Green indicator controls. Next, the following experimental buffer solutions were added depending on whether it was a Mg or No Mg experiment. YOYO-1 was pre-bound to the HindIII digest DNA fragments for a period of 1 hr. The No Mg experimental buffer solutions were as follows:

V1: 1X Cutsmart, 5 mM EDTA, 10 ng/μL HindIII digest 10:1 YOYO1:bp dye

V2: 1X Cutsmart, 5 mM EDTA

V3: 1X Cutsmart, 5 mM EDTA

V4: 1X Cutsmart, 5 mM EDTA

The experimental buffer containing Mg was as follows:

V1: 1X Cutsmart, 5 mM EDTA, 10 ng/μL HindIII digest 10:1 YOYO1:bp dye

V2: 1X Cutsmart

V3: 1X Cutsmart, 5 mM Mg

V4: 1X Cutsmart, 5 mM Mg

The inclusion of Mg and the location of EDTA were the only differences between experiments. Both sets of experiments were run with the exact same conditions: HindIII digest, 52 V/cm, 3+ hour data acquisition time, and 10 ms frame acquisition.

DNA transport with buffer containing Mg immediately showed qualitative differences compared to the no Mg buffer. Injection of DNA into the nanochannel was less frequent and stick-slip motion was apparent as a subset of DNA appeared to hesitate at the ROIs. Figure 4.14 shows the histogram of DNA fragment sizes between the Mg (10,708 total DNA fragments analyzed) and No Mg (6,770 total DNA fragments analyzed) experiments. The experiment with Mg has a greater percentage of incorrectly-called

and missing fragments than the experiment without Mg. This result is confirmed by calculating the mixing (M) and incorrectly-called (IC) fragment percentage, M / (CC+IC+M) and IC / (CC+IC+M), respectively, and where CC is the number of correctly-called DNA fragments. These two metrics are combined to equal the percentage of fragments with impacted transport (IT). Table 4.4 shows the difference between missing, incorrectly-called, and impacted transport fragments from both experiments. The presence of Mg increases the number of missing and incorrectly-called fragments. Moreover, the number of fragments with impacted transport Mg in the system is nearly double that without Mg. Figure 4.14 and Table 4.4 also show that small DNA fragments are more highly affected by the inclusion of Mg, and that there may be an impacted transport size-dependence. In effect, the inclusion of Mg is detrimental to DNA transport. Nonspecific surface interactions causing stick-slip motion or DNA-wall interactions like Mg bridging would explain the increase of fragments that experience impacted transport.

The occurrence of incorrectly-called and missing fragments are both detrimental to mapping applications, however missing fragments are more harmful as they would appear as false mutations in data analysis algorithms. It is therefore essential to minimize missing fragments in the system. Assuming Mg-DNA bridging to channel walls is the primary culprit, it was theorized that it may be possible to passivate the nanofluidic channels by including a high concentration of <100 bp DNA fragment populations into the experimental buffers. In this way the small DNA fragments (<100 bp) will associate with bound Mg instead of the larger (2.2 – 23.1 kbp) fragments. Fragments smaller than approx. 500 bp are not detected with the laser-line setup, so inclusion of <100 bp fragments would not affect DNA transport analysis.

4.3.4 – Using Herring Sperm DNA as a Dynamic Coating

The inclusion of Mg cations into the DNA transport system severely impairs device performance. DNA transport through the nanochannel is impacted by stick-slip motion, DNA-wall affinity, and Mg-bridging in the presence of Mg cations. Oligonucleotides like degraded herring sperm DNA have successfully been used to passivate hydrophobic membranes in the past.[23-25] The addition of oligonucleotides into the HindIII DNA sample may act as a dynamic coating where the oligonucleotides will compete with the HindIII fragments for channel wall Mg-DNA bridging sites, benefiting overall HindIII fragment transport. Degraded herring sperm is commercially available (Sigma Aldrich) and comprised of

small oligonucleotides less than 50 bp in length. The minimum DNA molecules sizing threshold is set at approximately 500 bp so the oligonucleotides will not influence DNA sizing as long as the fluorescent background remains below the peak threshold for detection.

Herring sperm was added into the priming and experimental buffers to determine its utility as a dynamic coating. Dehydrated herring sperm was reconstituted in deionized water and added to the priming buffer at a concentration of 0.33 ng/μL. Reconstituted DNA was refrigerated at 4 °C between experiments to minimize degradation. The priming protocol was otherwise kept consistent with prior experiments. Herring sperm was added into each experimental buffer at a concentration of 0.33 ng/μL. Transport of negatively charged herring sperm into the nanochannel during the experiment was assumed to act as a dynamic coating due to its continual replenishment over the data acquisition period. Herring sperm was added after the YOYO-1 DNA staining step to minimize background fluorescence in the nanochannel. All herring sperm experiments were performed in the presence of 5 mM Mg.

A comparison of the herring sperm experiments to non-herring sperm DNA transport experiments is presented in Figure 4.15. Each data point represents the impacted transport percentage (missing + incorrectly-called) of translocating DNA fragments in an individual device. No Mg, Mg, and Mg w/ HS Coating titles on the x-axis represent experiments without Mg (15.0%), experiments with Mg (43.8%, 36.0%, 33.5%, and 34.5 %), and experiments with Mg and herring sperm (19.4%, 20.7%), respectively. All devices for this experimental comparison were from the same batch and passed the conductivity / Mg Green quality controls. The first thing to notice is the disparate number of data points for each condition due to a number of devices that failed the quality controls due to blockage issues. Nonetheless, devices with herring sperm dynamic coatings performed better than control experiments (with Mg), and nearly approached the impacted transport percentage of experiments without Mg. This data suggests that herring sperm increased the transport efficiency of DNA and lends credence to the theory presented of Mg-DNA bridging as a large contributor of DNA-wall affinity. The metric impacted transport is further broken down into the percentage of missing and incorrectly-called fragments in Figures 4.16 and 4.17. A similar trend, albeit with more spread, is observed. The missing fragment percentage for each experimental series is as follows: No Mg – 6.6%, Mg – 12.4%, 12.8%, 13.5%, 10.8%, and Mg w/ HS coating – 6.4%, 6.6%. In addition, the incorrectly-called fragment percentages had the most spread, each

experimental series is as follows: No Mg – 8.5%, Mg – 31.5%, 23.1%, 20.0%, 23.6%, and Mg w/ HS coating – 13.0%, 14.1%. Interestingly, both missing and incorrectly-called fragments display the same trend as each other. The similarity in trend between missing and incorrectly-called fragments was not expected due to incorrectly-called fragments containing a degree of random error due to Brownian motion in the nanochannel; but nonetheless lends support to the validity of using a sum of both, impacted transport, as the main comparative metric for transport performance. Also interesting to note, analysis of transporting fragments generally assigned more incorrectly-called fragments then missing fragments. Decreased impacted transport percentage of Mg w/ HS Coating experiments was nearly to that of the best-performing No Mg experiments, where DNA transport behavior was well behaved and stick-slip motion and DNA-wall affinity was minimal.

4.3.5 – DNA Fragment Size Specific Transport Efficiency

The influence of HindIII digest fragment size on transport efficiency was investigated. DNA fragment sizes were binned according to their respective sizing distributions on the histogram plots to analyze how different fragment sizes were called relative to each other. As mentioned above, the percentage of missing fragments and incorrectly-called fragments for the No Mg, Mg, and Mg w/ HS coating are shown in Figure 4.16 and 4.17, respectively. Figure 4.18 shows a size-dependent decrease in the percentage of missing fragments going from Mg to Mg/HS to no Mg present buffers, while Figure 4.19 shows a size-independent trend. However, the data in both figures converges on a familiar universal trend, transport in experiments with Mg perform poorly in comparison to No Mg and Mg with HS coating experiments.

An implication from this data is that large fragments transport more efficiently and predictably than smaller fragments. This trend cannot be explained by momentum as molecules / fluids at this length scale are generally non-Newtonian. However, electric fields impose a greater size-dependent force on DNA molecules during electrokinetically-driven transport due to the total count of negatively charged phosphate groups in the molecule backbone. If DNA-wall affinity or Mg-bridging is viewed as a point force on the molecule that acts in the direction of the channel wall, then larger DNA strands would more easily overcome that point force by size-dependent forces in the electrokinetic direction. In summary, long DNA strands are more likely to overcome DNA-wall interactions. Contrasting with Figure 4.18,

Figure 4.19 does not show the same dependence on size. Incorrectly-called fragment percentages instead appear unaffected by DNA fragment size, hinting that there are independent causes responsible for missing and incorrectly-called fragments. This conclusion can be further explained by the large portion of incorrectly-called fragments that arise from random error in the system which does not preferentially select for certain DNA sizes. The DNA size specific transport efficiency discussed here has consequences for DNA mapping systems. The transport of small DNA molecules is more likely to be affected by detrimental DNA-wall interactions and cause reordering of fragments. DNA mapping platforms that utilize restriction enzymes that digest DNA into < 5 kbp fragments run the risk of size preferential DNA-wall interactions, which could cause larger fragments to transport past and reorder the DNA sample.

4.3.6 – The Impact of Path Length on Transport Efficiency

The majority of analysis compared DNA transport between ROI 1 and ROI 2. The laser-line crosses the nanochannel in three locations and ROI 3 can be used to determine the impact of path length on the DNA transport efficiency. ROI 1-ROI 3 has a much longer path length, approximately 150 μm, than ROI 1-ROI 2. Therefore, if DNA-wall interactions are responsible for the decline seen in transport efficiency in experiments with Mg then it would be expected that a longer path length would result in decreased transport efficiency. For this analysis, transport between ROI 1-ROI 2 was compared to DNA transport between ROI 1-ROI 3 for the No Mg, Mg, and Mg with HS buffers.

Figure 4.20 shows the differences in impacted transport efficiency between the two paths. In this figure the ROI 1-ROI 2 path length, ~170 μm, was compared to the path length of ROI 1-ROI 3, ~320 μm. Figure 4.20 shows traversing a longer path length results in increased impacted transport percent or overall decreased transport efficiency. The established trend is universally observed for all transport experiments. The increase in impacted transport suggests that DNA-wall interactions influence molecule transport throughout the entire nanochannel as opposed to a single location. Once again, the addition of herring sperm oligonucleotide decreases the impacted transport percentage of fragments down to the No Mg experiments.

4.4 – Conclusions

Developing robust controls for DNA transport experiments was of paramount importance for establishing the experimental consistency necessary for experimental comparison. A brief summary of the findings from each experimental control are stated below:

1. Laser-induced photodamage control

   Conclusions – Transporting DNA is susceptible to photodamage from the laser-line. Adjusting the speed of translocation and laser power affects the degree of photodamage sustained. Tuning the electric field to 52 V/cm and laser power to 0.2 mW resulted in a negligible amount of DNA fragmentation for transporting DNA molecules.

2. Conductivity measurements

   Conclusions – A subset of COP devices out-of-box were found to have dissimilar conductivity measurements and subsequently transport performance. Many devices had nanochannel blockages that resulted in near-zero current measurement through the blocked nanochannel segment. While initial current measurements in many devices varied, the performance of devices improved with electrophoresis and time, where current measurements approached expected numbers. This experimental trend led to the following hypothesis – the bonding of COP devices with nanoscratches or incomplete bonding regions < 15 nm creates additional fluidic conduits in the presence of surfactants and subsequently lead to current measurements orders of magnitude larger than expected. However, small additional fluidic conduits become clogged during electrophoresis and no longer transport ions, resulting in a decrease in current measurement and increase in DNA transport performance. Conductivity measurements were used to gain additional information about device performance so that multiple transport experiments could be compared.

3. Mg Green indicator of Mg in the nanochannel

   Conclusions – Complexed Mg – Mg Green traces showed a uniform concentration of Mg cations throughout the nanochannel. Mg Green fluorescence also exposed fabrication defects in the nanochannel that were not visible under brightfield illumination. Using Mg Green as a Mg indicator served as supporting evidence of equal conditions for comparative experiments.

Numerous DNA transport experiments and analyses were explored. A brief summary of the conclusions from each experimental series and analysis are presented below:

1. DNA transport in Quartz vs. COP devices

   Conclusions – DNA transport in quartz versus COP devices is comparable. Quartz devices fabricated with thermal bonding exhibit slightly more consistent transport characteristics, however are more expensive.

2. DNA size-dependent diffusion characteristics

   Conclusions – DNA exhibits size-dependent diffusion and diffusivity. A power law fit to HindIII fragment diffusivity vs. HindIII fragment size has a scaling intermediate to Rouse diffusivity theory and DNA diffusivity found in empirical bulk measurements. This is the first data to examine the size influence of diffusivity in nanochannels.

3. The influence of Mg cations on DNA transport

   Conclusions – Mg cations detrimentally inhibit DNA transport in COP nanochannels by increasing stick-slip motion and DNA-Wall affinity. Mg-DNA bridging is hypothesized as a potential failure mode that affects a subset of DNA molecules during transport.

4. Using herring sperm oligonucleotides as a dynamic nanochannel coating

   Conclusions – Including herring sperm oligonucleotides decreased the percentage of fragments that experienced impacted transport in the nanochannel. The performance of the experiment without Mg observed the most consistent DNA transport. Including Mg cations in transport experiments resulted in an increased percentage of fragments with impacted transport. Including herring sperm oligonucleotides with Mg cations decreased the percentage of fragments with impacted transport back down to the best performing No Mg experiment. It was hypothesized that herring sperm oligonucleotides may compete for Mg-DNA bridging occurrences, decreasing the number of HindIII fragments affected.

5. DNA size-dependent transport efficiency

Conclusions – It was discovered that the small fragments in the HindIII ladder are more likely to be affected by detrimental transport conditions than the large fragments. This trend was universally witnessed in experiments without Mg, with Mg, and with Mg and herring sperm. The size dependence was explained by examining electrokinetic forces on the transporting fragments. If DNA-wall affinity or Mg-bridging is viewed as a point force on the molecule that acts in the direction of the channel wall, then larger DNA strands would more easily overcome that point force by size-dependent forces in the electrokinetic direction.

6. The influence of nanochannel path length on DNA transport

   Conclusions – Longer nanochannel paths resulted in a higher percentage of fragments with impacted transport. This trend was consistent for each buffer tested. The data suggests that DNA-wall interactions influence molecule transport throughout the entire nanochannel as opposed to a single location.

Many of the conclusions found in this chapter have implications for mapping platforms that rely on DNA confined in nanochannels. Missing and incorrectly-called fragments result from stick-slip motion, DNA-wall affinity, and Mg-DNA bridging to channel walls in a subset of DNA molecules during transport. Not all molecules were affected by detrimental transport phenomena like DNA-wall affinity and Mg-DNA bridging, but rather small < 5 kbp fragments were affected at a greater incidence rate. It is reasonable to predict that a combination of stick-slip motion, DNA-wall affinity, and Mg-DNA bridging could cause reordering of DNA fragments during transport. Reordered DNA fragments would be mistakenly identified as structural variants, serving as a false-positive of mutation in a DNA sample where it does not actually exist. This could inhibit the utility of mapping applications if not properly controlled. Utilizing restriction enzymes that digest DNA into large fragments could decrease reordering of fragments in the system as large fragments are not affected to the same magnitude by the detrimental transport phenomena. In addition, small HindIII fragments were determined to have greater diffusivities than large molecules. It is possible, although unlikely due to excluded volume interactions, that molecules could diffuse past each other in otherwise perfect transport conditions. This could also be avoided by utilizing large molecules

and adjusting DNA injection rate accordingly. Finally, the nanochannel design of mapping systems could benefit from minimizing the path length of transport nanochannels if suppressing reordering is desired.

4.5 – Figures and Tables

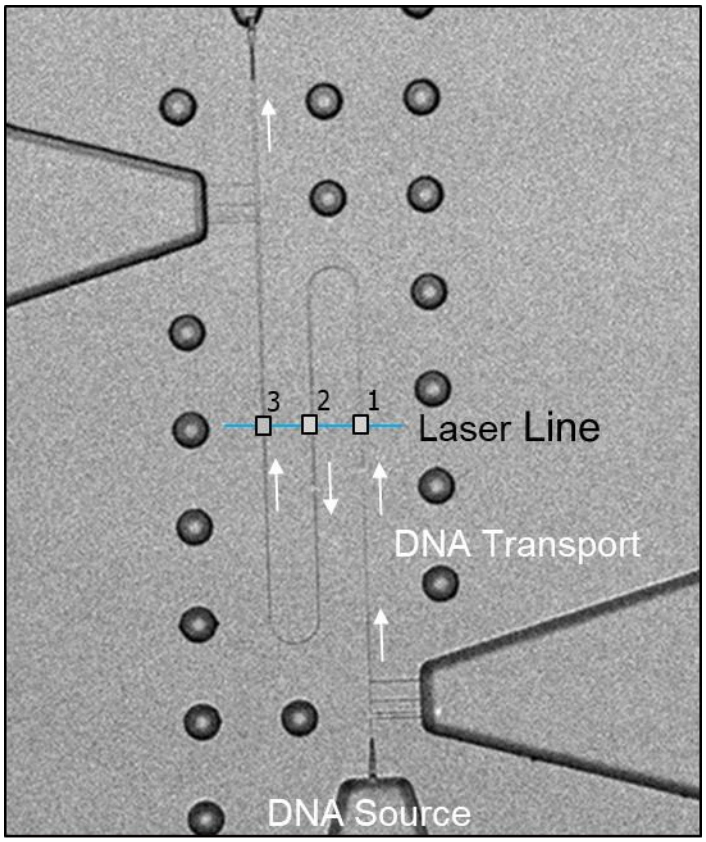

Figure 4.1: Schematic of DNA transport device. DNA is electrokinetically driven into the nanochannel where it passes through a laser line three times before exiting. Boxes 1,2, and 3 represent the three ROIs for data collection.

Laser-Induced Photodamage: Increase in Total Number of Fragments (%)

		Field Strength	
		52 V/cm	9 V/cm
Laser Power	0.9 mW	0.3%	92.0%
	0.5 mW	1.8%	38.0%
	0.2 mW	0.2%	25.0%

Table 4.1: The influence of laser power and electric field strength on DNA fragmentation during transport from ROI 1 to ROI 3. An increase in total fragment number was assumed to be due to laser-induced photocleavage of DNA molecules into smaller fragments.

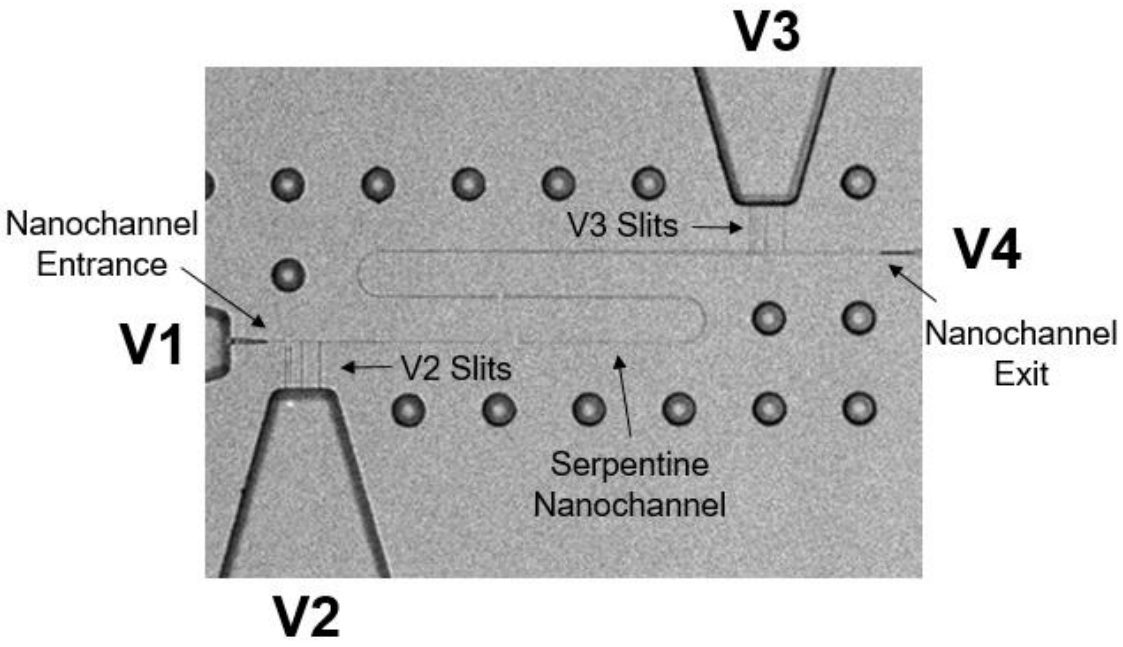

Figure 4.2: COP device nanochannel layout. A serpentine nanochannel connects V1, V2, V3, and V4 microchannel inlets. Slits at V2 and V3 aid in electrokinetic DNA injection. The following paths were measured in the conductivity control: V1-V2, V1-V3, V1-V4, V2-V3, V2-V4, V3-V4.

Expected Current from Conductivity Models

Path	Total R (MΩ)	Calculated Current (nA)	LTSpice Current (nA)
V1-V2	296	10.11	9.5
V1-V3	11,034	0.27	0.27
V1-V4	11,903	0.25	0.26
V2-V3	10,712	0.28	0.28
V2-V4	11,581	0.26	0.26
V3-V4	850	3.53	3.32

Table 4.2: Channel resistances and currents calculated using equations 1-3, and currents calculated by LTspice modeling program.

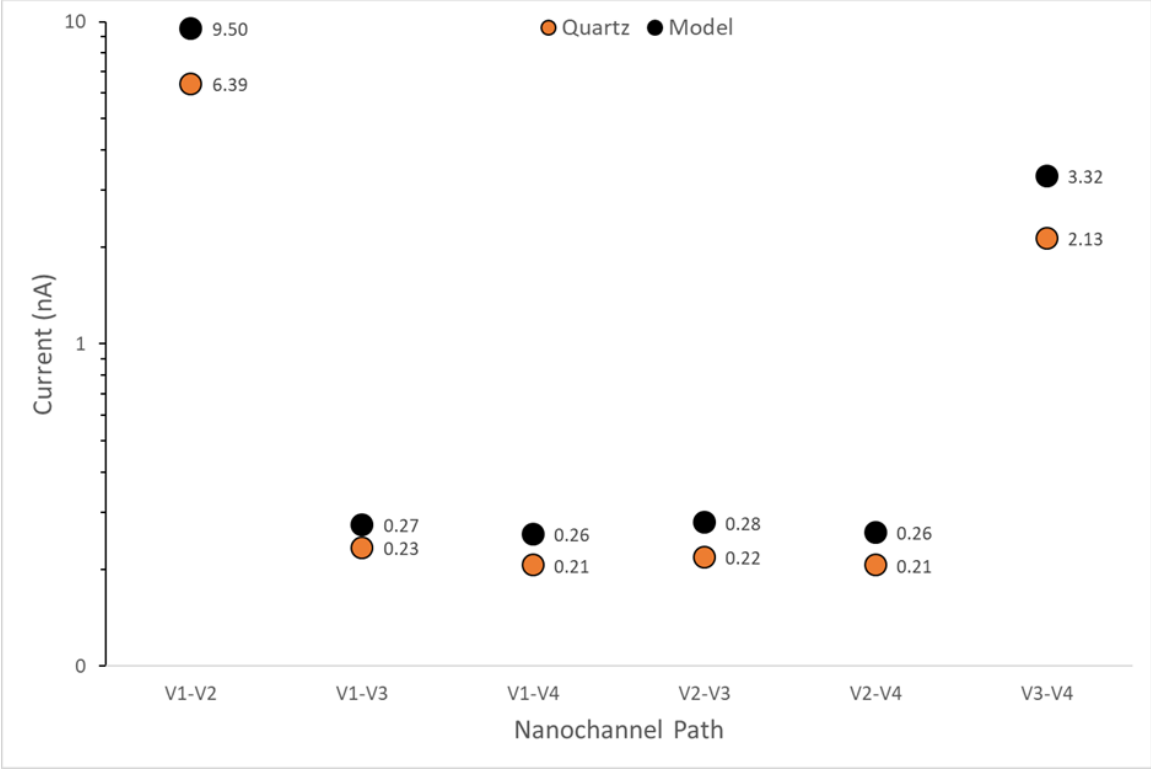

Figure 4.3: Measured current in quartz devices (⚬) vs. expected current from model (•). Y-axis plotted on log scale for data visualization purposes. Conductivity measurements were taken in passivation buffer.

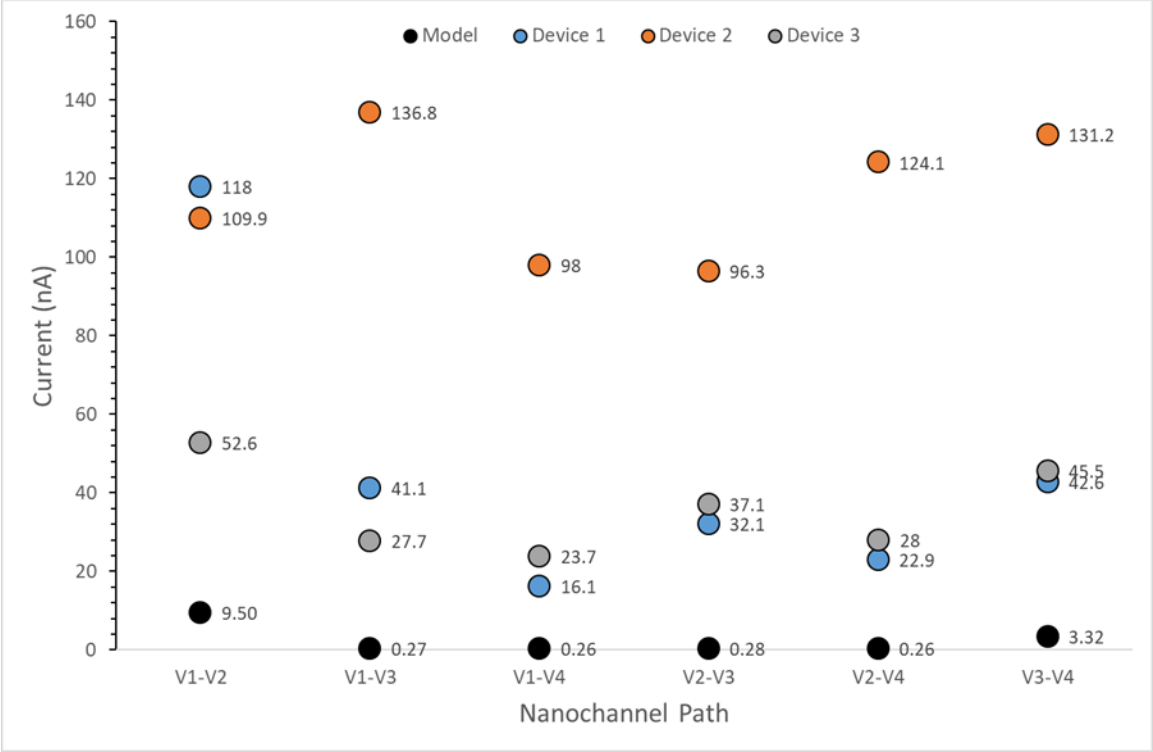

Figure 4.4: Current measurements of three devices pre-DNA transport experiments (●,●,●) compared to the expected current from the model (●).

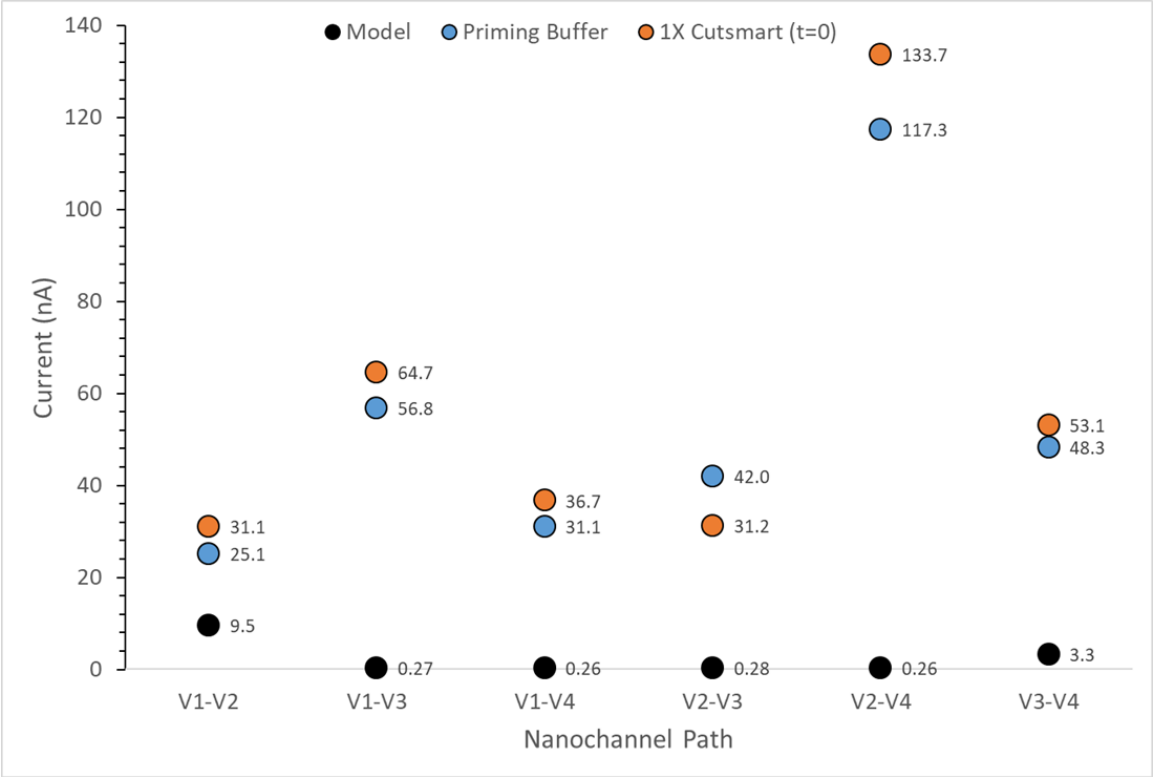

Figure 4.5: Comparison of expected current (●) and measured current with priming buffer (◉) or 1X Cutsmart buffer (◉) (no surfactants) in the microfluidic chip on Day 1.

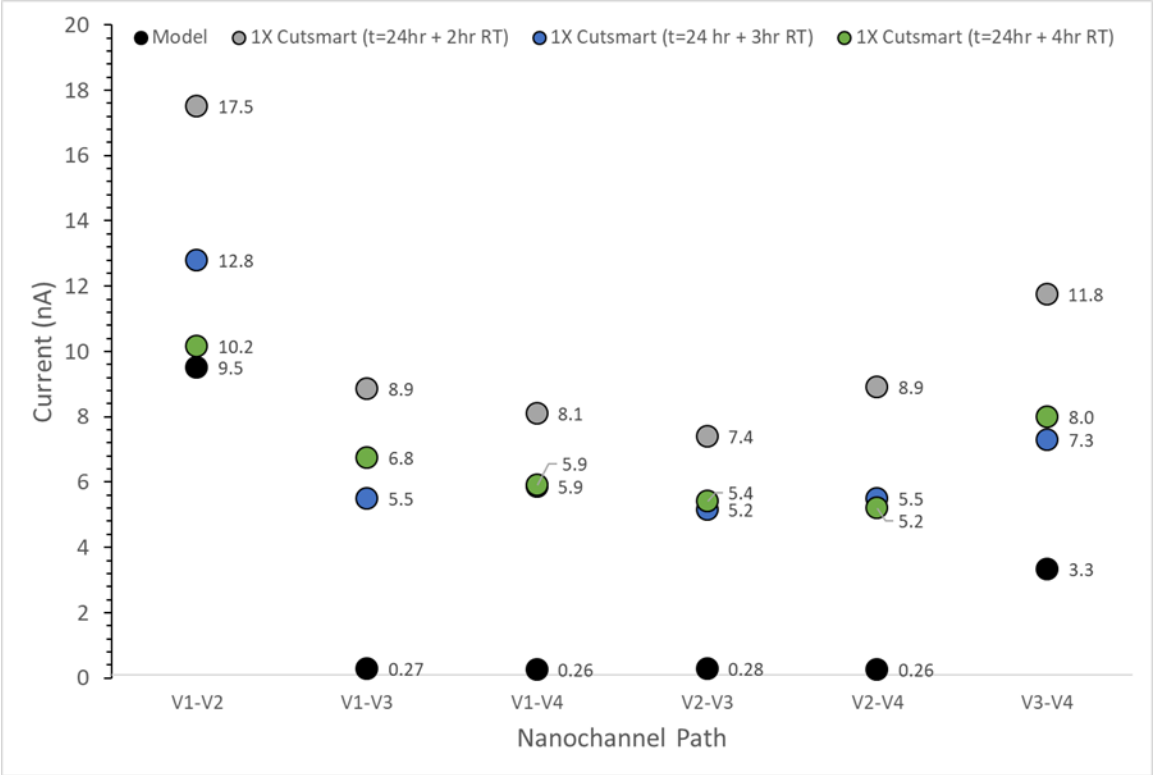

Figure 4.6: Comparison of expected current (•) and measured current with 1X Cutsmart buffer at t = 26 h (⊙), t = 27 h (⊙) and t = 28 h (⊙) after Day 1 current measurements in Figure 4.5. The microfluidic chip was left at 5 °C for 24 h then currents measured after 2, 3, and 4 h at room temperature.

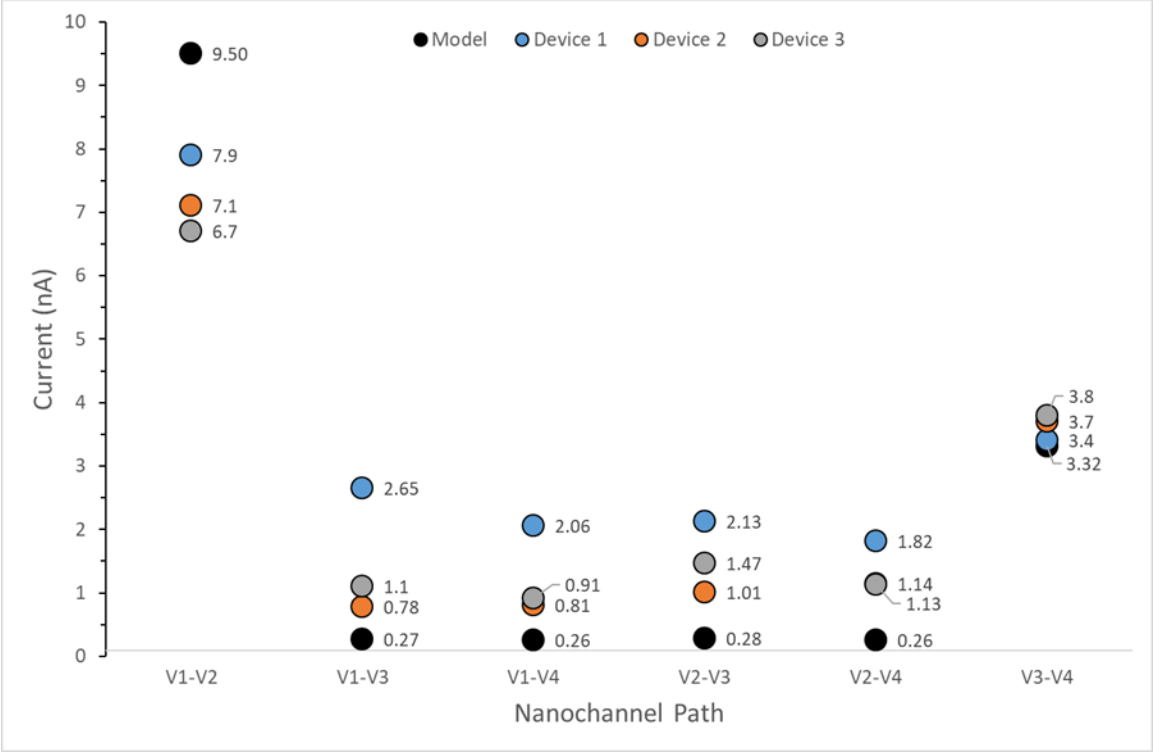

Figure 4.7: Comparison of experimental current measurements from three devices post-DNA transport (●,●,●) to the expected current from the model (●).

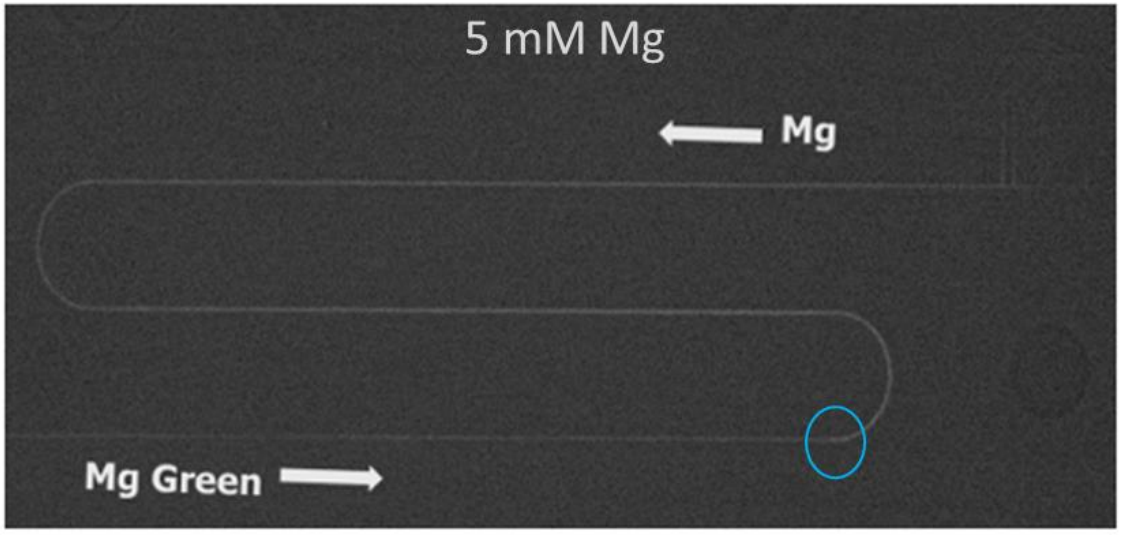

Figure 4.8: Complexed Mg-Mg Green fluorescence in the nanochannel at electrokinetic steady state averaged over 30 s. The blue circle encompasses the channel defect area revealed by an increase in channel dimension/fluorescence intensity.

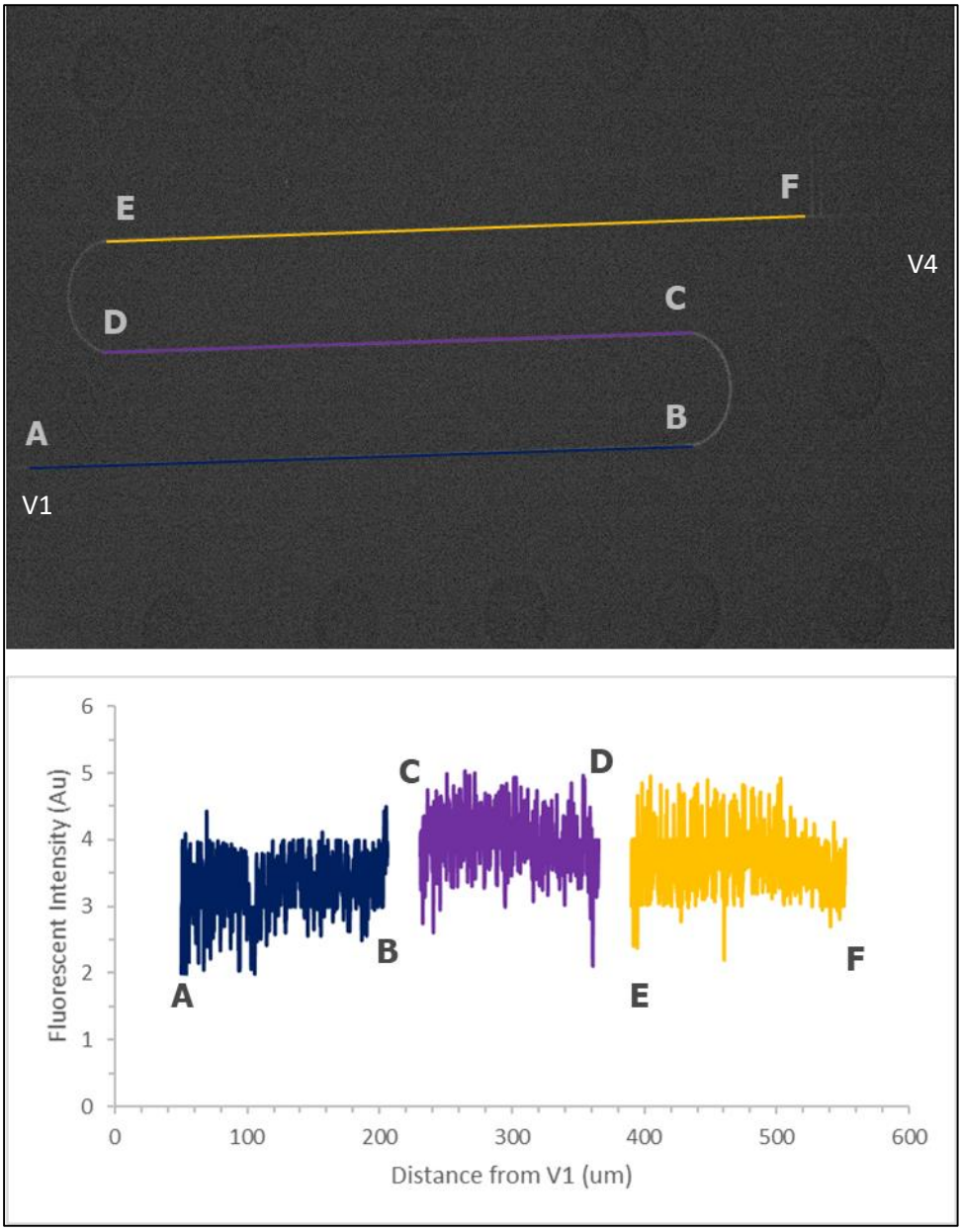

Figure 4.9: Line profiles of complexed Mg-Mg Green fluorescence average intensities in the serpentine nanochannel. Fairly consistent fluorescence was observed across the nanochannel.

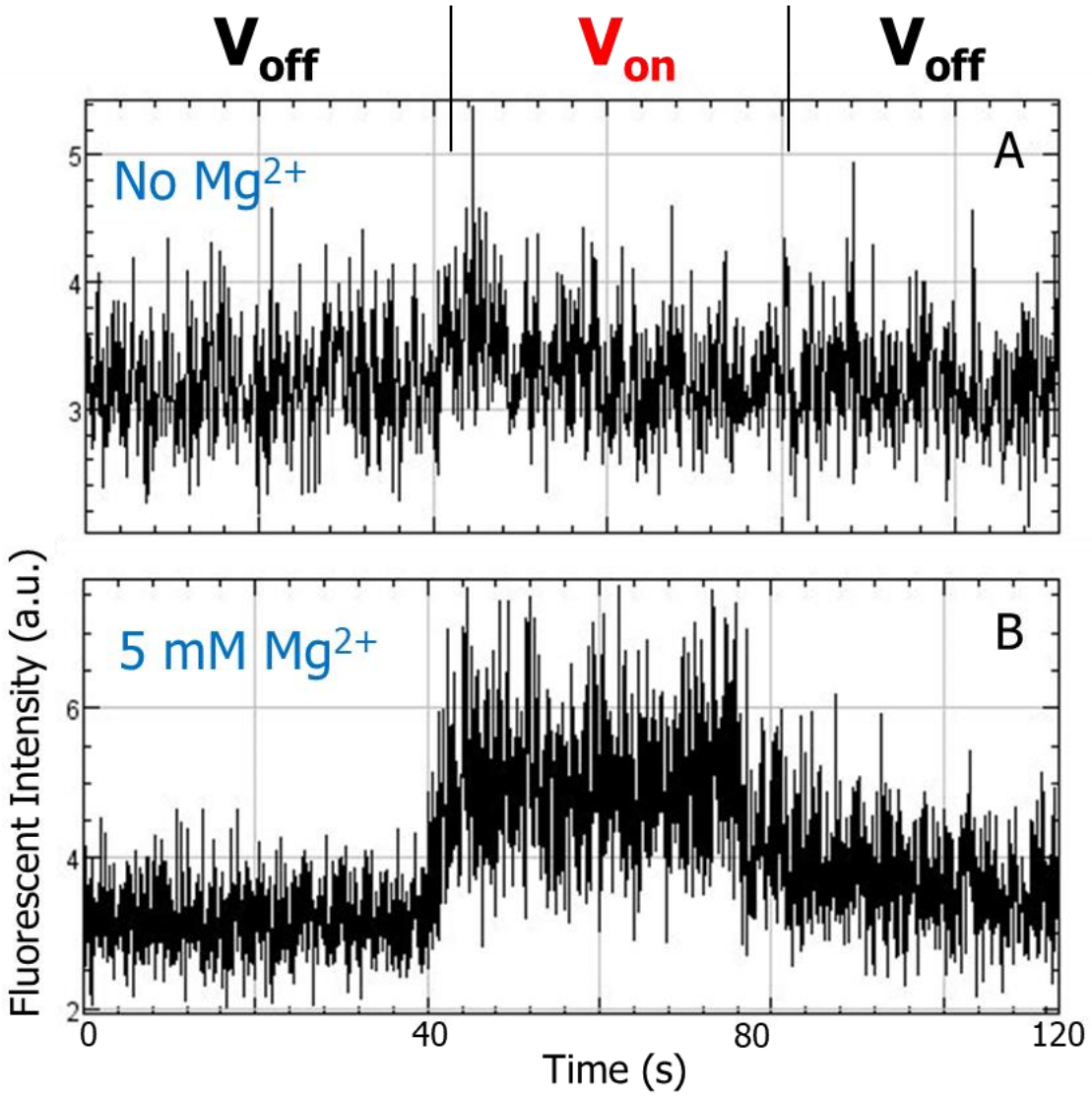

Figure 4.10: (A) Baseline fluorescence of Mg Green without Mg cations present. V_{off} / V_{on} delineate when the voltages were turned on to 52 V/cm to elicit electrokinetic transport of Mg Green into the nanochannel. There is very little fluorescent background due to Mg Green. (B) Fluorescence of the Mg Green with Mg cations present. Fluorescence increases as Mg-Mg Green complexes in the nanochannel during electrokinetic transport of the Mg cations.

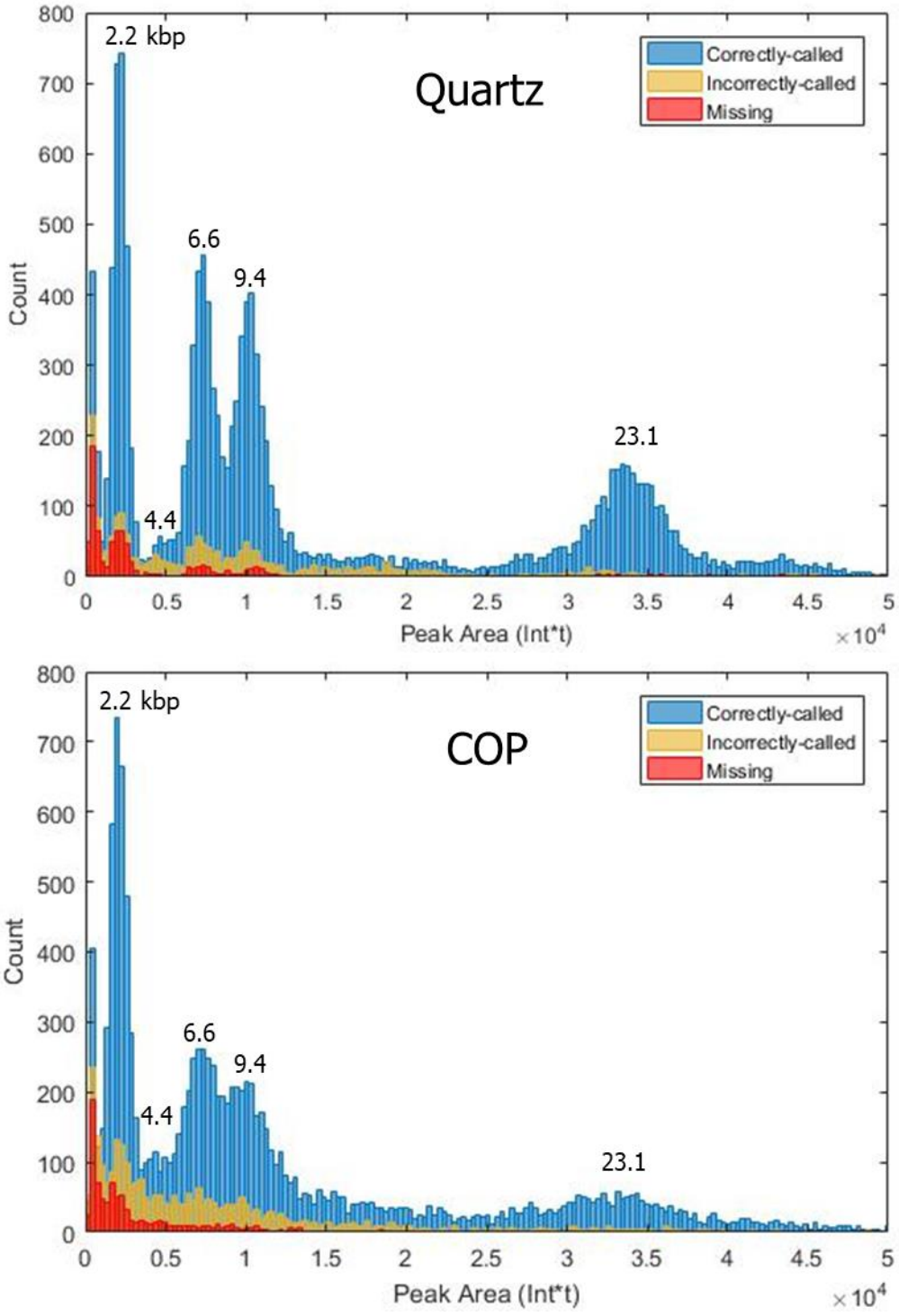

Figure 4.11: HindIII fragment size histograms in quartz and COP devices. The 5 major HindIII fragment populations are labelled.

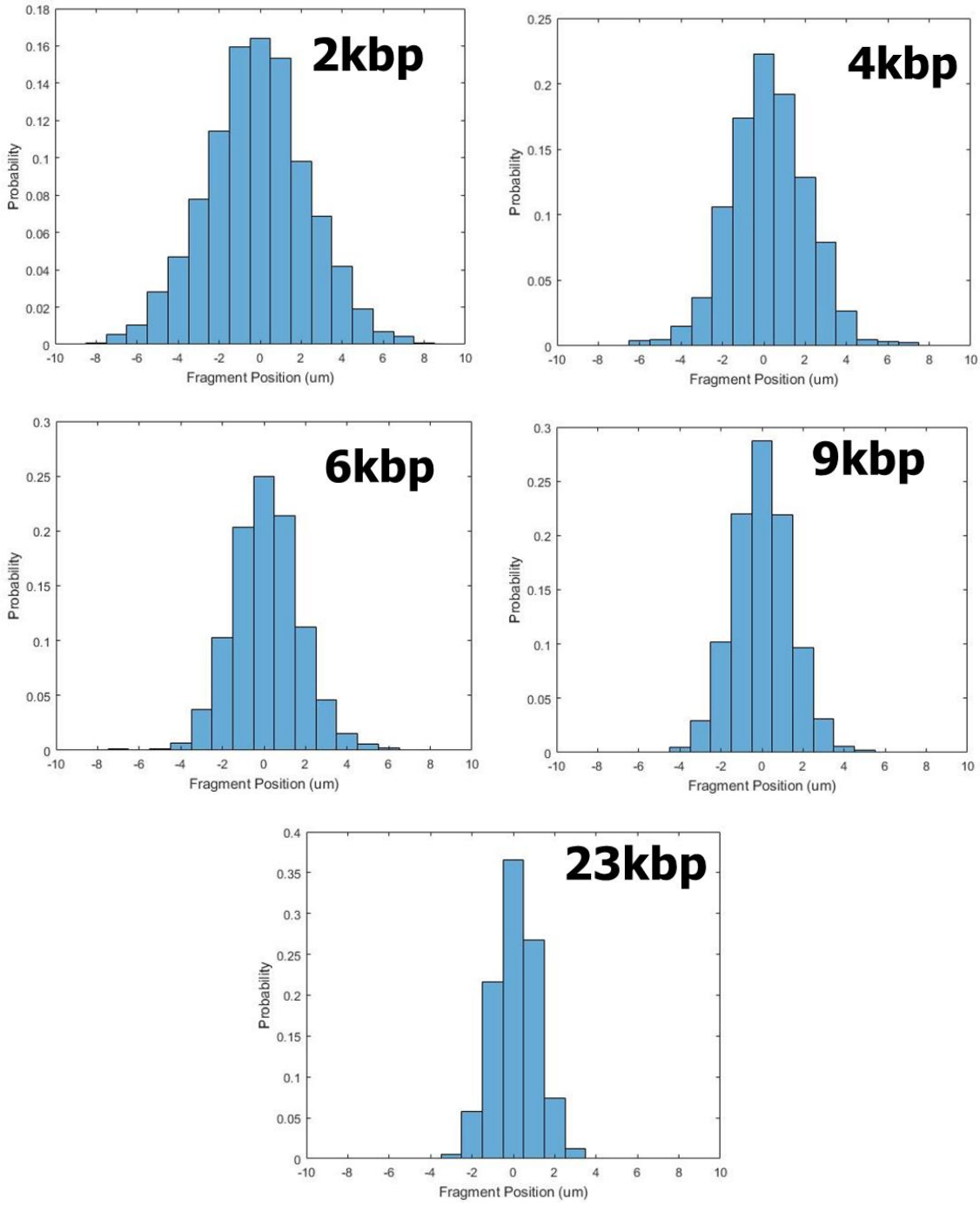

Figure 4.12: Fragment position probability after cross-correlation alignment for each HindIII fragment population.

Experiment vs. Rouse Diffusivity for HindIII Ladder Fragments

Basepairs	Contour Length (μm)	Experiment Diffusivity ($\mu m^2/s$)	Rouse Diffusivity ($\mu m^2/s$)
2,175	0.84	6.23	6.14
4,361	1.67	3.41	3.05
6,557	2.52	2.66	2.03
9,416	3.62	2.04	1.41
23,130	8.88	1.14	0.57

Table 4.3: Contour length, experiment diffusivity, and Rouse diffusivity for each HindIII fragment size.

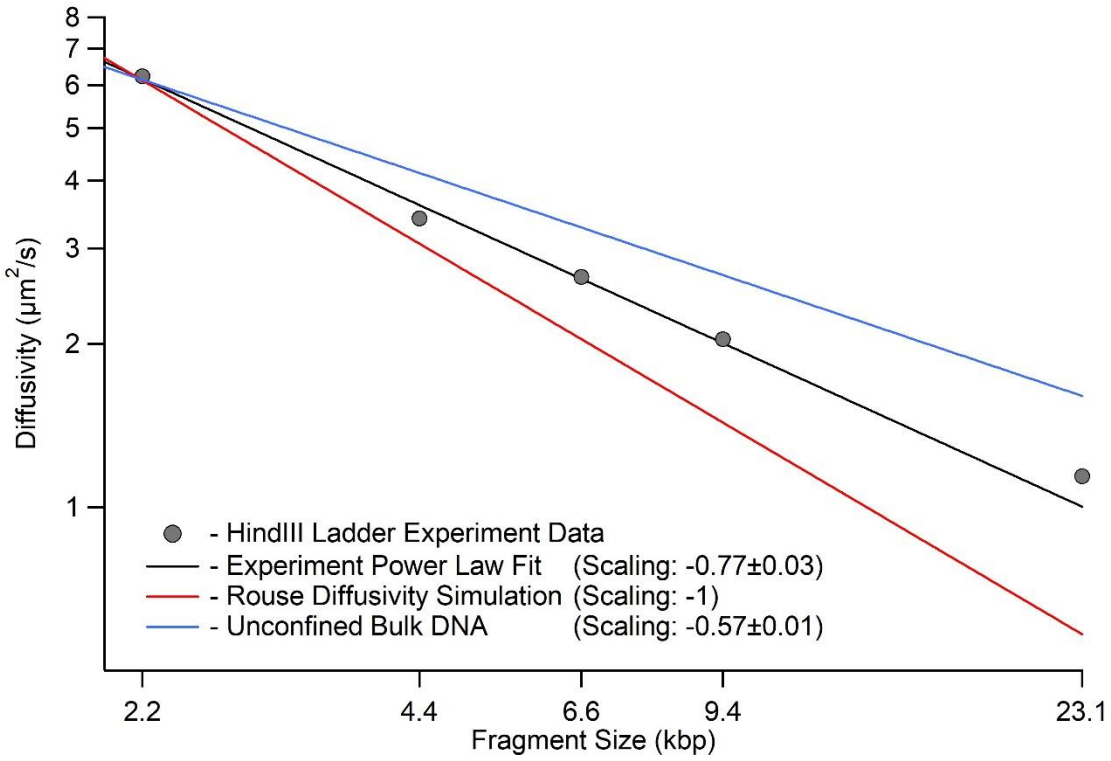

Figure 4.13: Log-log plot of the diffusivity of HindIII fragments. The scaling of the experimental data points is intermediate to that of Rouse diffusivity and unconfined DNA in bulk. The Rouse trace is an actual fit using the prefactors found in the cited simulation. Prefactors for unconfined bulk DNA were unavailable, therefore the values of the trace were arbitrarily placed for scaling visualization and should not be viewed as representative for fragment size.

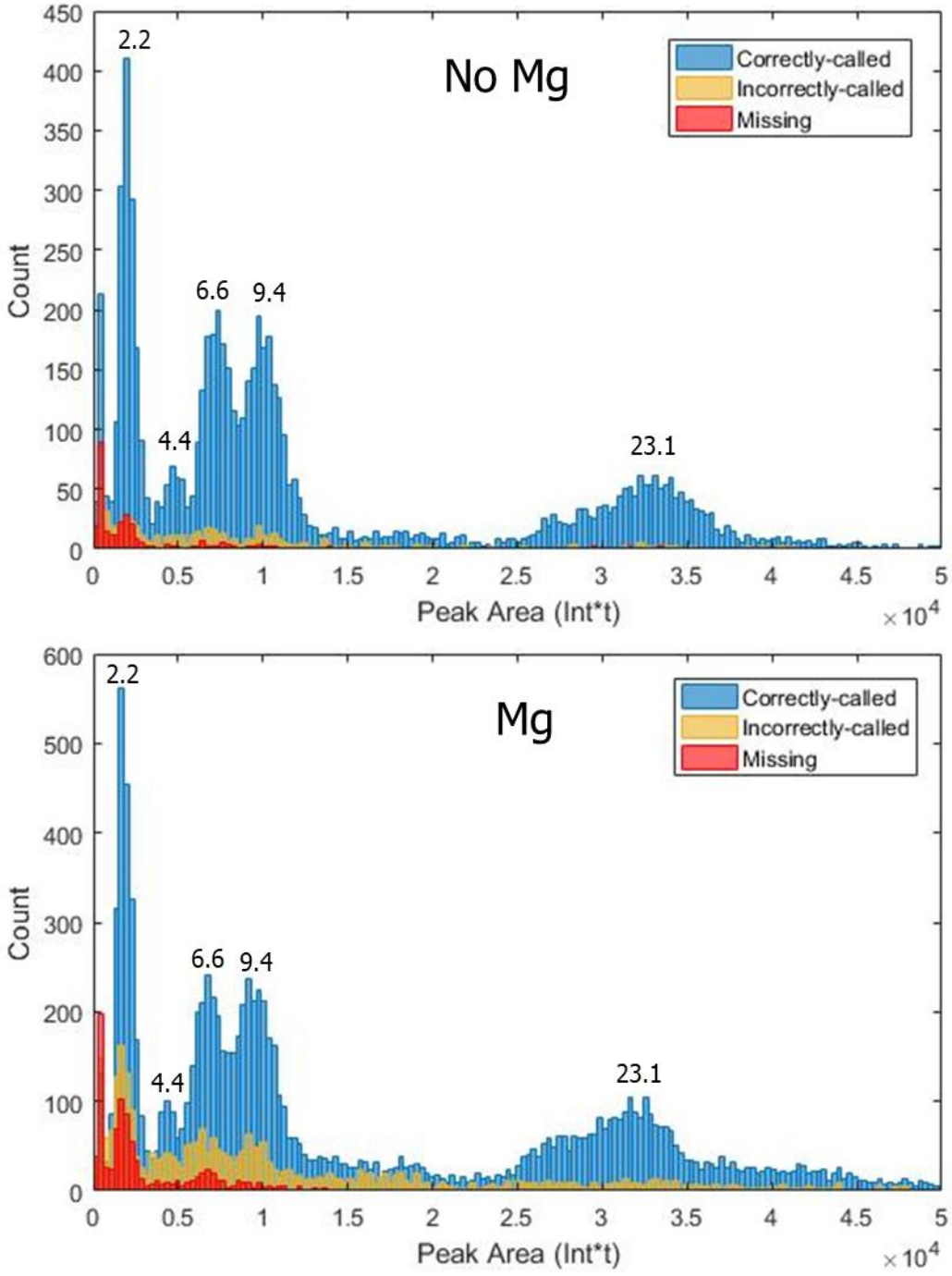

Figure 4.14: HindIII fragment size histograms for experiments with and without Mg cations. The inclusion of Mg increases the number of incorrectly-called and missing fragments for each fragment size.

DNA Transport Efficiency Comparison: Mg vs. No Mg

DNA Size (kbp)	No Mg M	No Mg IC	No Mg IT	Mg M	Mg IC	Mg IT
2.2	7%	9%	16%	13%	23%	36%
4.4	3%	10%	13%	8%	24%	23%
6.6	2%	5%	7%	6%	15%	12%
9.4	1%	6%	7%	3%	16%	13%

M	Missing Fragment %
IC	Incorrectly-called Fragment %
IT	Impacted Transport % (M+IC)

Table 4.4: Results for DNA transport experiments with and without Mg. Table representation of data found in Figure 4.14.

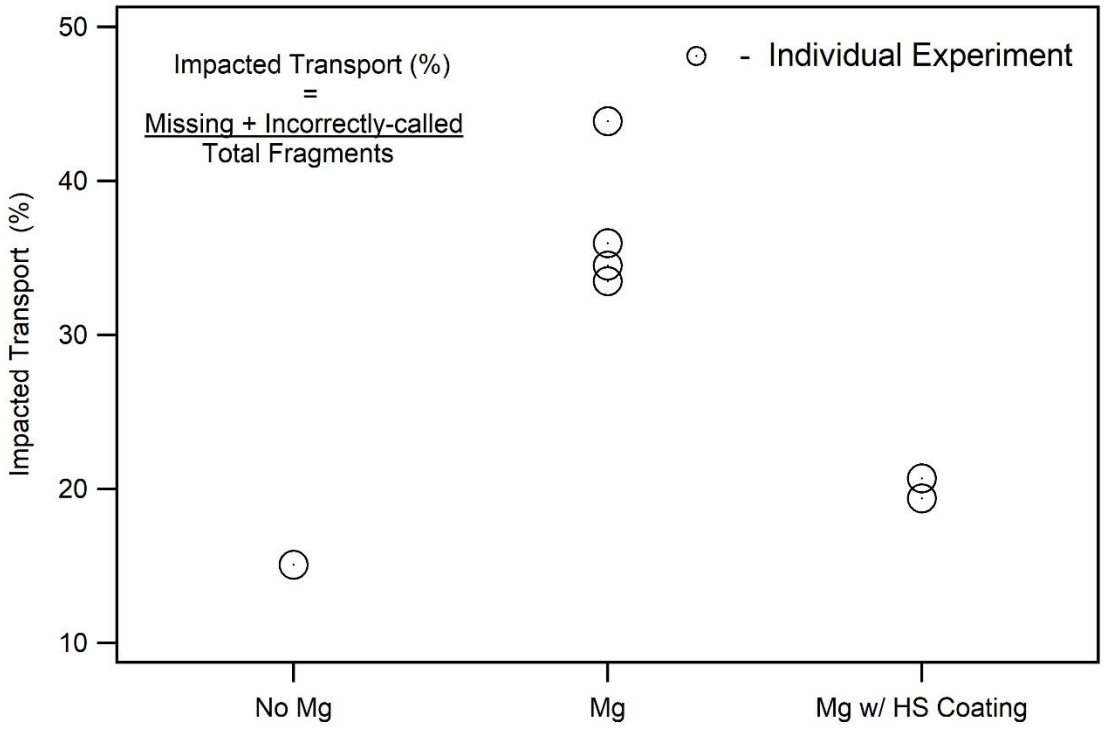

Figure 4.15: Percentage of fragments with impacted transport in No Mg, Mg, and Mg w/ HS coating experiments. Each data point is from an individual experiment and encompasses 5k-12k DNA fragments.

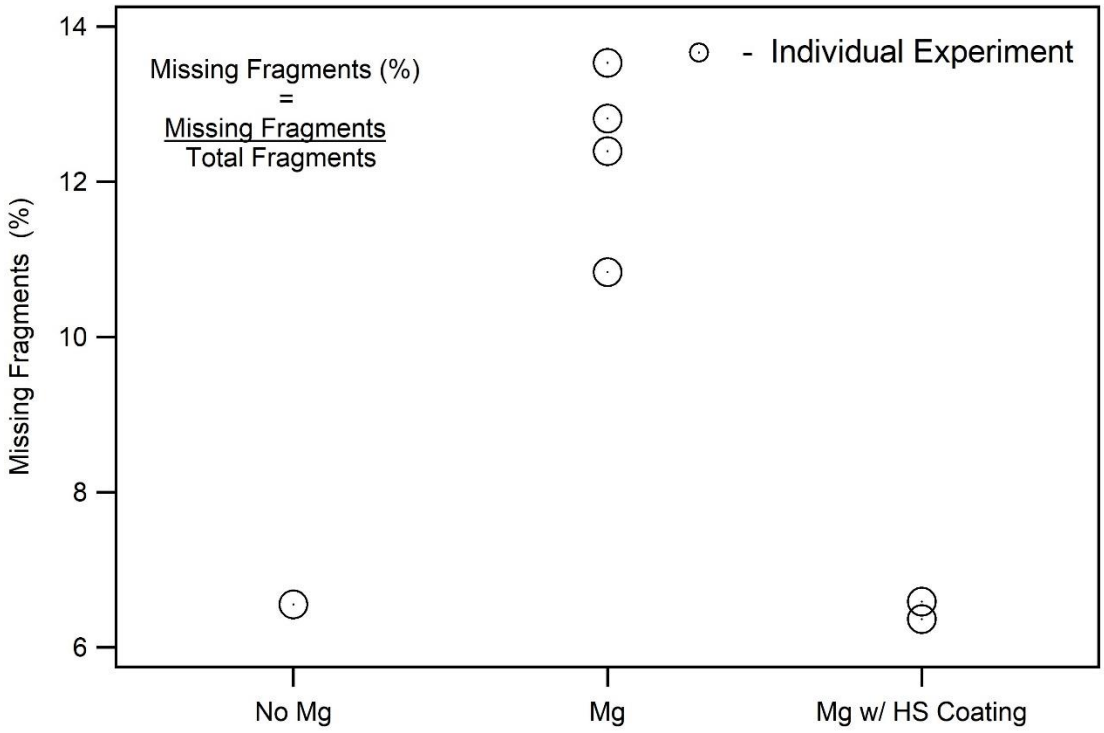

Figure 4.16: Percentage of missing fragments in No Mg, Mg, and Mg w/ HS coating experiments. Each data point is from an individual experiment and encompasses 5k-12k DNA fragments.

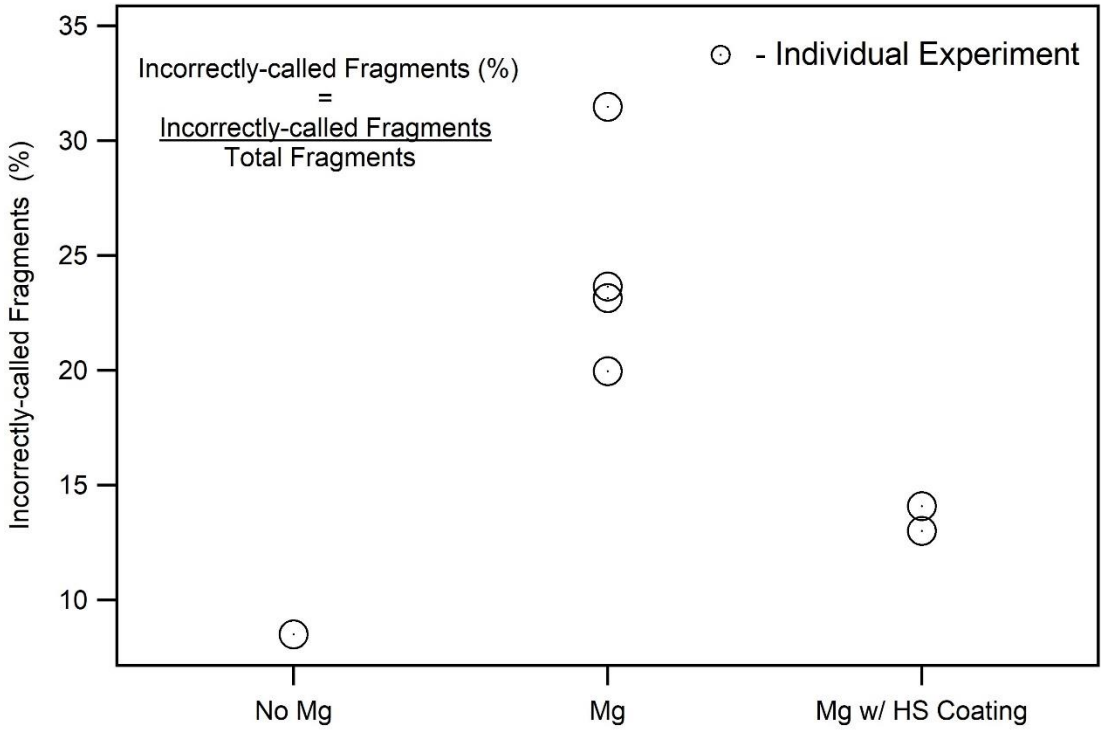

Figure 4.17: Percentage of incorrectly-called fragments in No Mg, Mg, and Mg w/ HS coating experiments. Each data point is from an individual experiment and encompasses 5k-12k DNA fragments.

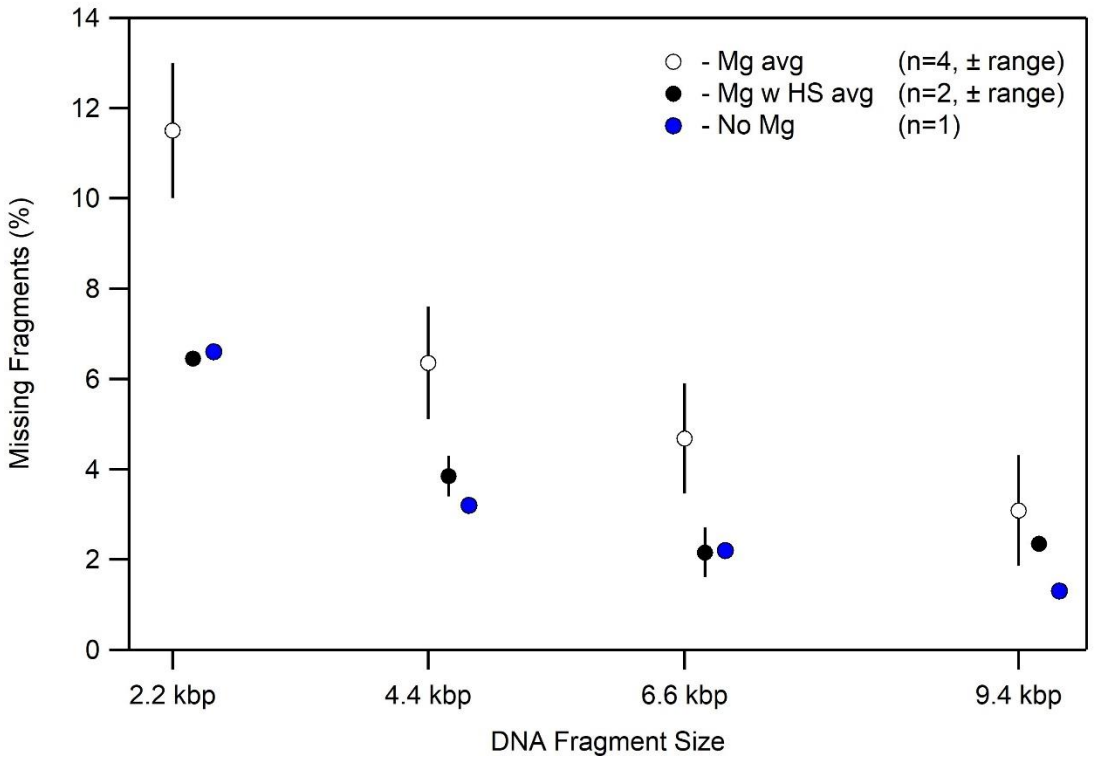

Figure 4.18: Percentage of missing fragments in No Mg, Mg, and Mg w/ HS coating experiments for each HindIII fragment size. A size-dependence is observed.

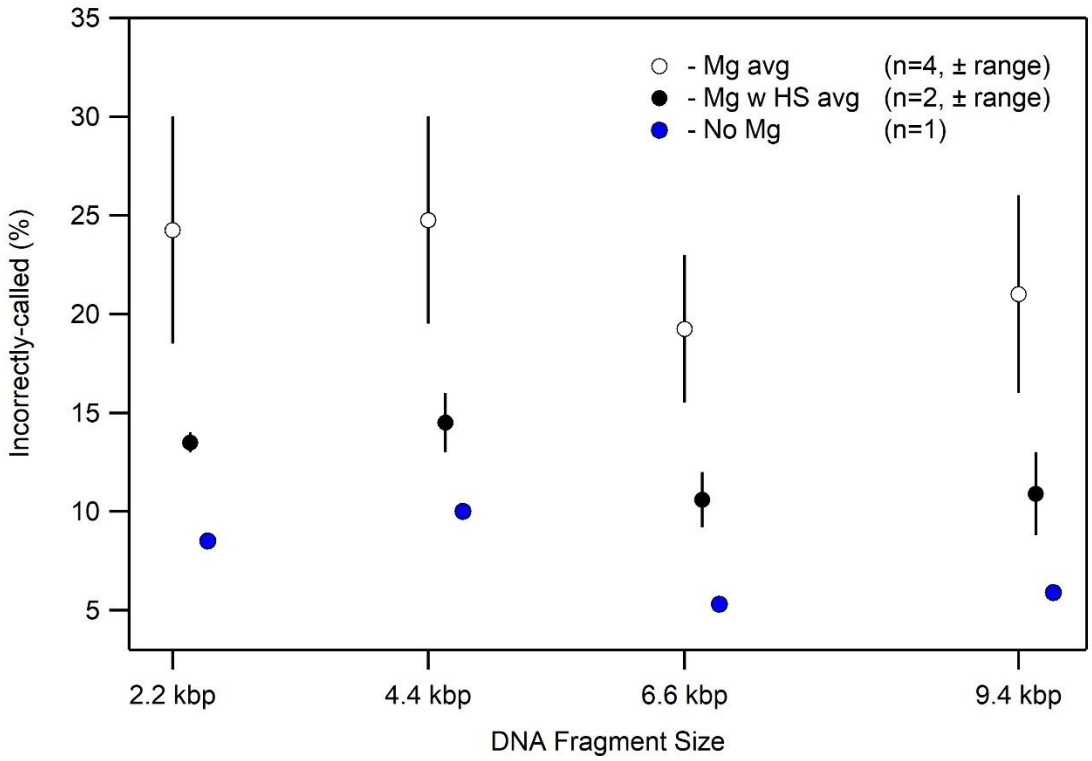

Figure 4.19: Percentage of incorrectly-called fragments in No Mg, Mg, and Mg w/ HS coating experiments for each HindIII fragment size. Unlike Figure 4.18, no size-dependence is observed.

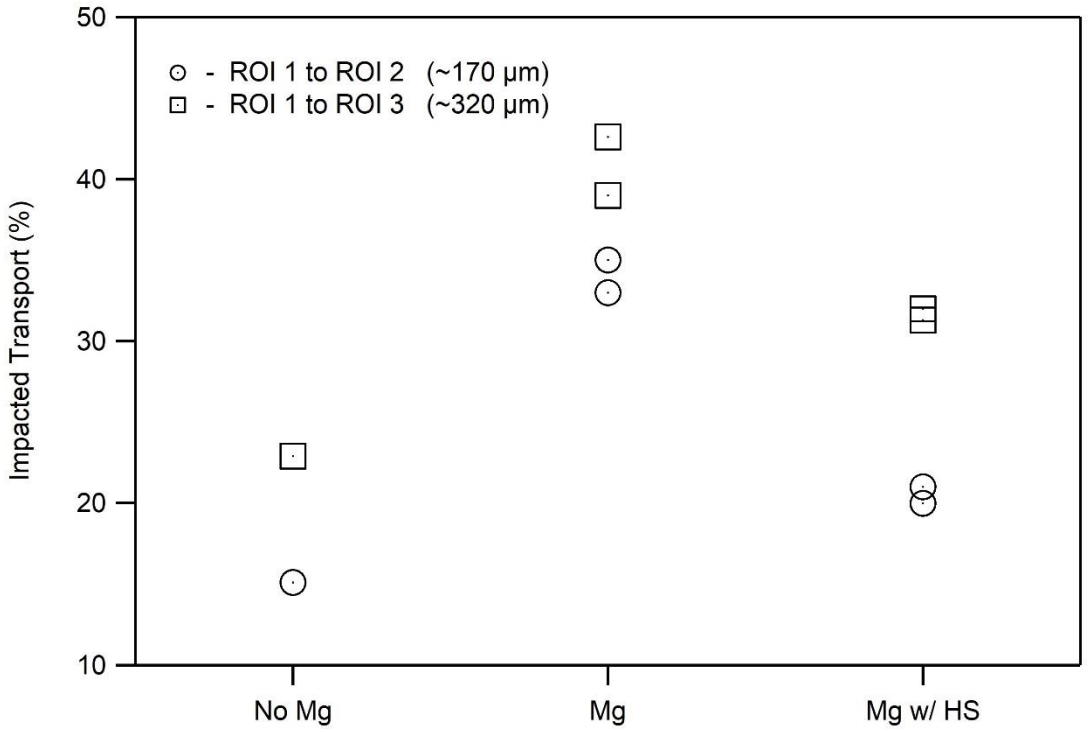

Figure 4.20: Percentage of fragments with impacted transport for No Mg, Mg, and Mg w/ HS experiments. Longer paths (square symbol) universally causes a higher percentage of impacted transport fragments.

REFERENCES

1. Yameen, B. *et al.* Synthetic proton-gated ion channels via single solid-state nanochannels modified with responsive polymer brushes. *Nano Lett* **9**, 2788-2793 (2009).

2. Frank, M., Drikakis, D. & Asproulis, N. Thermal conductivity of nanofluid in nanochannels. *Microfluidics and Nanofluidics* **19**, 1011-1017 (2015).

3. Tsutsui, M. *et al.* Transverse electric field dragging of DNA in a nanochannel. *Sci Rep* **2**, 394 (2012).

4. Ramsey, J. M. & Menard, L. Nanofluidic devices for the rapid mapping of whole genomes and related systems and methods of analysis. (2016). Patent.

5. Menard, L. D. & Ramsey, J. M. Nanofluidic devices with integrated components for the controlled capture, trapping, and transport of macromolecules and related methods of analysis. (2013). Patent.

6. Menard, L. D., Ramsey, J. M., McCrate, O. A. & Tycon, M. A. Fluidic devices with nanoscale manifolds for molecular transport, related systems and methods of analysis. (2015). Patent.

7. Menard, L. D. & Ramsey, J. M. The fabrication of sub-5-nm nanochannels in insulating substrates using focused ion beam milling. *Nano Lett.* **11**, 512-517 (2011).

8. *FAQ: Why does my Lambda DNA molecular weight marker appear smeared and not represent the correct banding pattern?*, <https://www.neb.com/faqs/0001/01/01/why-does-my-lambda-dna-molecular-weight-marker-appear-smeared-and-not-represent-the-correct-bandi> Web. Accessed 6/17/19.

9. Gupta, D., Bhandari, A. B. & Dorfman, K. D. Evaluation of Blob Theory for the Diffusion of DNA in Nanochannels. *Macromolecules* **51**, 1748-1755 (2018).

10. Dai, L., Tree, D. R., van der Maarel, J. R., Dorfman, K. D. & Doyle, P. S. Revisiting blob theory for DNA diffusivity in slitlike confinement. *Phys Rev Lett* **110**, 168105 (2013).

11. Chen, Y. L. *et al.* Conformation and dynamics of single DNA molecules in parallel-plate slit microchannels. *Phys. Rev. E* **70**, 060901 (2004).

12. Balducci, A., Mao, P., Han, J. Y. & Doyle, P. S. Double-stranded DNA diffusion in slitlike nanochannels. *Macromolecules* **39**, 6273-6281 (2006).

13. Brochard, F. & de Gennes, P. G. Dynamics of confined polymer chains. *J. Chem. Phys.* **67**, 52-56 (1977).

14. Muralidhar, A. & Dorfman, K. D. Kirkwood diffusivity of long semiflexible chains in nanochannel confinement. *Macromolecules* **48**, 2829-2839 (2015).

15. Reccius, C. H., Stavis, S. M., Mannion, J. T., Walker, L. P. & Craighead, H. G. Conformation, Length, and Speed Measurements of Electrodynamically Stretched DNA in Nanochannels. *Biophys. J.* **95**, 273-286 (2008).

16. Robertson, R. M., Laib, S. & Smith, D. E. Diffusion of isolated DNA molecules: dependence on length and topology. *Proc Natl Acad Sci U S A* **103**, 7310-7314 (2006).

17. Sinden, R. R. *DNA Structure and Function*. Print. (1994).

18. Gupta, D. *et al.* Mixed confinement regimes during equilibrium confinement spectroscopy of DNA. *J. Chem. Phys.* **140**, 214901 (2014).

19. Fernandes, M. X., Ortega, A., Lopez Martinez, M. C. & Garcia de la Torre, J. Calculation of hydrodynamic properties of small nucleic acids from their atomic structure. *Nucleic Acids Res* **30**, 1782-1788 (2002).

20. Sissi, C. & Palumbo, M. Effects of magnesium and related divalent metal ions in topoisomerase structure and function. *Nucleic Acids Res* **37**, 702-711 (2009).

21. Riehn, R. *et al.* Restriction mapping in nanofluidic devices. *Proc Natl Acad Sci U S A* **102**, 10012-10016 (2005).

22. Mela, P. *et al.* The zeta potential of cyclo-olefin polymer microchannels and its effects on insulative (electrodeless) dielectrophoresis particle trapping devices. *Electrophoresis* **26**, 1792-1799 (2005).

23. Belotserkovskii, B. P. & Johnston, B. H. Denaturation and association of DNA sequences by certain polypropylene surfaces. *Anal Biochem* **251**, 251-262 (1997).

24. Svinarchuk, F., Bertrand, J. R. & Malvy, C. A short purine oligonucleotide forms a highly stable triple helix with the promoter of the murine c-pim-1 proto-oncogene. *Nucleic Acids Res* **22**, 3742-3747 (1994).

25. Budker, V. G., Godovikov, A. A., Naumova, L. P. & Slepneva, I. A. Interaction of polynucleotides with natural and model membranes. *Nucleic Acids Res* **8**, 2499-2515 (1980).

CHAPTER 5: SINGLE CELL CAPTURE DEVICE FOR ANALYSIS OF WHOLE GENOMES

5.1 – Introduction

The advent of next generation sequencing techniques has accelerated the potential for personalized healthcare.[1-4] Isolation of patient cells and subsequent DNA extraction is of particular interest to clinicians and researchers interested in single cell omics. Which leads to the question, how can we capture and isolate DNA from individual cells? Extraction of entire genomes has been demonstrated in macroscale with spin columns and bio-functionalized magnetic microparticles. However, these techniques have serious disadvantages. Genomic material is often lost during purification and sample prep, which can be detrimental to the analysis of rare cell populations.[5,6] Moreover, comparative analysis of single cells is not possible. Microfluidic cell capture platforms have been developed to rectify these issues by providing closed systems for cellular trapping and DNA extraction. However, significant challenges still exist to compartmentalizing single cells and manipulating vast amounts of extracted DNA for downstream analyses.

Microfluidic platforms for cell capture and subsequent DNA extraction are well published[7-12] and patented.[13-20] Many of these platforms isolate DNA for PCR techniques, where careful handling of long DNA strands is of lesser importance. However, minimizing DNA shear risk is critical for genomic analysis of mapping and other long-read sequencing applications.[6,13] In juxtaposition with cellular extraction for PCR methods, the manipulation of long, unsheared DNA for mapping and sequencing applications has been relatively unexplored. The laminar flow and subsequent low shear forces on DNA in microfluidics is particularly advantageous in this application, posing an advantage over DNA-damaging macroscale extraction techniques. Two main archetypes of cell extraction occur – by mechanical cell shearing or chemical lysis. Chemical lysis methods are better suited for extraction techniques that rely on undamaged genomes as mechanical cell shearing methods can naturally result in large degrees of DNA shearing.[6] The serine protease Proteinase K and detergents like Triton X-100 are used in a variety of chemical lysis solutions to disrupt cell lipid membranes and extract genetic material.[21,22] In addition,

Proteinase K denatures the histones responsible for tight coiling of DNA; therefore, extracted DNA is free to diffuse unconfined.[23] Extracted genomes resembled a cloud of loosely-tangled DNA strands in preliminary cell extraction experiments in the Ramsey lab. In addition, the vast amount of extracted DNA can be difficult to handle using hydrodynamics or electrophoretic methods, and exists as an obstacle for any single cell capture method.

Microfluidic platforms for cell capture and chemical lysis have been demonstrated in the past. For example, *Craighead et al.* developed a device design and method comprised of micropillars spatially configured to capture cells by size exclusion. DNA from chemically-lysed cells were immobilized and maintained in elongated form by the use of hydrodynamic forces in microfluidic channels.[8] Ideally DNA could be released from the pillars and flow downstream for further analysis. Determining the best way to manipulate extracted DNA is critical to the single cell capture application and would be valuable if demonstrated and reduced to practice.

This chapter explores the design, development, and testing of a device capable of compartmentalized single cell capture. The device described here was successful in capturing and lysing individual cells, but was not able to suitably manipulate the entire genomes released during cell lysis. Subsequently, downstream analysis of compartmentalized genetic material was not explored, but nonetheless exists as an area of future work.

5.2 – Experimental

5.2.1 – Device Design

The single cell capture device for cell-specific genomic analysis was designed around capturing single cells over an array of capture regions. The designed platform includes individual cell capture regions where individual cells will be trapped, chemically lysed, and compartmentalized for downstream DNA analysis. Figure 5.1 illustrates the design of the device and features two main components. Three microfluidic channels (approximately 100 μm wide, 30 μm deep) are connected by a series of interlinked microchannels an order of magnitude smaller in size (5.5 μm wide, 2 μm deep). Each microfluidic channel features a via located at positions (1), (2) and (3) to enable head pressure driven flow for cell transport and buffer exchange. The interlinked microchannels (Fig 5.1B), dubbed the harpsichord due to their shape, are of different lengths and integrate wider microchannels in series. The purpose of each integrated microchannel is to 'gate' genomic material based on either the length of time it would take to electrokinetically transport through the channel (longer channel = increased transport time). The wider microchannel sections (Figure 5.3C) in the harpsichord were included to increase DNA transport time through that section. Each channel in the harpsichord features a cell capture region at the large microfluidic channel/harpsichord interface large enough for one individual cell. The idea beHind this design is to capture a single cell in each capture region, lyse the cell to release genomic material, compartmentalize the genomic material in the cell's respective channel, and time gate the genomic material based on the differing microchannel lengths and the time it would take to electrokinetically transport through the harpsichord. The fluidic device design was modelled with COMSOL to determine the magnitude of flows expected and is shown in Figure 5.2 for three individual capture regions. Once a cell is captured in the capture region it would physically block the entrance to the smaller microchannel and block flow at the capture region / microchannel interface. This inhibits additional cells from being captured in the same region. Figure 5.2 shows the expected flows of a device in operation with head pressures of -100 mBar at (1) and -500 mBar at (3). The resulting flow in the cell transport microchannel (burgundy) is approximately 1 mm/s, while the flow velocity in the capture region is close to 0.1 mm/s, verifying that cells the capture regions will not be subjected to bulk microchannel flow upon capture.

5.2.2 – Device Fabrication

The single cell capture devices were created from quartz substrates (Telic Company) precoated with 120 nm and 530 nm of chromium and AZ1500 photoresist, respectively. Direct-write photolithography was performed with a Heidelberg Instruments DWL 66FS laser writer. The first of two photolithography steps created the large cell transport microchannels in the photoresist, which was then developed for 1 min with AZ400K 3:1 developer (AZ Electronics Materials). Next, the Cr layer was etched with Cr etchant (Chromium Etchant 1020, Transene Corp.) for 3 minutes with sonication to reveal the quartz. The microchannels were created by use of a 5:1 buffered oxide etch (Transene Corp) for 156 min. The substrate was rinsed and dried under nitrogen post buffered oxide etch. The second photolithography step patterns the smaller DNA transport microchannels or harpsichord features. Fiducial marks on the quartz substrate were used to enable nearly perfect overlap of successive development with the first etched microchannels. The procedure for creating the harpsichord microchannels was identical to the first procedure, except for the buffered oxide etch which was performed for approximately 13 min instead of 156 min. Once both sets of microchannels were etched the remaining photoresist and Cr were removed with AZ400K and Cr etchant, respectively. Vias were powder blasted into the devices to create entrances to the fluidic channels. The device was then placed in 2X Nanostrip (KMG Chemicals) with 130 μm quartz coverslips (Esco Optics) for 24 h to remove organic contaminants. Finally, the devices and coverslips were thermally bonded at 1000 °C to create sealed fluidic channels.[24] Figure 5.3 shows the bonded cell transport microfluidic channel - harpsichord region and critical dimensions of the cell capture feature and harpsichord microchannels. Important to notice here is the buffered oxide etch is an isotropic etch process, therefore sharp corners are rounded out.

5.2.3 – Buffer and Cell Preparation

Three different cell lines were utilized in preliminary experiments: Primary colon cells, K562 cells, and Kasumi-3 cells. All cells were obtained from the lab of Nancy Allbritton and are nonadherent cell lines. Cells were passaged the day of experiment into 1X PBS at 30 °C. Cells were then rinsed with 1X PBS and centrifuged at 0.8 RPM. Three rinse and centrifuge steps were used to isolate the cells from media and debris. Once the cells were ready for staining, 2 μL YOYO-1 or SYTO-16 was added to the cells in PBS. The resulting solution was gently mixed until the dye was no longer visible. Gentle mixing

at this step was vital to minimizing cell death and subsequent cell debris. Afterwards, the cells were kept on ice for 1 h for staining.

A buffer solution containing Triton X-100 and Proteinase K was used to lyse the cells. The cell lysis solution was comprised of the following components:

250 µL of heat-treated PBS

50 µL of 10% Triton X-100 in nuclease free water

50 µL 0.5 M EDTA

0.5 µL Dithiothreitol

100 µL Proteinase K

5.2.4 – Experiment Protocol

Each experiment started with a new dry quartz device. Devices were wet with heat-treated 1X PBS an hour before the experiment. The devices were wet according to the following protocol:

1. Add 50 µL 1X PBS to (3) via
2. Pull house vacuum at (1) and (2) in parallel for 1 min
3. Inspect to make sure entire harpsichord geometry is wet
4. Add 50 µL 1X PBS to (2) via
5. Pull house vacuum at (1) for 30 s
6. Inspect to see that (2)-(1) microchannel is wet and free of bubbles
7. Add 50 µL 1X PBS to (1) via
8. Let sit for 1 h

The aforementioned order of wetting (3) – (2) – (1) was important to ensure even device wetting and to minimize bubbles in the harpsichord geometry.

A combination of head pressure and house vacuum were used to generate bulk flow and subsequent cell capture. The wetting PBS was aspirated and 50 µL of cell buffer solution was pipetted into via (1), 25 µL of 1X PBS was pipetted into via (2), and 10 µL of 1X PBS was pipetted into via (3). The head pressure difference between (1), (2), and (3) was not enough to elicit cell capture in the capture regions, so house vacuum (-542 mBar) was added at (3). In this way cells travelling from (1) to (2) were

pulled into the capture regions. If more than one cell was captured in an individual capture region vacuum could be briefly added to (2) to dislodge captured cells and reset the device. Figure 5.4 shows the pressure-induced capture of three cells with the brightfield image showing what appears to be captured cells in region 1, 3, and 4, with potential debris captured alongside 4. The fluorescence of DNA stained with Syto-16 (Figure 5.4B) verifies the captured cells in 1, 3, and 4, and in addition shows a small amount of genetic material captured at region 2. Figure 5.4 highlights two things: that single cell capture is possible, and that additional solution cleaning steps need to be implemented to minimize debris in the system.

Once approximately 5 cells had been captured, the cell lysis step was started. 50 µL of cell lysis solution was added to the 25 µL of 1X PBS solution at via (2). The increase in buffer volume at (2) reversed the flow direction. Pressure gradients caused transport of lysis solution through the cell transport microchannel where it comes into contact with captured cells at the harpsichord geometry. Platinum electrodes were inserted into vias (2) and (3) to enable electrokinetic transport of extracted DNA into the harpsichord geometry. A 5 V potential was used for this purpose. Gating of capture region-dependent genetic material was expected based on the different lengths of the individual microchannels in the harpsichord with DNA in the shorter channels expected to enter the cell transport microchannel (3) first.

5.3 – Results and Conclusions

Figure 5.4 shows that capture of single cells is possible with the aforementioned device design. The success of cell lysis is also demonstrated in Figure 5.5, which shows lysis of a cell over the course of approximately 32 s. In this figure, the blue arrow points to a captured Kasumi-3 cell. The cell is lysed over the period of 30 s, visible by the change in cell shape from A-D. This particular experiment utilized a SYTO-16 stain. The bracket in Figure 5.5D shows the DNA expanding into the DNA transport microchannel. The fluorescent intensity appears to drop as DNA is no longer confined to the cell and the overall density of DNA decreases. Lysis of captured cells was immediate (< 5 minutes after lysis solution addition) in all experiments tested. Important to note, as there were still cells located in the cell transport microchannels (1) and (2) when the cell lysis solution was added; there is a vast amount of extracted DNA that exists in the cell transport microchannel.

It is unclear if the captured cells' lysed DNA entered the DNA transport microchannels due to hydrodynamic or electrokinetic forces. Moreover, controlling extracted genomes with precision was difficult. The DNA extracted from each cell did generally transport into the harpsichord, however in all cases DNA irreversibly stuck to the quartz walls and could not be further transported using electrokinetic or hydrodynamic flow. Figure 5.6 illustrates DNA-wall adherence experienced in the transport microchannels. Bright regions in the harpsichord signify regions of incomplete DNA extraction and/or cell debris. The vast majority of cells in solution were in transport microchannels (2) or (1) instead of captured at the harpsichord. Attempts made to remove these extra uncaptured cells from the device resulted in the dislodging of captured cells and thus were futile. Furthermore, there was still the vast amount of extracted DNA in the cell transport microchannel from uncaptured cells. Pressure differences in the microchannel caused the uncaptured cell DNA to enter the harpsichord in addition to the captured cell DNA, impairing the utility of the single cell compartmentalized capture design. Figure 5.7 shows this failure mode. Large amounts of web-like DNA from the cell transport microchannel entered the DNA transport microchannel in most experiments performed, highlighting the need for better pressure and electrokinetic control.

In summary, the single cell capture device and designed protocol was capable of repeatably capturing and lysing single cells. However, compartmentalized transport of captured cells was not able to

be reduced to practice due to DNA adherence, the lack of appropriate fluidic control, and difficulty in manipulating large web-like volumes of extracted DNA. The information contained here is included to instruct future single cell capture experiments about potential failure modes.

5.4 – Figures

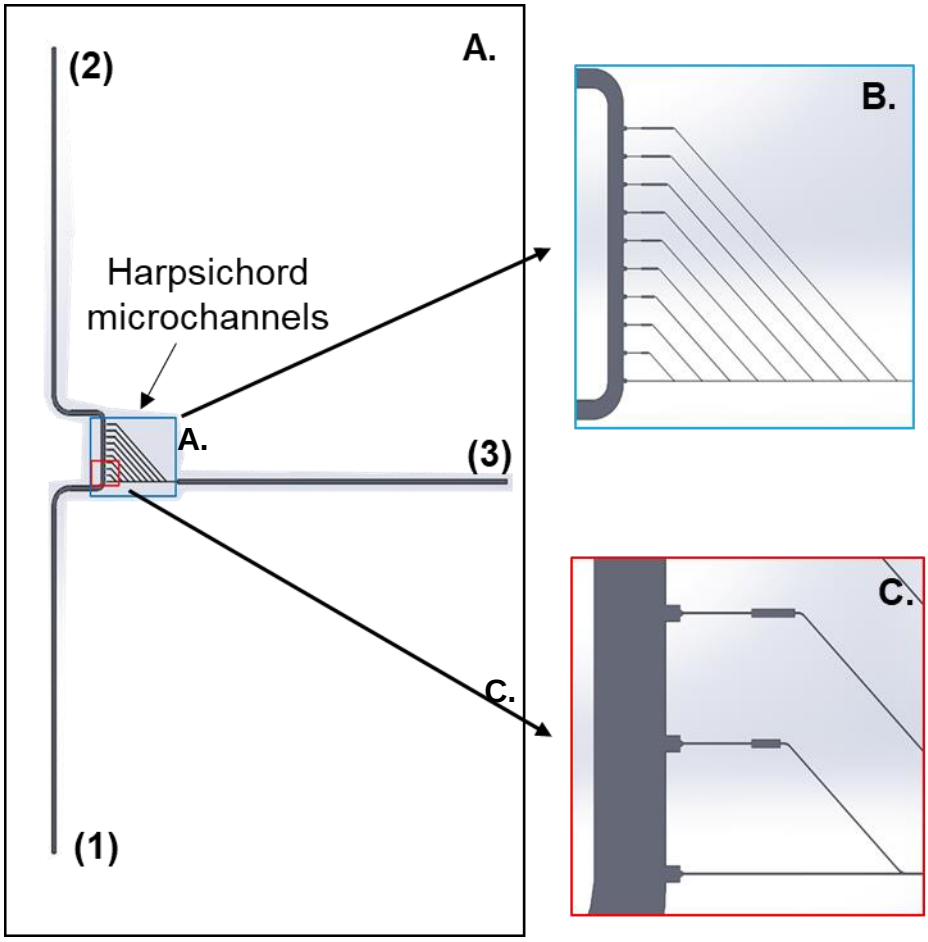

Figure 5.1: Design of single cell capture device. **A.** Overview of the device geometry. **(1)**, **(2)**, and **(3)** represent vias incorporated for cell and buffer exchange (actual vias not pictured). Three microfluidic channels (cell transport) are connected by an array of smaller microchannels (harpsichord figure) for extracted DNA transport. The DNA transport microchannels are sized so that cells are restricted from entering. Each microchannel in **B.** is a unique length for time gating of DNA transport. **C.** shows cell capture regions at the microchannel-microchannel interface, which were designed to capture a single mammalian cell approximately 10 μm in diameter.

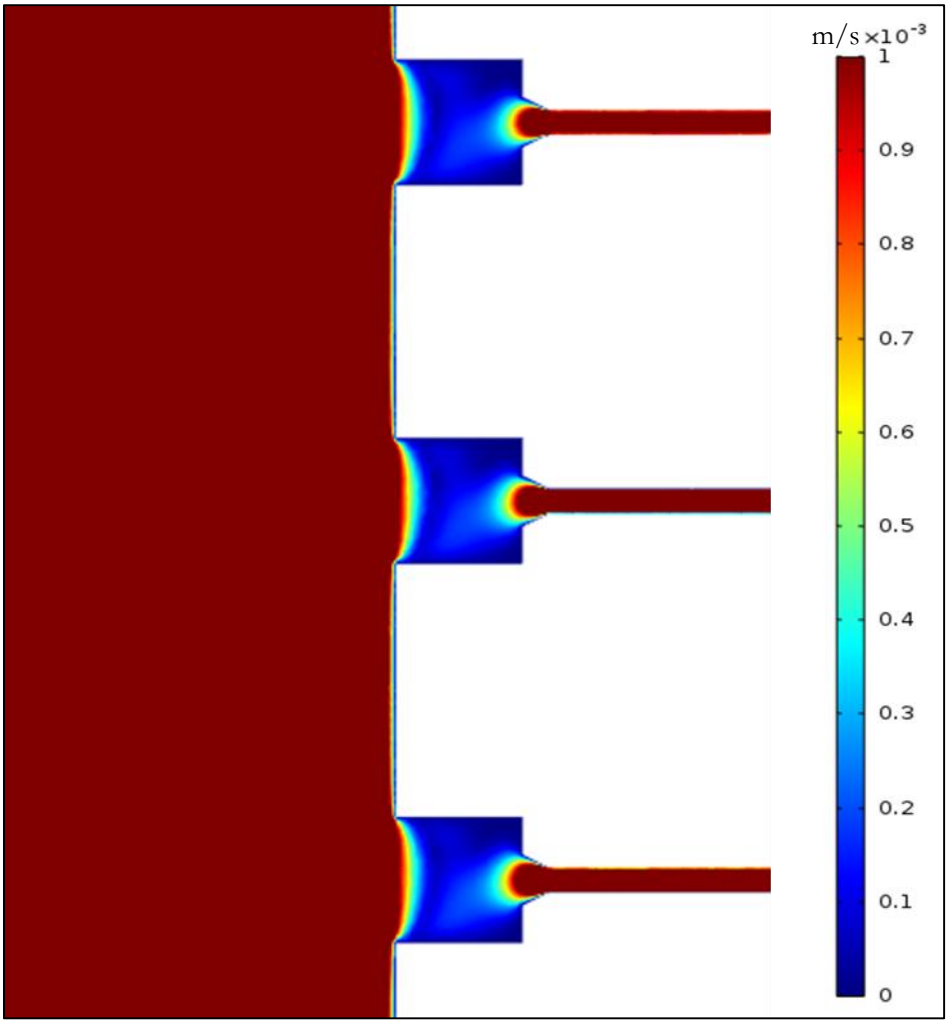

Figure 5.2: COMSOL model of expected hydrodynamic flow velocities for the single cell capture platform. Cell capture regions show dead volumes where cells capture occurs.

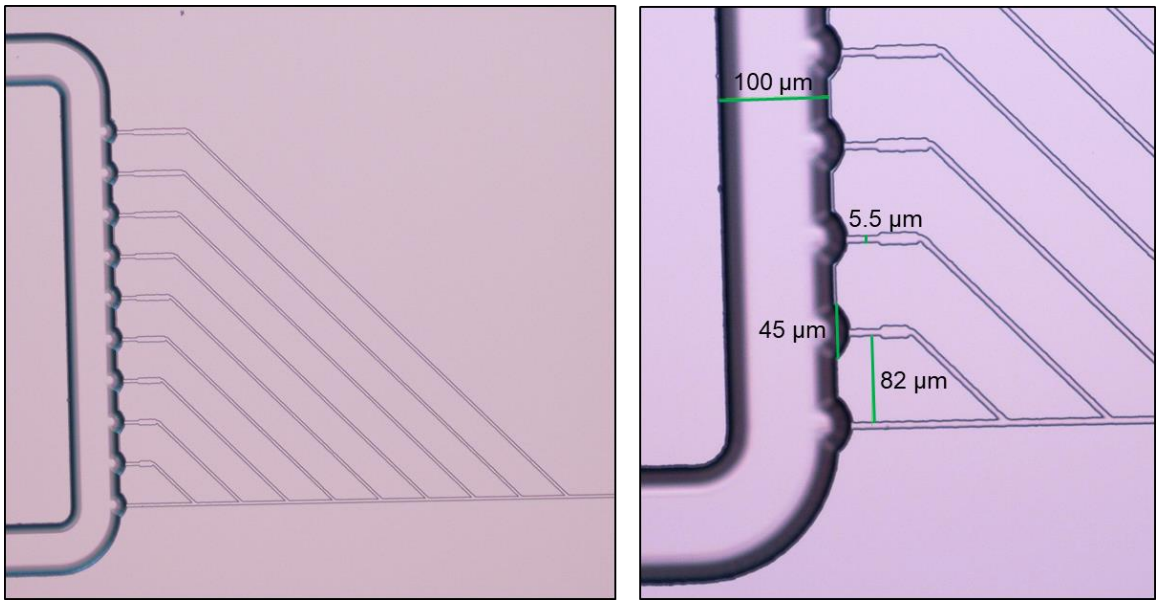

Figure 5.3: Image of cell transport microchannel-harpsichord region after fusion bonding (left) and single cell capture device with dimensions of critical microfluidic geometries (right). Corners are rounded due to isotropic wet etching.

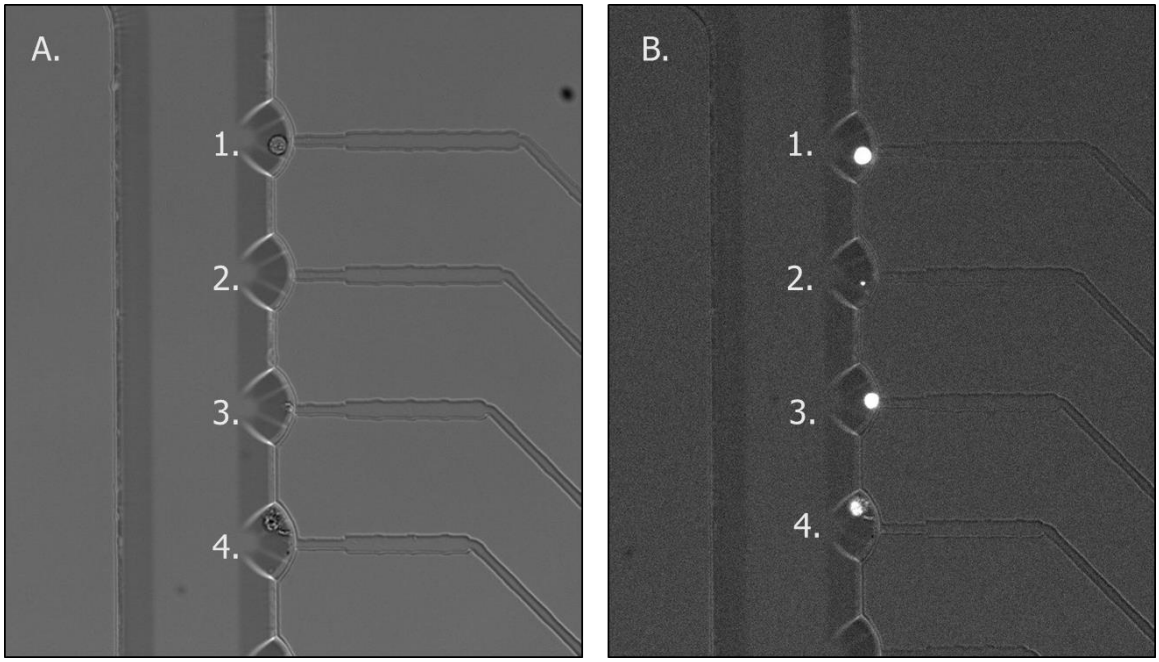

Figure 5.4: **A.** Image of captured cells taken with brightfield illumination. **B.** Fluorescent image of the same captured cells stained with Syto-16. Cellular debris can be seen in capture regions **2.** and **4.**

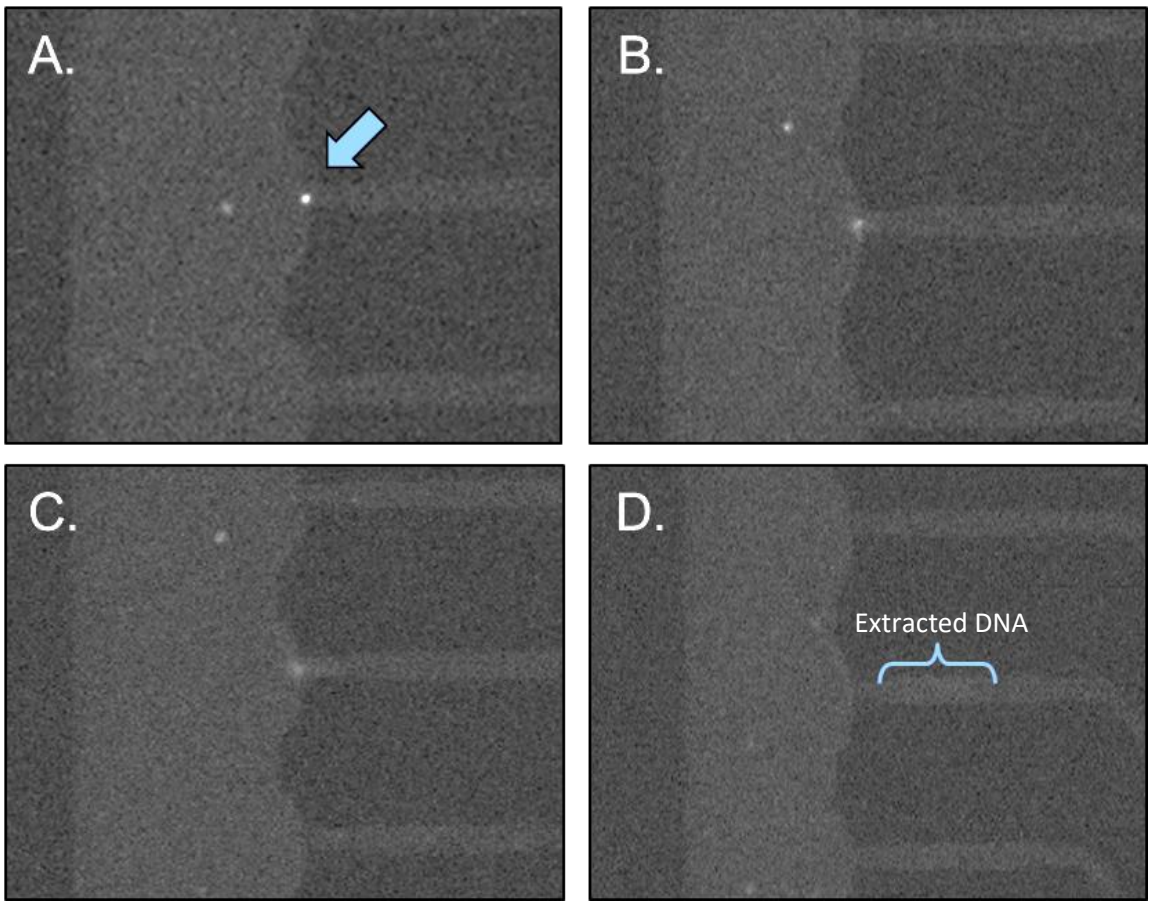

Figure 5.5: Fluorescent image of Kasumi-3 cell lysis over 32 s. The cell lyses and releases DNA from A-D. DNA diffuses out of the cell in D. and therefore more difficult to visualize due to overall decreased DNA density.

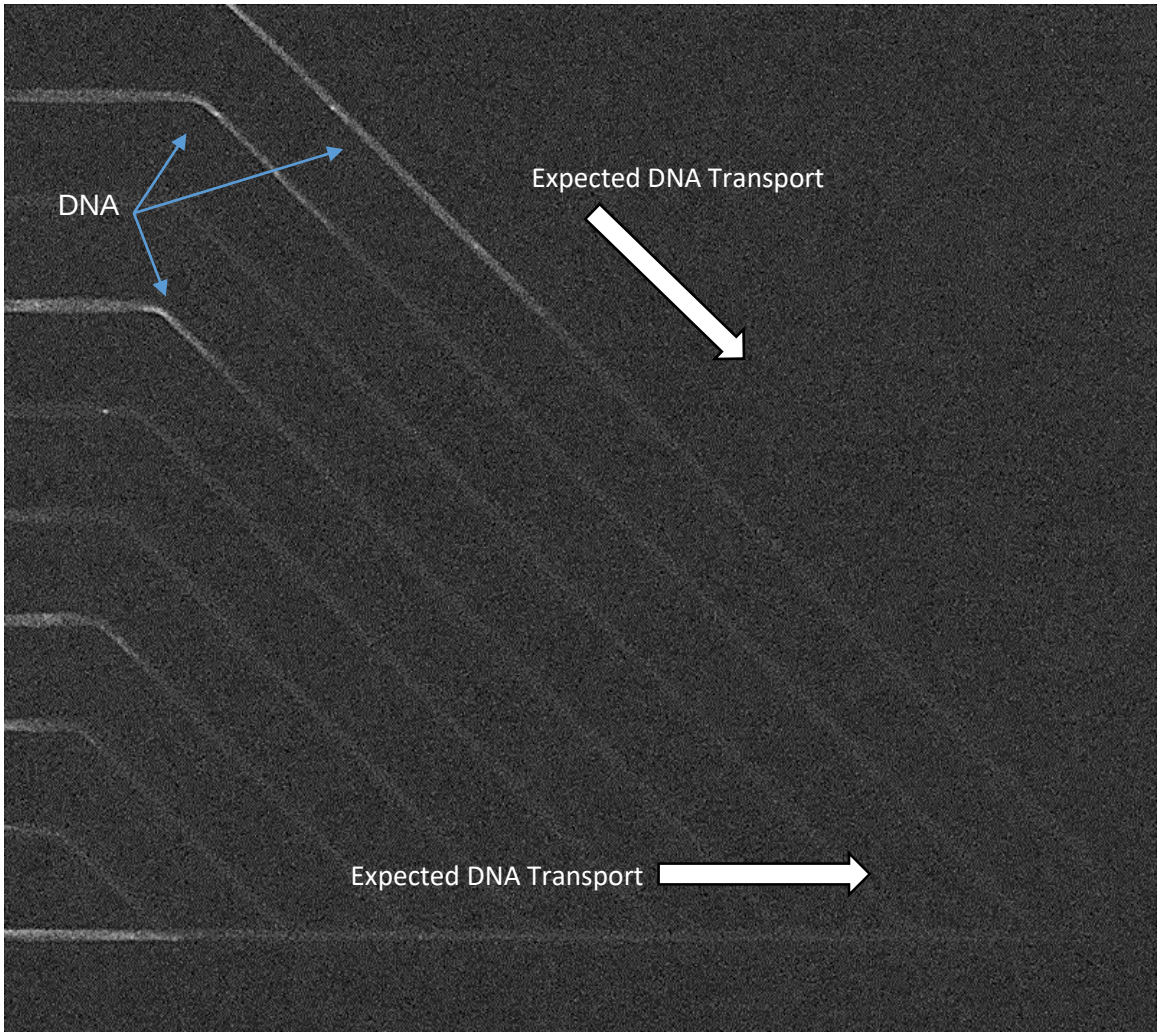

Figure 5.6: Single cell capture failure mode 1. Extracted DNA stuck to the quartz device walls instead of transporting in the expected direction towards the positive electrode. Bright regions are DNA not fully extracted or cellular debris.

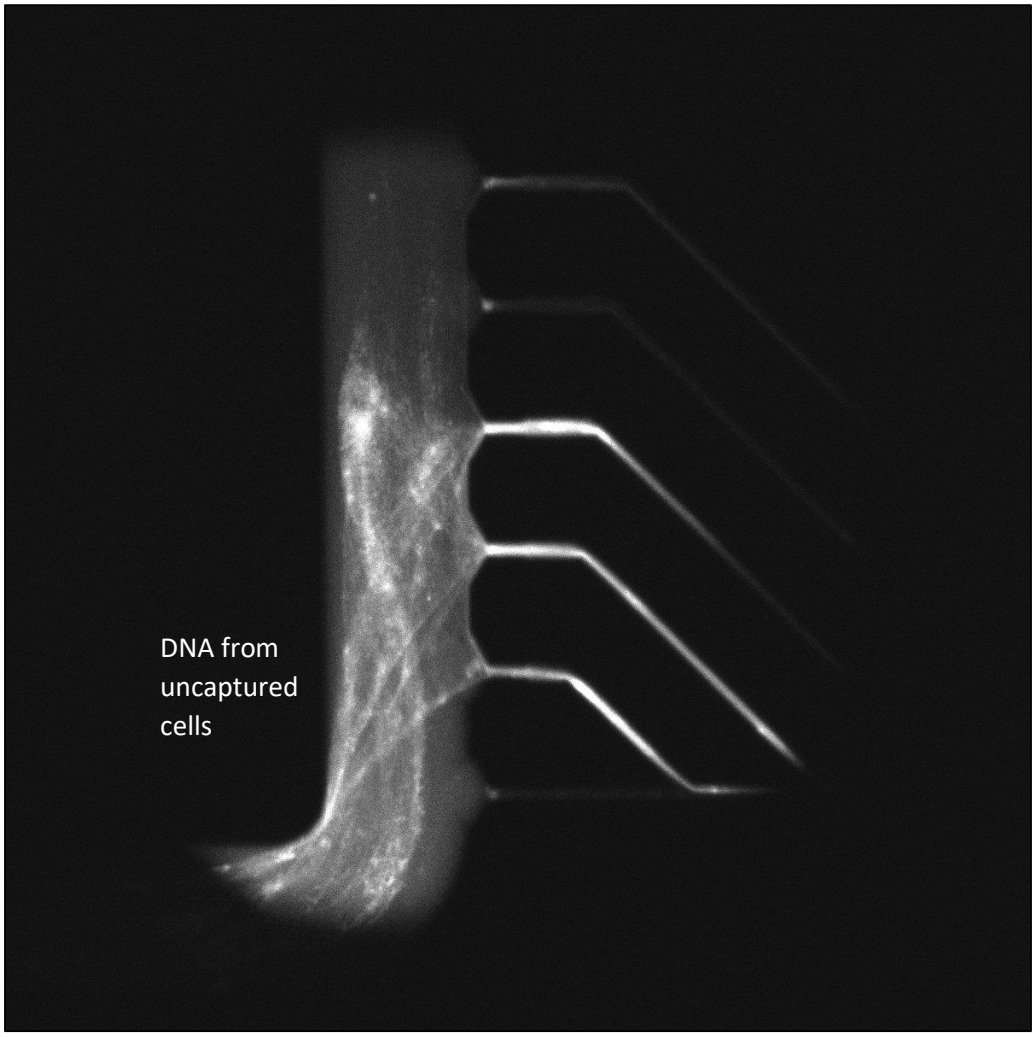

Figure 5.7: Single cell capture failure mode 2. Extracted DNA from cells in the cell transport microchannel enters the DNA transport microchannel.

REFERENCES

1. Chen, R. & Snyder, M. Systems biology: personalized medicine for the future? *Curr Opin Pharmacol* **12**, 623-628 (2012).

2. Seifert, M., Friedrich, B. & Beyer, A. Importance of rare gene copy number alterations for personalized tumor characterization and survival analysis. *Genome Biology* **17**, 204 (2016).

3. Ku, C. S. & Roukos, D. H. From next-generation sequencing to nanopore sequencing technology: paving the way to personalized genomic medicine. *Expert Rev Med Devices* **10**, 1-6 (2013).

4. Girotti, M. R. *et al.* Application of Sequencing, Liquid Biopsies, and Patient-Derived Xenografts for Personalized Medicine in Melanoma. *Cancer Discov* **6**, 286-299 (2016).

5. Ali, N., Rampazzo, R. C. P., Costa, A. D. T. & Krieger, M. A. Current Nucleic Acid Extraction Methods and Their Implications to Point-of-Care Diagnostics. *Biomed Res Int* **2017**, 9306564 (2017).

6. Branton, D. & Deamer, D. in *Nanopore Sequencing: An Introduction*.

7. Karle, M. *et al.* Continuous microfluidic DNA extraction using phase-transfer magnetophoresis. *Lab Chip* **10**, 3284-3290 (2010).

8. Benitez, J. J. *et al.* Microfluidic extraction, stretching and analysis of human chromosomal DNA from single cells. *Lab Chip* **12**, 4848-4854 (2012).

9. Wang, X. *et al.* Microfluidic extraction and stretching of chromosomal DNA from single cell nuclei for DNA fluorescence in situ hybridization. *Biomed Microdevices* **14**, 443-451 (2012).

10. Mahshid, S. *et al.* Development of a platform for single cell genomics using convex lens-induced confinement. *Lab Chip* **15**, 3013-3020 (2015).

11. Cinque, L., Yamada, A., Ghomchi, Y., Baigl, D. & Chen, Y. Cell trapping, DNA extraction and Molecular Combing in a microfluidic device for high throughput genetic analysis of human DNA. *Microelectronic Engineering* **88**, 1733-1736 (2011).

12. Takahashi, T. *et al.* A microfluidic device for isolating intact chromosomes from single mammalian cells and probing their folding stability by controlling solution conditions. *Sci Rep* **8**, 13684 (2018).

13. Craighead, H. G. I., NY, US), Topolancik, Juraj (San Jose, CA, US), Tian, Harvey (Fayetteville, AR, US), Wallin, Christopher (Ithaca, NY, US). MICROFLUIDIC DEVICE FOR EXTRACTING, ISOLATING, AND ANALYZING DNA FROM CELLS. United States patent (2018). Patent.

14. Maekawa, A. H., JP), Sakai, Tomoyuki (Kokubunji, JP), Sonehara, Tsuyoshi (Kokubunji, JP), Takahashi, Satoshi (Hitachinaka, JP). NUCLEIC ACID ANALYSIS DEVICE, NUCLEIC ACID ANALYSIS APPARATUS, AND NUCLEIC ACID ANALYSIS METHOD. United States patent (2012). Patent.

15. O'halloran, J. J. U., GB), Warburton, Elaine Harrington (Purley, GB), Solomon, Matthew Daniel (Hughesdale, VIC, AU), Mccormack, John Edward (North Warrandyte, VIC, AU), Schuenemann, Matthias (Brunswick, VIC, AU), Briggs, David James (Lancefield, VIC, AU), Andre, Mindy Lee

(Croydon, VIC, AU). MICROFLUIDIC DEVICE FOR NUCLEIC ACID EXTRACTION AND FRACTIONATION. United States patent (2014). Patent.

16. Cao, H. P., PA, US), Deshpande, Parikshit A. (Philadelphia, PA, US), Austin, Michael D. (Philadelphia, PA, US), Boyce-jacino, Michael (Titusville, NJ, US). METHODS OF MACROMOLECULAR ANALYSIS USING NANOCHANNEL ARRAYS. United States patent (2008). Patent.

17. Craighead, H. G. I., NY), Turner, Stephen W. (Ithaca, NY). Monolithic nanofluid sieving structures for DNA manipulation. United States patent (2004). Patent.

18. Claussen, J. W., DE), Wittayer, Stephan (Montabaur, DE), Selzer, Susanne (Monsheim, DE), Von Germar, Frithjof (Münster, DE),. Microfluidic extraction and reaction device. United States patent (2013). Patent.

19. Jensen, G. B. C., DK), Thomsen, Lars (Alborg, DK), Veltman, Oene Robert (Alborg, DK). Method, Chip, Device and System for Extraction of Biological Materials. United States patent (2008). Patent.

20. Bienvenue, J. M. F., VA, US), Landers, James P. (Charlottesville, VA, US), Scott, Orion N. (Charlottesville, VA, US). Multiple-sample microfluidic chip for DNA analysis. United States patent (2017). Patent.

21. Koley, D. & Bard, A. J. Triton X-100 concentration effects on membrane permeability of a single HeLa cell by scanning electrochemical microscopy (SECM). *Proc Natl Acad Sci U S A* **107**, 16783-16787 (2010).

22. Kim, J., Johnson, M., Hill, P. & Gale, B. K. Microfluidic sample preparation: cell lysis and nucleic acid purification. *Integr Biol (Camb)* **1**, 574-586 (2009).

23. Laskey, R. A., Honda, B. M., Mills, A. D. & Finch, J. T. Nucleosomes are assembled by an acidic protein which binds histones and transfers them to DNA. *Nature* **275**, 416-420 (1978).

24. Menard, L. D. & Ramsey, J. M. Electrokinetically-Driven Transport of DNA through Focused Ion Beam Milled Nanofluidic Channels. *Anal. Chem.* **85**, 1146-1153 (2013).

CHAPTER 6: CONCLUSIONS AND FUTURE WORK

6.1 – Conclusions

The goal of this work was to investigate DNA characteristics and transport in nanofluidic optical mapping-type applications. The work contained in this thesis has translational utility to mapping applications, but also furthers basic research of DNA nanochannel transport and polymer physics in confinement. Studying the polymeric extension behavior of DNA in nanochannels resulted in the first quantitative agreement between empirical data and theory in the extended de Gennes regime. Contrary to past findings, the DNA extension length (R) was found to scale with D_{eff} in close agreement with the theoretically predicted relationship ($R \sim D_{eff}^{-2/3}$) and simulation results, with best-fit exponent values ranging from -0.67 to -0.70 across the three devices. Results suggested that the inclusion of DNA extension data in nanochannels with a single dimension below a critical dimension threshold (channel width or depth below 219 nm in this experimental series) can significantly impact extension scaling results; therefore, using D_{eff} to approximate channel dimensions is invalid when a single channel dimension is below the threshold. In addition, modest changes in aspect ratios, at least from 1 – 3 (width/depth), were shown to have negligible effect on DNA extension and subsequent extension scaling.

The development of a quantitative method for analysis of DNA transport through a nanochannel was presented to compare DNA transport in a variety of mapping-like conditions. YOYO-1 labelled HindIII digest fragments were transported through COP and quartz nanochannels, where their transport through three distinct regions of interest was recorded with a sCMOS camera and analyzed. Image traces at successive ROIs were analyzed with the use of cross-correlation, DNA sizing, fragment size calibration, and lastly fragment assignment based on DNA transport time and fragment size. DNA fragment traces were assigned into one of three groups depending on their size and relative arrival time: correctly-called, incorrectly-called, and missing fragments. Correctly-called fragments are fragments that were successfully matched at both ROIs with similar fragment size and within the expected arrival time window. Incorrectly-called fragments arrived within the expected time window but were not the same size

fragment, suggesting the occurrence of detrimental DNA-wall interactions during transport. Missing fragments were fragments that were identified at the first ROI but disappear from the second, again suggesting detrimental DNA-wall interactions strongly slowed DNA transport. Incorrectly-called and missing fragments were jointly classified as fragments with impacted transport, the percentage of which was used to compare transport in different experimental conditions. The aforementioned method was used to analyze DNA transport in mapping-type conditions in quartz and COP devices, different buffer components, and enabled the comparative analysis of oligonucleotide dynamic coatings to minimize detrimental DNA-wall interactions.

Conductivity measurements, photodamage controls, and magnesium cation presence controls were developed to verify experimental consistency and facilitate experimental comparisons. Quartz and COP device substrates were compared and exhibited similar DNA transport efficiency. The addition of Mg cations detrimentally inhibited DNA transport by increasing stick-slip motion and DNA-wall affinity. Mg-DNA bridging was hypothesized as the leading cause of decreased transport performance. An oligonucleotide dynamic coating was included in the buffer to improve DNA transport performance in the presence of Mg. Buffers with the oligonucleotide dynamic coating resulted in a significant improvement in DNA transport efficiency, decreasing the number of DNA fragments with impacted transport down to buffers with no Mg present. In addition, it was discovered that small HindIII fragments are more likely to be affected by detrimental transport conditions than large DNA frements. This DNA size-dependent transport efficiency was witnessed in all experiments. The analysis method was used in addition to quantify DNA diffusion in nanochannels. The diffusivity of DNA fragments also exhibited a strong size-dependence, with small fragments diffusing greater distances than large fragments. The scaling of DNA fragment diffusivity was discovered to be intermediate to Rouse diffusivity theory and bulk empirical measurements. All of these findings have implications for DNA mapping applications, particularly the data showing increased transport performance in the presence of oligonucleotide dynamic coatings.

Last of all, the design, fabrication, and testing of a device capable of capturing single cells was described. The purpose of the device design was to enable capture of a single cell, lyse the cell to release cell-specific genomic material, compartmentalize the lysed DNA, and transport cell-specific DNA downstream for genetic analysis. The device demonstrated repeatable capture and lysis of individual

cells, however compartmentalized transport of cell-specific DNA was not able to be reduced to practice due to DNA adherence, lack of fluidic control, and the difficulty faced in manipulating large volumes of DNA. The device design and capture experiments were included to inform about expected failure modes during DNA extraction and transport, as well as provide a starting point for future design and development.

6.2 – Future Work

The study of DNA extension physics in nanochannels has slowed in recent years due to the disconnect between theory, simulation, and empirical measurements. The empirical data in agreement with theory and simulation in this dissertation may breathe new life into the otherwise stagnant field, increasing interest in simulations and empirical measurements of DNA in confinement. Furthermore, study into the influence of intercalating dyes to DNA characteristics like persistence length is still not fully understood. Additional research into this area will be necessary to develop a deeper understanding of DNA physics.

Nanofluidic platforms for genetic analysis still have numerous obstacles to overcome before mass commercialization occurs. Designing methods to minimize DNA-wall interactions is paramount to long-term success, and the use of oligonucleotide dynamic coatings may not be possible in all genetic analysis scenarios. Further advancement of nanofluidic optical mapping platforms will be driven by fundamental nanofluidic research. To start, the DNA transport analysis method described could be used to compare nanofluidic transport performance in a range of polymeric materials to inform device fabrication. In addition, while HindIII digest DNA fragments were used in this work due to ease of access, further research into DNA-wall interactions or DNA transport could incorporate additional digests or even active restriction digestion in the nanochannels.

The DNA transport analysis method could be used to further investigate DNA size-specific diffusion in nanochannels to obtain a deeper understanding of molecular diffusion in confinement. Studies investigating diffusion in nanochannels have not developed diffusion theory with DNA size as an independent variable. Comparing the diffusivities of different sized DNA fragments may lead to a universal diffusivity vs size curve and lead to the formulation of exact equations for diffusion theory in nanochannels. Additional work could also look into the interpenetration of closely-spaced DNA fragments

due to diffusion during nanochannel transport to determine if fragments change order without wall interactions. This type of work would require software capable of ordering successive DNA fragments at multiple points, accordingly the DNA transport analysis method could provide a starting point for that type research.

Finally, the failure modes of the single cell capture device highlights the need for additional research into the manipulation of extracted DNA. Entire genomes of genetic material are difficult to control in microfluidic environments. Potential separation techniques or multi-step lysis techniques could mitigate DNA transportation issues and make single cell extraction of long DNA strands feasible. The utilization of pressure control systems instead of relying on head pressure could also improve cell loading and DNA extraction.